CASI

HIGH SPEED CIVIL TRANSPORT DESIGN USING COLLABORATIVE OPTIMIZATION AND APPROXIMATE MODELS

A final report
submitted to NASA Langley Research Center
in partial fulfillment of the research
funded by Grant # NCC-1-253

By
Valerie Michelle Manning
1997-1999

Abstract

The design of supersonic aircraft requires complex analysis in multiple disciplines, posing a challenge for optimization methods. In this thesis, collaborative optimization, a design architecture developed to solve large-scale multidisciplinary design problems, is applied to the design of supersonic transport concepts. Collaborative optimization takes advantage of natural disciplinary segmentation to facilitate parallel execution of design tasks. Discipline-specific design optimization proceeds while a coordinating mechanism ensures progress toward an optimum and compatibility between disciplinary designs.

Two concepts for supersonic aircraft are investigated: a conventional delta-wing design and a natural laminar flow concept that achieves improved performance by exploiting properties of supersonic flow to delay boundary layer transition. The work involves the development of aerodynamics and structural analyses, and integration within a collaborative optimization framework. It represents the most extensive application of the method to date.

Nomenclature

AR	aspect ratio
b	wing span
c	chord, constraint
C_L	lift coefficient
C_p	pressure coefficient
C_f	friction coefficient
d	diameter, distance
$\frac{D}{T}$	drag to thrust ratio
E	Young's modulus
f	aerodynamic force on a wing panel
F	aerodynamic force on a wing strip
h	altitude, enthalpy
H	shape factor (δ^*/θ)
J	objective function
J^*	optimal objective function
l	length
L	lift
$\frac{L}{D}$	lift-to-drag ratio
LFL	landing field length
M	moment, Mach number
n	load factor, linear amplification ratio

N^*	composite amplification factor
q	dynamic pressure
R	aircraft range in nmi
S	wing reference area
sbr	wing span break ratio $\left(\frac{y_{break}}{(b/2)}\right)$
sfc	specific fuel consumption
$SLSTH$	sea level static thrust
T	torque, temperature
t	FEM thickness
$\frac{t}{c}$	thickness to chord ratio
$TOFL$	take-off field length
$tsfc$	thrust specific fuel consumption
u	local velocity, x direction
v	local velocity, y direction
V	velocity
w	local velocity, z direction
W	weight
x	chordwise station
$\{X\}$	design variable vector
y	spanwise station, in ft
$\{Z\}$	system level target vector

GREEK

α	angle of attack
δ	structural deflection
δ^*	displacement thickness
γ	flight path angle
μ	viscocity
ν	efficiency

ρ	density
σ	stress
σ_x, σ_y	normal stress
$\sigma_{vonmises}$	vonMises stress
τ_{xy}	shear stress
θ	twist, momentum thickness
Θ	spanwise twist distribution
τ	wing taper ratio
ω	frequency

SUBSCRIPTS

a, aero	aerodynamics
break	wing break location
cr	cruise condition
e	edge, external
f	final
fuel	fuel
fuse	fuselage
horiz	horizontal tail
i	initial
in	inboard of wing break
jig	built-in twist
LE	leading edge
man	maneuver condition
m, miss	mission
o	target variable
out	outboard of wing break
p	propulsion
root	wing root location

s, stru, struct	structures
TE	trailing edge
tip	wing tip location
trap	related to trapezoidal wing parameter
vert	vertical tail
w	wing, wall

ACRONYMNS

ALI	attachment line instability
CFI	crossflow instability
CO	collaborative optimization
COURSE	collaborative optimization using response surface estimation
HLFC	hybrid laminar flow control
HSCT	high-speed civil transport
HSR	NASA High Speed Research program
LFC	laminar flow control
LFL	landing field length
MDO	multidisciplinary optimization
NASA	National Aeronautics and Space Administration
NLF	natural laminar flow
RS	response surface
SST	supersonic transport
TOFL	take-off field length
TSI	Tollmein-Schlicting instability
USOC	United States Olympic Committee
VCE	variable cycle engine

Contents

List of Tables

List of Figures

Chapter 1

Supersonic Commercial Aircraft Design

Transport is a necessary finishing process of production: The faster it goes the better it is for business.

Fernand Braudel

1.1 Introduction

1.1.1 Motivation for Commercial Supersonic Aircraft

Fast, faster, fastest. On foot, and in land, water and air vehicles, humans have pushed for enhanced performance. We can now run farther than the length of a football field in less than 10 seconds, and sprint a mile more than 15 seconds faster than the "unbreakable" 4 minute barrier. Each was recently thought impossible. We have designed automobiles that travel faster than sound waves in air, and engineless water vehicles outrun the wind that propels them. Aircraft now routinely travel at many times the speed of sound. And of course there exists a commercial supersonic aircraft that can whisk passengers to their destination at twice the speed of sound.

The U.S. has long wanted to have a fleet of commercial supersonic transports, but there are two main obstacles to overcome before this platform will become a reality. These barriers, economics and modern environmental laws, have postponed the launch of supersonic aircraft for commercial use.

Not everyone has supported the mission. In 1970, the director of the *Citizens League Against the Sonic Boom* wrote an entire book condemning the "unnecessary plane that could destroy peace and quiet throughout much of the civilized world." [69].

Any current commercial transport must be environmentally and economically acceptable. Ticket prices should be within about 20 percent of current business class fares, and maintenance must be affordable for the airlines. The aircraft must not disturb civilians beneath its flight path, contribute to ozone layer depletion, or consume excessive amounts of fossil fuel. The problems are many, but the potential to traverse half of the globe in less than half of the time offered by current travel methods is a powerful motivator. Be it a super-sized transport carrying over 250 passengers, or a small craft with less than fifteen travelers, the American supersonic passenger plane will exist.

1.1.2 Multidisciplinary Optimization: A Necessary Part of Supersonic Aircraft Design

Aircraft design is necessarily a multi-disciplinary problem. It is, in fact, important to perform some sort of iterative analysis in order to design most large-scale systems. This requirement is a consequence of the natural interdependencies involved in the primary engineering disciplines. One of the most basic interactions involves the structure of an aircraft wing and its aerodynamics. For supersonic aircraft, a thinner wing results in lower wave drag; however structural bending strength is inversely proportional to thickness. Another interaction involves propulsion and weight. A light aircraft with low drag is preferred for propulsive efficiency, but sufficient size and strength to support the the engines on the wing or fuselage and to carry sufficient fuel tends to drive up the weight. One great issue in supersonic design is the trade-off assessment and convergence of these conflicting effects.

In recent years, various multidisciplinary design optimization approaches have been applied to High Speed Civil Transport (HSCT) analytical design [10, 39, 65, 66, 74, 81] and to multidisciplinary analysis integration using varying fidelity models [39].

1.2 Challenges of Commercial Supersonic Aircraft Design

For many years now, military supremacy has depended upon supersonic fighter and bomber aircraft, proving the importance and ensuring the advancement of supersonic aircraft technology. In fact, military necessity has driven many technological advancements and commercial aviation has benefitted greatly from the technology developed for these projects.

United States involvement in World War II predicated improvements in fighter aircraft, and created a need to deal with locally supersonic flows. Also, the turbojet engine was introduced, promising even further speed increases. In the early 1940s aerodynamicists could not yet predict with certainty what occurred in the speeds of transonic flight. Researchers needed to develop accurate research tools and methods to derive needed data and to solve the mystery of compressibility and transonic aerodynamics [34, 49]. By 1946, there was general, but not universal, public opinion that the speed of sound in air, 760 miles per hour at sea level and 660 miles per hour at an altitude of 36 000 ft, represented an impenetrable barrier through which no airplane could fly [34]. Before that time, a number of aircraft had lost control or experienced strong buffeting at velocities approaching the speed of sound. Once the *barrier* was broken by then U.S. Air Force Captain Charles "Chuck" Yeager in 1947 however, many supersonic aircraft soon followed.

About three decades ago, the United States had developed plans for a supersonic commercial transport (the SST). The airplane was to enter service in the 1970's and revolutionize air travel less than 15 years after the nation held the first subsonic jets in awe. Market projections for the SST ranged as high as 500 aircraft by 1990 [1]. Prior to its absorption into NASA in 1958, the National Advisory Committee for Aeronautics (NACA) developed experimental methods and facilities for the study of supersonic problems. From that time until 1971, NASA's role in supersonic technology included research supporting the development of two aircraft. The first was a U.S. Mach 3 cruise bomber called the B-70. The B-70 had been proposed as a replacement for the B-47 but the project was canceled in 1959 due to transfer of interest to intercontinental ballistic cruise missiles (ICBMs).

The second NASA supersonic project was the SST. President Kennedy supported this project, and proposed an SST be produced within the decade of the 1960's. Throughout the effort, the most powerful criticisms were environmental, such as sonic booms and ozone depletion. Meanwhile, the French and British came together to unveil the Concorde at the 1971 Paris Air Show. The Concorde was, in the words of Alan S. Boyd during his tenure of

Chairman of Airbus Industrie of North America, "a pretty good case history of how *not* to produce an airplane" [1]. It is however, to this day the only active supersonic commercial transport due in part to the fact that the U.S. SST project in 1972 was canceled by congress. After the U.S. program folded, NASA still focused on solving the remaining technical problems which were the barriers to supersonic cruise flight. The High Speed Research Program (HSR) was established in the early 1990s as a technology development program intended to enable the commercial development of a "next generation" HSCT. Major areas of study by HSR are propulsion, airframe materials and structures, flight deck systems, aerodynamics performance, and systems integration. In recent years researchers in government, industry, and education have joined HSR to resurrect the concept and to develop technology to make feasible a commercially successful vehicle capable of sustained supersonic flight. Boeing and McDonnell Douglas among others, have poured many hours into technology assessment and development. Various studies predicted a substantial opportunity for a future HSCT aircraft to in rapidly growing long-haul market, and that in the period from 2005 - 2015, this market could support 500-1000 HSCT aircraft, creating multibillion dollar sales opportunity for its producers [61]. The HSCT would take advantage of the growth rates of flights to the South Pacific, slashing the 9-to-16 hour flight times. Even commercial shipping companies such as Federal Express could benefit from such aircraft. A sample of routes proposed for the HSCT appears in Figure 1.1, including both trans-pacific and trans-atlantic travel.

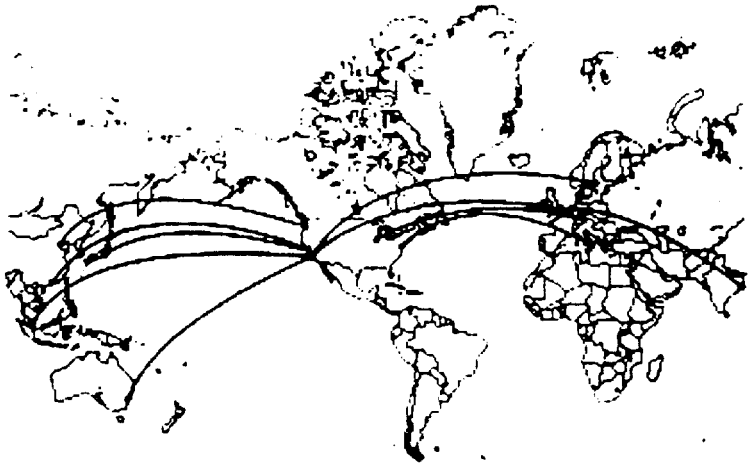

Figure 1.1: HSCT potential routes

Most early military supersonic planes were designed for maneuverability, high climb-rates, and short-range flights at supersonic speeds. The engines were designed to provide performance rather than efficiency. [49]. A modern commercial supersonic air vehicle presents additional challenges. As proven by the Concorde and the Mach 3.0 SR-71 "Blackbird", sustained supersonic flight introduces issues in fatigue, heating, and maintenance. Supersonic flight over land will only be possible if sonic footprints are vastly reduced, and commercial airport noise ceilings are an important constraint affecting propulsion systems. Federal Aviation Administration (FAA) reserve fuel requirements must be met, the aircraft must be able to take-off and land at existing airports, and be prepared to operate for upwards of 50 000 hours. In addition, the aircraft will be required to operate fairly efficiently at subsonic speeds for take-off, landing, and over-land flight.

Propulsion issues abound, as modern HSCT engines require revolutionary advances. New engine materials and combustor technology are necessary for propulsion system design that satisfies modern emissions, noise, vibration, thrust, weight, fuel efficiency, service life, and reliability performance [20]. There is also a concern about engine emission of nitrogen oxides (NO_x) contributing to ozone layer depletion, as the engines of the HSCT would operate in the stratosphere where these emissions are thought to be quite harmful. The primary concept for the modern HSCT is a variable cycle design that integrates the benefits of a zero-bypass turbojet at cruise and a high-bypass turbofan at off design points, such as take-off, climb, and lower speeds.

The new HSCT will have structural and materials hurdles to clear. Speeds much over Mach 2.0 provide a temperature rise at which aluminum alloys, of which the Concorde is constructed, begin to lose strength. Aluminum alloys generally operate up to 200 degrees farenheit while titanium, of which the SR-71 is constructed, is thermally stable to 350 degrees. An all-titanium commercial aircraft would, however, be too heavy for efficient commercial operation, thus aircraft which cruise above the temperature limit of aluminum alloys require titanium alloys or composites as the basic materials [61].

Wing deflections under load are also an issue, as supersonic aircraft wings are quite thin. Combined with large chords and spans, such planforms requires structural stiffening to avoid excessive deflection from heating and aerodynamic loading. Addition of internal material to control the deflections leads to a weight penalty, and constrains the available wing fuel volume.

Some of the most difficult requirements to meet involve environmental compliance. Sonic

booms, engine noise at take-off, emissions, and atmosphere deterioration are all relevant issues. Any aircraft flying supersonically will create a shock wave and the associated sonic boom. Increasing the size and speed of the moving body increases the strength of the shock wave, thus the strength of the boom.

Depending upon the source, the effect of the sonic boom on the environment varies. According to the Office of Technology Assessment, the sonic boom levels created by an HSCT would not be expected to cause any appreciable property damage during flight over land [49, 57]. Regardless, public outcry prompted the passing of a 1971 law by congress denying supersonic flight over the continental United States to commercial airplanes. Boom size and propagation can be altered with design, but as yet not completely eliminated. Supersonic footprint definition and reduction comprises an entire field of research.

Finally, further challenges in HSCT design are presented when considering the passenger, whose main concerns are likely safety, price, and comfort. Previous works [1, 17, 21] have considered details such as cost, routes, and FAA regulation compliance. Certification studies detailing these issues have been published [51].

1.3 Supersonic Commercial Aircraft Concepts

Early aircraft were designed with wings of little or no sweep, and even the first supersonic aircraft, the Bell X-1, had almost unswept straight-tapered wings. Generally when local and freestream velocities approached the supersonic regime, these unswept rectangular "Hershey bar" wings showed large increases in drag. In 1942, Alexander Lippisch studied the problems of supersonic flight. He decided upon a delta wing of very small wingspan and a 60 degree leading edge sweep angle with very thin sections. He tested a wind tunnel model of the design and the resulting drag through the transonic regime were compared with a rectangular wing. As can be inferred from Figure 1.2, the delta wing was favored for supersonic performance [43].

Virtually all modern supersonic *cruise* aircraft use some derivative of the "delta" or triangular wing. Ideas for supersonic aircraft configuration have changed little since the early 1960's. For example the modern B-1 bomber closely resembles the NASA Supersonic Commercial Air Transport (SCAT)-16, proposed in 1963. Of the two aircraft studied in this work, one employs the more conventional delta-like planform, while the other, for reasons to be explained in Section 1.3.1.2, utilizes wings with much less sweep.

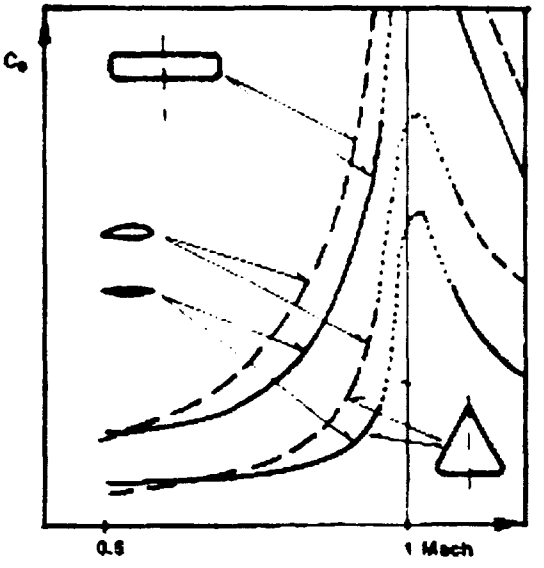

Figure 1.2: 1943 Supersonic delta wind tunnel test. Drag coefficient versus Mach number for two planforms and two airfoil types.

An aircraft not designed as a derivative of the delta planform is the Oblique All-Wing Supersonic Transport [83, 84], studied at NASA Ames Research center and within the Aircraft Design Group at Stanford University. This aircraft, shown in Figure 1.3, was a Mach 2.0 concept designed for efficient long-range flight. Though a 20 foot span flight dynamics testbed of this unique design was built and flown at Stanford University, the full-scale aircraft has not been developed.

The British/French Concorde ranks as one of history's foremost technical achievements. The two nations that developed this aircraft not only spoke different languages, but also used different measurement systems. Yet, out of this alliance came the first and only commercial supersonic transport in regular passenger service [49]. The well-documented shortcomings, largely economic, are attributable in part, to the small passenger capacity and to the conservative approach followed in the design. The aerodynamics of the supersonic transports require that the nose of the aircraft extend beyond the flight deck, impairing crew visibility. The Concorde has the ability to droop the nose on high angle of attack take-off and landing. A modern aircraft version might use computer technology to incorporate an artificial vision for the crew.

The Concorde "ogee" planform was evolved in part "to obtain the virtues of the canard

Figure 1.3: Oblique all-wing supersonic transport

but to avoid the problems of troublesome canard tip vortices by integrating it into the wing planform." [59] This cranked delta type wing employed on the Concorde and on most proposed successors has leading edges that are subsonic (swept behind the Mach cone) inboard and supersonic (swept in front of the Mach cone) outboard. Thus the inboard wing leading edges can be rounded while those outboard are sharp, to avoid a detached shock. To reduce the wave drag penalty, the supersonic aircraft wings must be quite thin. For example, the Concorde thickness-to-chord ratio varies from between 3% to 1.75% at the root and tip respectively, for a 2.5% average. This slender wing concept provides improved wave drag characteristics.

Another supersonic aircraft of interest in industry is the supersonic executive jet. Executives, celebrities, and others with the means currently employ subsonic versions of these smaller aircraft that free them from adhering to airline schedules, and could allow landing at smaller airports.

National Business Aviation Administration (NBAA) president John W. Olcott has said that business aviation is experiencing a needs-driven market mode that is centered on meeting the expanding travel requirements of corporate America [4]. This feeling is reflected in industry, where the belief is that a corporate supersonic transport appears to have a significant market. Military technology and excess production capacity provide the basis

for making such an aircraft affordable [70]. In the late 1980s, Gulfstream and the Sukhoi and Lyulka design bureaus planned, but did not launch, a 10-seat Mach 2 business jet. It was a U.S.-Russian cooperative program, and had an estimated price of 40-50 million dollars. Early next century, this figure would be closer to 60-70 million dollars. Currently in the late 1990's major manufacturers of business class aircraft, Dassault and Gulfstream, along with Lockheed Martin's Skunk Works are studying supersonic business jets (SSBJ). French manufacturer Dassault Aviation is tentatively planning an 8-seat Mach 1.8 SSBJ scheduled for entry in 2005-2007 [76]. Dassault executives estimate that the market would be around 150-200 aircraft.

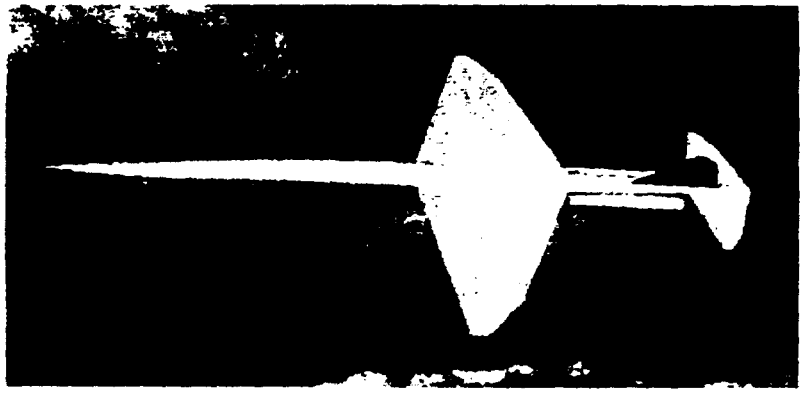

Figure 1.4: ASSET natural laminar flow executive jet, Morris, 1994.

The Asset Group, led by Dr. Richard Tracy, has patented an executive jet designed for supersonic laminar flow [79]. The laminar flow on the low-sweep, ultra-thin wing shown in Figure 1.4 is to be achieved naturally, without assistance from laminar flow control devices. This 5000 n.mi. aircraft would have operational and environmental advantages over turbulent jets. The Asset plane is a version of the natural laminar flow aircraft analyzed in this dissertation.

1.3.1 Supersonic Laminar Flow Aircraft

To reach the high lift-to-drag ratios required for long ranges between 5000 - 6500 nautical miles, and to reduce thrust requirements, low drag coefficients are necessary. The total aircraft drag consists of wave drag, vortex drag, and friction drag.

Viscous drag is largely a function of the surface area of the aircraft as well as the flight condition and configuration. Figure 1.5 shows the change in cruise lift-to-drag ratio

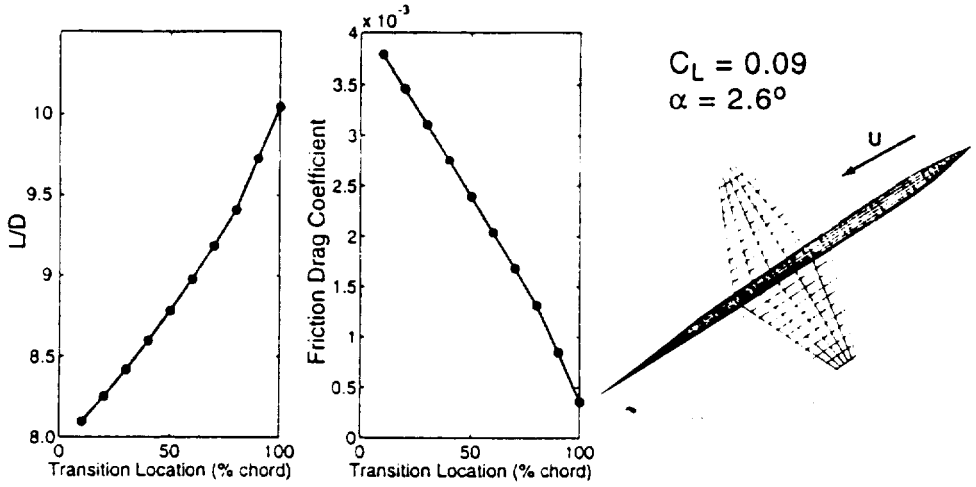

Figure 1.5: Wing skin friction drag coefficient and aircraft L/D versus wing laminar flow fraction

with increasing laminar flow fraction using the analyses developed for this research. It is clear from this plot that flying with laminar flow provides significant savings. As the flight condition does not change, the savings is due solely to the great reduction in wing friction drag coefficient. Delayed boundary layer transition results in lower friction drag, reduced fuel burn, and less heating of materials, allowing for a weight savings or increased range. This increases the chances for a profitable supersonic transport or business jet. The

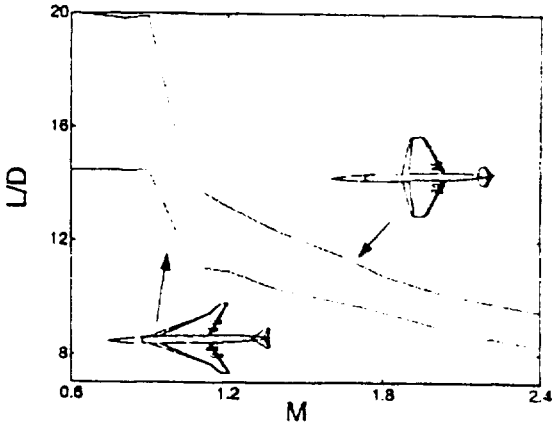

Figure 1.6: L/D versus Mach number: NLF and conventional "double-delta" aircraft.

optimal benefit of flying with laminar flow is achieved in design, by re-sizing the vehicle. Thus laminar flow control could yield reductions in aircraft take-off gross weight, operational

empty weight, and block fuel for a given mission, and significant improvements in cruise L/D. Figure 1.6 is a plot of predicted L/D versus Mach number for a conventional HSCT design, assumed turbulent, and an alternative, 95 percent laminar aircraft. At supersonic transport flight speeds there is a potential L/D increase of over 10 percent. Associated benefits may include reductions in emissions and noise, and smaller engine requirements. Two basic approaches to reducing friction drag are maintaining laminar flow with laminar flow control devices and taking advantage of design knowledge and the properties of supersonic flow to naturally delay boundary layer transition. These approaches are introduced and discussed in the following sections.

1.3.1.1 Supersonic Laminar Flow Control

Laminar flow control (LFC) is the use of artificial or mechanical action to delay boundary layer transition. A complex process, laminar flow control consists of suction, cooling, or a combination of the two. Suction is performed via ducts, flutes, and a pump source over the wing chord and can "refresh" a boundary layer, defending against Tollmien-Schlichting instabilities (TSI), crossflow instabilities (CFI) and contamination from attachment line instabilities (ATI). Conventional supersonic transport wings have rounded subsonic leading

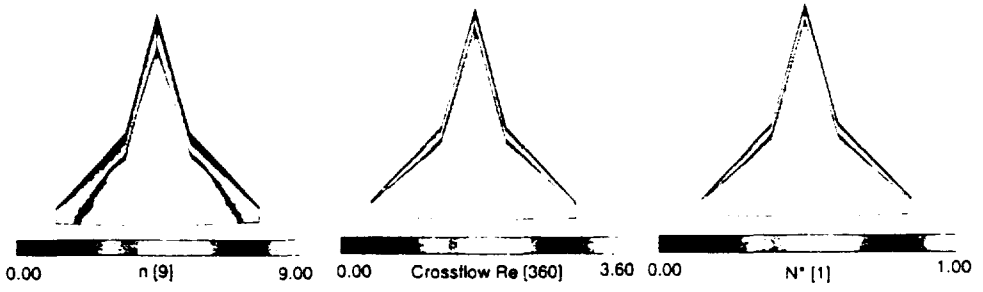

Figure 1.7: Boundary layer transition due to streamwise instability, crossflow instability and a combination. White areas indicate turbulent flow.

edges on the highly swept inboard portion. In this region is an attachment line boundary layer which flows along the leading edge spanwise from the root, splitting between the upper and lower surfaces. If the resulting attachment line instabilities become critical, the entire wing boundary layer will be contaminated, and possibly become turbulent.

The high sweep of the inboard portion of the conventional wing means that the boundary layer is prone to transition due to crossflow instability. The outboard, supersonic leading edge portion could possibly maintain laminar flow without laminar flow control if it is

not too contaminated by the residual crossflow emanating from the inboard portion of the wing. Such a wing would require laminar flow control to improve the boundary layer characteristics. Figure 1.7 shows predicted transition for a conventional HSCT planform. The boundary layer analysis is described in Chapter 3.

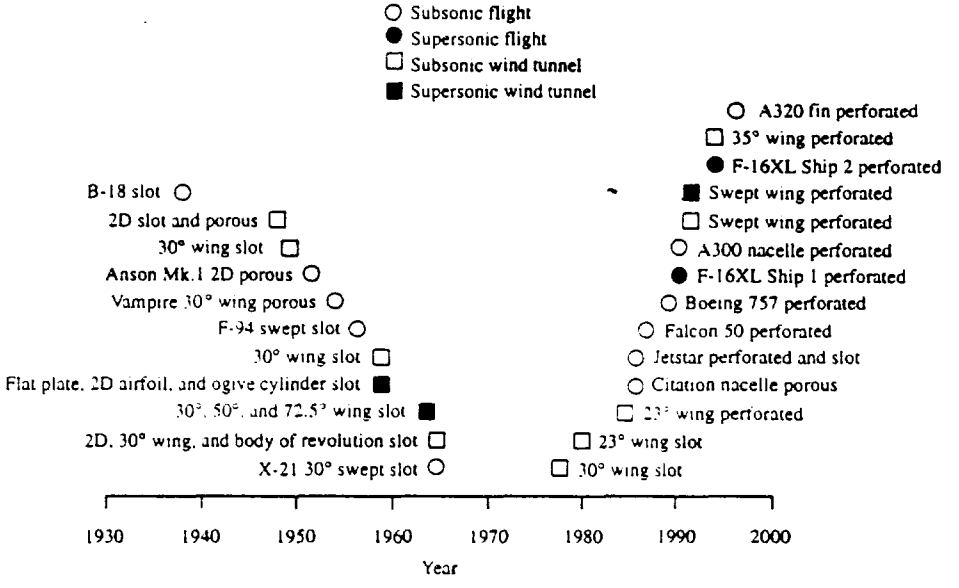

Figure 1.8: Overview of laminar flow control projects. (From Joslin, 1998).

There have been numerous wind-tunnel and flight tests performed to develop an understanding of boundary layer stability and to test the effectiveness of laminar flow control, many of which are plotted chronologically in Figure 1.8. Few of these test were performed at supersonic Mach numbers. One problem with wind tunnel experimentation is eliminating flow contamination upstream of the tunnel test section, as the Tollmien-Schlichting instabilities which lead to streamwise transition on a wing are quite sensitive to wind tunnel noise. An additional difficulty is designing tunnels with test sections capable of reaching Reynolds numbers on the order of cruise flight. The author observed a quiet supersonic wind tunnel developed at NASA Langley Research Center. It is a small pilot tunnel for Mach 3.5. In the subsonic part of the nozzle throat the boundary layer is removed to provide a fresh laminar layer in the tunnel nozzle which radiates little noise into the test section. When this layer transitions supersonically, the subsequent noise is radiated along Mach lines, leaving a quiet substantial test section [50]. Supersonic laminar flow control experiments include a 1965 supersonic wind tunnel test using slot suction laminar flow control on an 5 percent

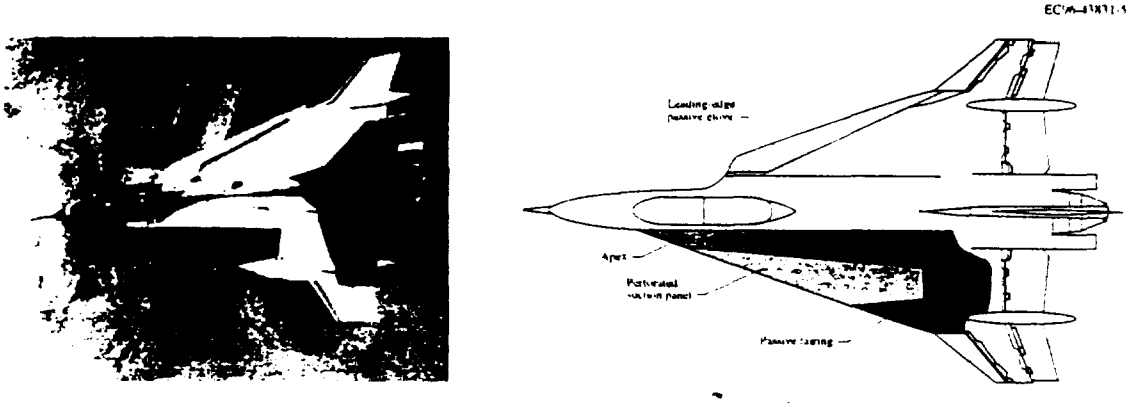

Figure 1.9: F-16XL supersonic test aircraft. LEFT: Aircraft in flight. RIGHT: Aircraft LFC component diagram. Note inboard and outboard sweeps of 70 and 50 degrees, respectively, representative of a typical HSCT configuration.

thick airfoil of 20 inches chord in which laminar flow was observed. In the early 1970s, the Laminar Flow Control project was introduced as part of the NASA ACEE Program to help improve aircraft cruise efficiency. natural laminar flow and laminar flow control projects included experiments involving the F-111 Tact, F-14 VSTEE, Boeing 757 NLF glove, laminar flow control wind tunnel tests, advanced airfoil development for natural laminar flow, and Jetstar laminar flow control flight test. There were even several laminar flow control nacelle experiments in the early 1990s [37].

In the early 1990s NASA and industry (Rockwell, Boeing, McDonnell Douglas) came together in the United States to conduct laminar flow control experiments with two F-16XL delta-wing aircraft one of which is shown in flight in Figure 1.9. The initial studies indicated that laminar flow control could reduce HSCT drag by 7% to 9%, though incurring a weight penalty from the LFC system [2]. Initially wind tunnel tests at NASA Langley Research Center (LaRC) were run on a 15-inch, 77.1 degree sweep model to support the F-16XL flight experiment and to calibrate design tools and to study attachment line instability. Traveling crossflow instabilities had the highest amplification but suction stabilized the boundary layer and kept the streamwise instabilities controlled 10 over the entire model. At NASA Ames, tests were run in the Mach 1.6 quiet tunnel to analyze freestream disturbances on a model in which a section of the passive glove for the F-16 XL was used to study the wing leading edge characteristics [37]. In 1990, focusing on attachment line instability, a perforated suction glove located on the leading 25% of the chord was flight tested on the first aircraft.

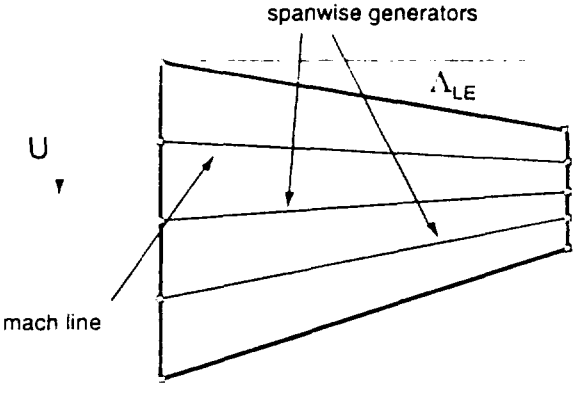

Figure 1.10: Sample NLF planform

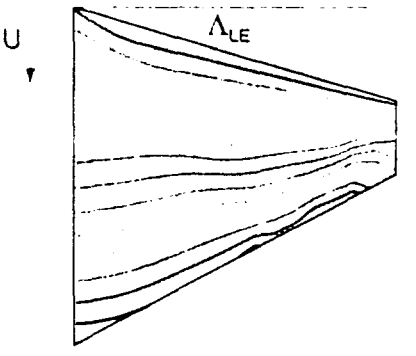

Figure 1.11: Computed isobars on trapezoidal wing. nearly-straight, low-sweep isobars indicate low crossflow. Note root and tip Mach cone effects.

No laminar flow was observed at the design point, but some laminar flow was maintained at off design conditions [37]. In 1991 and 1992 the second aircraft underwent leading edge passive glove tests. The foam and fiberglass glove, seen on the right wing in Figure 1.9 had a 4.5 meter span, and covered the first 10 percent chord. The aircraft thus fitted was flown to calibrate equipment. Subsequently the aircraft was fitted with a perforated suction glove of titanium skin and aluminum stringers (see Figure 1.9). Suction was applied to 10 million holes and 20 suction regions, with the flight test objectives to achieve between 50 and 60 percent chordwise laminar flow. This would provide CFD validation, and laminar flow control suction system criteria. The first supersonic flight of this aircraft was November 22, and the initial suction-on supersonic flight was January 24, 1996 [37].

1.3.1.2 Supersonic Natural Laminar Flow

Theory and limited experimental evidence suggests the possibility of maintaining extensive laminar boundary layers in supersonic flows without the aid of active flow control devices [77, 80]. This natural laminar flow (NLF) requires wings with a limited leading edge sweep angle lower than the Mach angle, generating isobars with little sweep and near conical flow situations. A sample planform appears in Figure 1.10, including lines between the root and tip to represent the spanwise generators. The low sweep of these generators results in limited flow along the span, reducing the crossflow Reynolds number and the growth of the crossflow instabilities. Figure 1.11 shows computed pressure contours, indicating the accuracy of the 2-D flow assumption, though weak Mach cone effects are apparent.

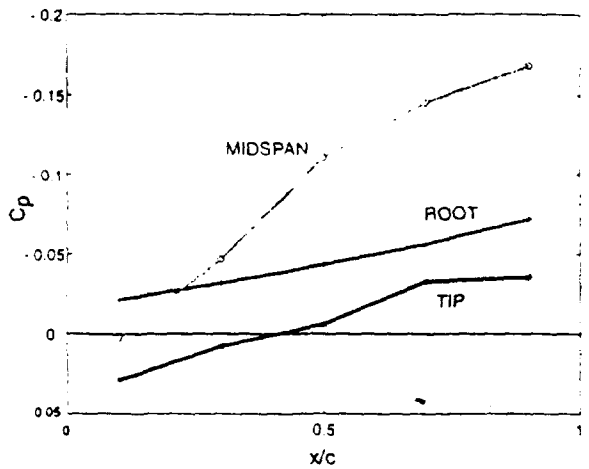

Figure 1.12: Sample surface C_p from surface panel method. Mach = 2.4, $C_L = 0.11$

The airfoil of the supersonic NLF wing has a sharp leading-edge with biconvex or modified biconvex shape and little camber, and varies little in shape spanwise. Supersonic flow characteristics over the biconvex airfoils of HSCT wing regions are shown in Figure 1.12. The chordwise distribution of pressure coefficient is nearly linear, with a quite favorable pressure gradient. These phenomena reduce the tendency of the streamwise boundary layer to transition due to critical growth of streamwise instabilities. These linear C_p plots show that this type of wing planform and airfoil design not only indicate favorable boundary layer characteristics, but also the potential for analytically predicting the flow properties with stripwise 2D or quasi-3D methods.

There are some fundamental inhibitors to attaining fully laminar flow without LFC assistance on the wing of a supersonic aircraft. Among these are the effects of the fuselage and the attachment line boundary layer. The fuselage, which transitions near the nose, emanates a wedge of turbulent flow onto the wing. The presence of the fuselage can also introduce disturbances to the wing which can prove destabilizing to the boundary layer outboard of this wedge.

To obtain a feasible supersonic natural laminar flow aircraft design in the face of these conflicting issues, multidisciplinary optimization methods *must* be employed. Tradeoffs between various design disciplines, such as aerodynamics, structures, and performance are a key element to the viability of the concept and attaining large amounts of laminar flow in practice.

Figure 1.13: F-104 sublimation test. LEFT: Upper surface. RIGHT: Lower surface. Courtesy of NASA.

In the 1950s, during the heyday of laminar flow research, techniques for detecting supersonic boundary layer transition were evaluated on F-104 wings. The aircraft was fitted with a fiberglass cloth and epoxy resin glove, and both sublimation and resistance thermometers detected transition location. Mach numbers up to 2.0 at an altitude of 50 000 ft were flown in California at the NASA High-Speed Flight Station [37]. Detailed transition analysis is not available, however Figure 1.13 show photographs of the upper and lower surface sublimation measurements. The lower surface delayed transition to 60 percent on a wing not particularly well-suited for maintaining extensive natural laminar flow. The upper surface shows the expected crossflow transition.

In the mid-1980s two test vehicles were flown in NLF experiments. An F-15, with a wing swept about 45 degrees, was fitted with a wing glove over 30 percent chord to cover wing surface imperfections and flown up to Mach 1.8, 55 000 ft. Transition was observed at 15 percent chord for Mach 1.16 ($n = 11$) and closer to the leading edge for Mach 1.76. Similar gloves were applied to a 60 degree sweep wing and the 55 degree sweep vertical tail of an F-106. Flights from Mach 0.8 to 1.8 and 30 000 ft to 50 000 ft of altitude all revealed transition within 5 percent of the leading edge [37]. It was determined that ATI contamination of the boundary layer or CFI from the large wing sweep was the cause of the poor results. For these reasons, NLF wings studied in this research are all of less than 20 degrees leading edge sweep, with supersonic leading edges.

1.4 Current Design Approach

1.4.1 Design Phases

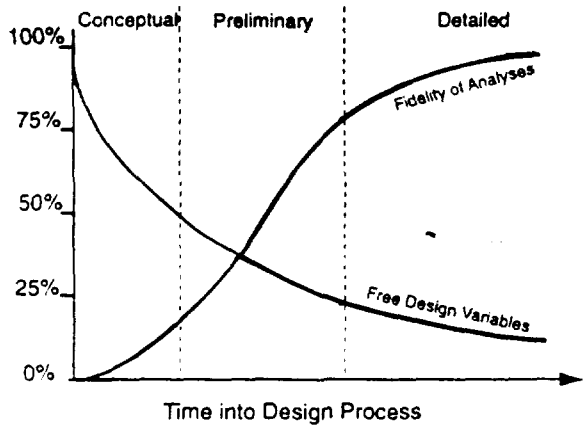

Figure 1.14: The number of free variables and the fidelity of analyses vary as the design is refined.

Figure 1.14 shows the change in the number of free design variables and fidelity of analyses with time into the design process. About eighty percent of the aircraft life cycle cost is determined at the conceptual design phase [39, 55]. The more accurate the initial analyses, the greater the potential time and money savings late in the design. The conceptual design phase often occurs after the problem has been defined and goals, constraints, and performance criteria are understood. Conceptual design is important because solution concepts are generated and evaluated at a level of detail for which there are many uncertainties. It is the beginning of a process during which engineering, science, practical knowledge, production methods, marketing and commercial aspects come together to create a valuable product [40]. At this point there are many free variables, set, and analyses in this phase are quite inexpensive to run, giving basic results. As the design moves through the preliminary phase and on to the detailed phase, the number of free variables decreases, while the fidelity of the analyses increases. Finally, only a subset of the original free variables remain as design variables of the problem. The area into which the current research falls is a function of the design goal. If the design goal is to manufacture and fly the aircraft, then research with this level of fidelity would be considered part of the preliminary design phase. If the design goal is a proof of concept or proposal preparation, then level of detail is sufficient to warrant the detailed phase. It is even quite possible to update analysis fidelity during

optimization of a design, as the optimum is approached, in order to achieve the highest possible accuracy.

1.4.2 Aircraft Characteristics and Optimization Goals

The overall goal for each aircraft optimized in this dissertation is to minimize the gross weight subject to a variety of constraints, including a 5000 n.mi. range. Selected design variables, defining the flight condition, geometry, loads, and deflections are varied in disciplines of aerodynamics, structures, mission, and performance. The optimization process is explained in Chapter 2.

The chosen value of 5000 n.mi. range corresponds to a flight from Los Angeles to Tokyo. Researchers at Boeing performed parametric studies and advanced technology assessments to show that the required TOGW is about 745 000 lb for 1990 certification. Boeing also projects that for the year 2015 certification, the required TOGW for 5000 n.mi. will be 585 000 lb. [21] The weight reduction is over 25%, a savings due mostly to more advanced structures and materials.

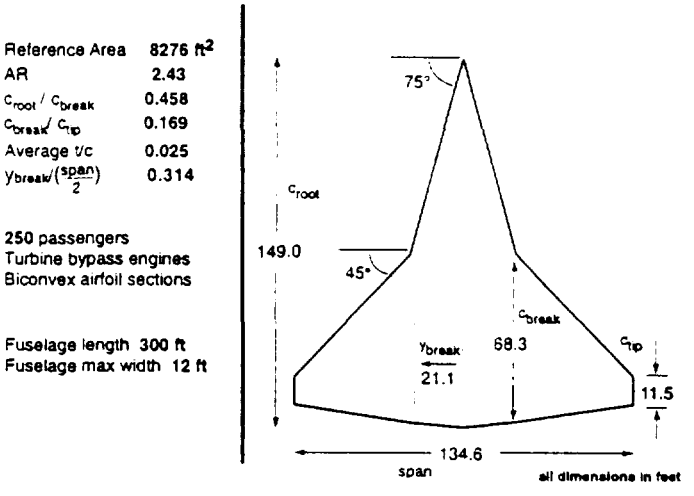

Figure 1.15: Conventional HSCT wing baseline parameters

The wing of the baseline conventional HSCT analyzed in this work is shown in Figure 1.15. This aircraft is based upon the Boeing Mach 2.4 aircraft, full details of which can be found in Reference 21. The initial wing of the supersonic NLF concept analyzed in this research is shown in Figure 1.16.

The first optimization performed in this dissertation is the conventional HSCT with a

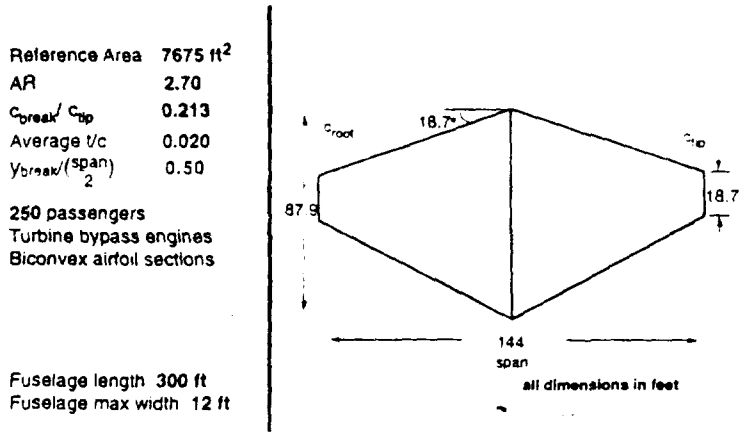

Figure 1.16: Supersonic natural laminar flow wing baseline parameters

fixed planform and fuselage design. The design variables include wing deflections, aerodynamics loads, sea-level static thrust, initial cruise altitude, lift-to-drag ratio, and take-off weight (TOGW). The converged design must be compatible between aerodynamics, structures and mission disciplines given a set of performance constraints while minimizing the weight of the vehicle. This will provide a validation of the collaborative optimization method using the highest fidelity analyses to date, and a baseline for comparison to further design reported in this thesis. The second optimization is a supersonic NLF aircraft analyzed with the same design variables. Some analyses in this natural laminar flow design are more complex, including boundary layer stability analysis, expanded structural fidelity, and more complex grid generation.

1.5 Research Contributions

Collaborative optimization is a design architecture that was developed to solve large-scale multidisciplinary design problems. [13] This thesis presents a large-scale implementation of collaborative optimization, permitting design without direct communication between high-fidelity disciplinary analyses. Collaborative optimization in this work is tailored in many ways, including application of reduced basis modeling, trust region updating, and discipline variable selection. These modifications increase the robustness of the method and reduce the number of required optimization cycles.

The analyses described herein include industry-standard codes. This level of code fidelity was chosen for many reasons. Foremost is that the true design of a large-scale vehicle is, in industry and government, handled by large teams of disciplinary experts with timelines of months or years. Though this research method is designed for application to industry, all computations and implementation here were handled by a single designers. Thus, current code fidelity gives the maximum level of accuracy and detail which allows the entire collaborative optimization process to be handled by one researcher in a reasonable time period. Also, the current level of fidelity has found its niche in the design world beyond a demonstration, as it is useful for finding starting points, and for developing proposals for new vehicles by allowing inexpensive preliminary design. Thus it is possible to think of this work in one of two ways: a complete, autonomous design, or an initial step toward a larger goal.

In previous work, collaborative optimization has been proven effective, but only with low fidelity analyses on a basic test suite of simple problems [7, 15, 62], a ship optimization [71], many wing designs [71], [13] , and a single-stage-to-orbit vehicle [13]. This dissertation shows that collaborative optimization does perform well on large-scale problems with complex codes, and illustrates this in the optimization of the natural laminar flow supersonic transport. The logical next step is application within industry.

1.6 Thesis Layout

The remaining chapters of this dissertation are organized as follows:

Chapter 2 introduces some multidisciplinary design and optimization frameworks, and details the MDO approach used in this thesis, collaborative optimization (CO). The basics of collaborative optimization, and the use of response surface estimation, are included along with specifics to large scale application. The basic design problem of supersonic aircraft optimization is also presented.

Chapters 3, 4, and 5 explain the details of the aerodynamics, structures, and mission disciplinary analyses respectively, along with problem-specific implementation.

Chapter 6 discusses the importance and details of fitting methods, or reduced-basis modeling, as incorporated into this research including explanation of all fits and response surfaces. The chapter also explores sensitivity of the discipline results to modeling accuracy.

Chapter 7 discusses the results of the optimizations of two aircraft. The design results

are presented in a manner that follows the CO process, depicting the design progression rather than simply laying out the final configurations.

Chapter 8 consists of conclusions of this research and ideas for future work.

Chapter 2

Architecture for Multidisciplinary Optimization

2.1 Introduction

In the aircraft industry, large-scale design processes are often decomposed into groups of related tasks such as aerodynamics, structures, controls, and performance. One goal of this dissertation is to demonstrate the use of a particular optimization framework, collaborative optimization, on a large-scale problem. Specifically the focus is on the design of supersonic commercial aircraft. In this work, *large-scale* refers to a complex problem with many design disciplines and many free-design variables. The goal of this chapter is to justify the use of multidisciplinary optimization in the design of aircraft, to introduce selected multidisciplinary strategies for large-scale design.

The design and optimization of a complex system such as a supersonic commercial aircraft requires pushing technology limits in all relevant disciplines. A solution will only be reached by using the tools of multidisciplinary design optimization (MDO) [70]. Geising and Barthelemy [30] give an appropriate definition of multidisciplinary optimization, stating that MDO is: " ... a methodology for the design of complex engineering systems and subsystems that coherently exploits the synergism of mutually interacting phenomena." They go on to state that: "MDO provides a collection of tools and methods that permit the tradeoff between disciplines involved in the design process. Multidisciplinary optimization is not design, but enables it."

2.2 Multidisciplinary Optimization Architectures for Large-Scale Design

Many options exist for the optimization of problems requiring multidisciplinary analysis. In fact, MDO is not a new concept, and is related to research directed toward the decomposition of problems that are heavily coupled, as in References 8 and 29. The selected optimization method can have a strong effect on the efficiency of the solution, and is extremely problem-dependent, varying with the degree of coupling, number of disciplines, fidelity of analysis codes, computing power, and even the specific optimizer. In the case of each of the architectures presented, the problem, as shown in Equation 2.1, is to minimize a selected objective function with respect to free design variables and subject to constraints.

$$\begin{aligned} Minimize &: Objective \\ With\ respect\ to &: Design\ Variables \\ Subject\ to &: Constraints \end{aligned} \tag{2.1}$$

"The size and shape of the mathematical space that contains all the design variables is very large and complex in a typical 3-D case. To find a global minimum of such a space requires a sophisticated numerical optimization algorithm that avoids local minima, honors the specified constraints, and stays within the feasible design domain." [23]

Figure 2.1 shows the interdisciplinary coupling of the analyses used in this research. Analysis inputs move vertically, and outputs move horizontally. The black dots represent information transfer. For example, the cruise aerodynamics analysis computes L/D and passes it to the mission analysis. Information transfer below the analysis boxes, such as the 1-g twist deflection, is considered feedback. In Figure 2.1, each discipline is dependent upon some result from another discipline. In some cases, feedback loops are required, as in the aeroelastic co-dependence of aerodynamics and structures through loads and deflections. In this case several iterations may be required in order to converge upon a solution before moving onto the remaining analyses. Since the aircraft system is highly coupled, it is plausible that both analysis and design should be performed using a set of integrated computer codes that solves a large system of equations governing aerodynamics, structures, trajectory, cost, etc.. This approach offers consistent computation since all boundary and interfacing conditions are incorporated implicitly [24]. A diagram of such a single-level optimization

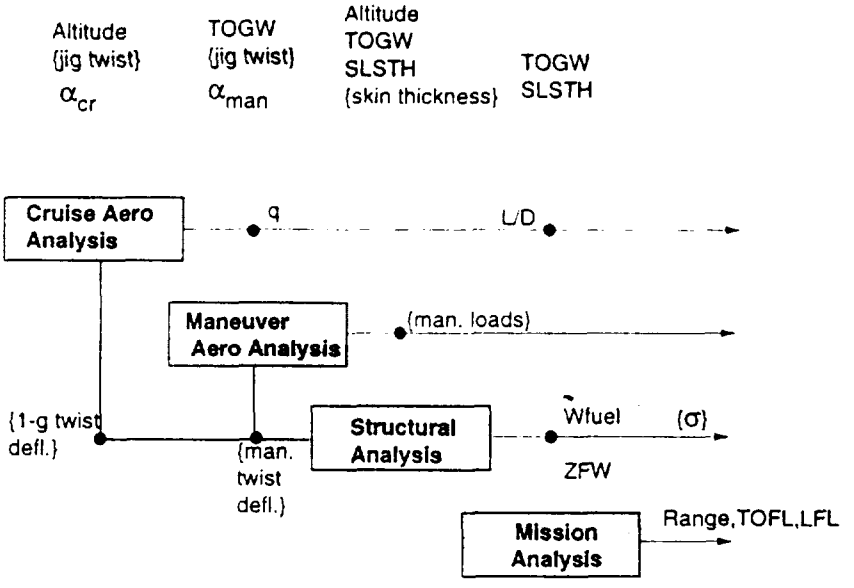

Figure 2.1: Organization of design analyses

approach appears in Figure 2.2. In this case the optimization design variables are angles of attack, jig twist, thrust, altitude, and finite-element thicknesses of the wing skin, spars, and ribs. Constraints consist of structural stress ratio, and performance values such as take-off field length, landing field length, climb gradient, and Range. During optimization, additional computed variables are passed between disciplines. Another possible way to pose the optimization problem, sequential optimization, appears in Figure 2.3. The problem has evolved into many optimizations encompassed within a system-level problem. As the overall goal is to reduce TOGW, maximizing L/D, and minimizing ZFW and aerodynamic loads on the wing are good intermediate goals. These have been set as objective functions to the appropriate discipline optimizations. As non-interdisciplinary variables and constraints are kept within the governing subproblem, the number of system-level design variables and constraints is reduced. There is still, however, necessary feedback information which will greatly affect solution time.

Some of the more successful optimization approaches use close-coupled procedures similar to those in Figures 2.2, and 2.3, however, their success depends in part on the fact that automated, fast-running analysis codes are used [30]. This may not be the most efficient approach as code fidelity increases, since the various disciplines (aerodynamics via CFD,

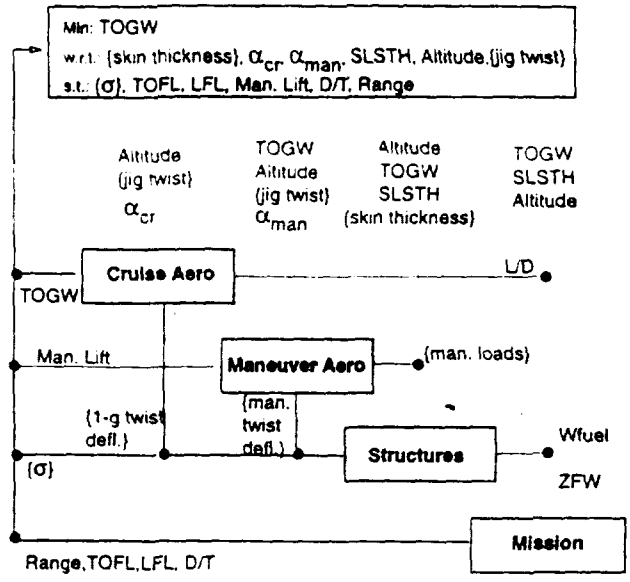

Figure 2.2: Aircraft design by single-level optimization

structures via FEM) may not converge at similar rates. In addition, all-at-once optimization eliminates the possibility of problem parallelization, which can reduce overall solution time. These optimization approaches, in fact, are unacceptable for the fidelity of analysis used in this research. A close look at the system can reveal ways in which certain disciplines are only loosely coupled with some others. The total system can then be analyzed semi-sequentially, or via coarse-grained parallelization. Such a semi-sequential approach is presently used by most researchers, but is much more prone to global instability because of the often unknown and inadequate treatment of boundary and interface conditions. [24]

Though the importance of MDO in improving the efficiency of large-scale design is accepted in the realm of academia, application in industry not widespread. One reason for this is that most demonstrations of optimization methods are performed using simple codes not representative of true design complexity. Proof of the concept for industry then, is not just a matter of accuracy and favorable results, but of modeling the industry implementation. The method which gains widespread acceptance will be one which can easily adapt to the current industry design process. It is in this area that the collaborative optimization method excels.

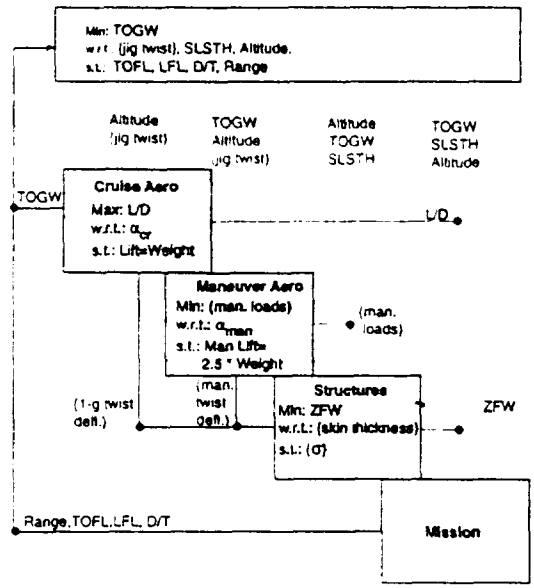

Figure 2.3: Aircraft design by sequential optimization

2.3 The Collaborative Optimization Methodology

> Design teams operating in a manually iterated synthesis environment have the advantage of using higher fidelity legacy codes, but data exchange between disciplinary analyses is often slow and cumbersome. For example, finite element structural analysis and CFD aerodynamics analysis may be conducted by different engineers on different computing platforms in different states. As a result, designs are difficult to fully optimize or even completely iterate to convergence in some cases ... New computational frameworks for collaborative design promise to combine the best features of synthesis tools and manually iterated design environments ... Disciplinary experts remain involved in the design process by setting up analysis tools, creating and modifying required wrappers, validating data ranges during the design process, and monitoring their own analysis results [58].

Collaborative optimization (CO), the method used in this thesis, is a multidisciplinary concept that preserves disciplinary level design freedom while providing a coordinating mechanism that ensures progress toward an optimum and compatibility between the disciplinary designs [74]. It deliberately mirrors the natural design process breakdown.

The collaborative optimization method is described in detail in References 13, 72, and 73. The process involves a system-level optimizer that provides a vector of target variables, $\{z\}$, to the disciplines which, in turn, execute their own optimization problems. From the subproblem standpoint, these targets $\{z\}$ are specified parameters. The subproblems minimize the discrepancy between their own local variables, $\{x\}$ and computed state variables $\{y\}$, and the system-level targets $\{z\}$ (see References 74 and 72). The system-level optimization problem in Equation 2.1 may be expressed as follows:

$$\begin{aligned} min: \; & G(z_1 \ldots z_n) \\ w.r.t.: \; & Z = \{z_1 \ldots z_n\} \\ s.t.: \; & J_i^*\{z\} = 0 \; \forall \; subproblems \end{aligned} \tag{2.2}$$

where the i^{th} subproblem optimization is given by:

$$\begin{aligned} min: \; & J_i^* = \sum_{1}^{a} (z_j - x_j)^2 + \sum_{a+1}^{b} (z_k - y_k)^2 \\ w.r.t.: \; & X = \{x_1 \ldots x_m\} \\ s.t.: \; & \{c_i\} \end{aligned} \tag{2.3}$$

where a is the number of elements in z which are inputs to the subproblem and b is the number which are computed. Figure 2.4 shows a schematic of method implementation with three disciplines.

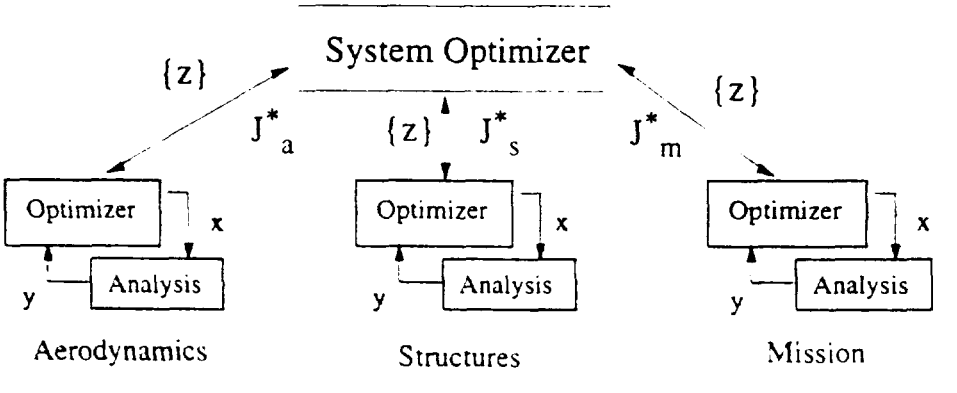

Figure 2.4: Collaborative optimization implementation for sample disciplines

	Aerodynamics	*Structures*	*Mission*
Compute:	L/D	ZFW	range
	lift (cruise and maneuver load cases)	element thicknesses (skin, rib, spar)	field lengths (take-off and landing)
	wing load distribution	wing deflections	available thrust for climb
	boundary layer transition location	wing element stresses	final cruise altitude

Table 2.1: Task summary of design subproblems

2.3.1 Organization of Disciplinary Analyses and Optimization

Regardless of the method used, large-scale computational aircraft design is accomplished by dissecting the process into groups of related tasks, and each of these design tasks can be handled by disciplinary experts. The number of groups is a function of the desired specificity of each discipline; for example, inviscid and viscous aerodynamics, structural integrity and vehicle weight, propulsion system and fuel tank placement, could each be a separate piece. Collaborative optimization is well suited for design problems in which there are many local (to each discipline) design variables and constraints, but relatively few shared, or global, variables. Active reduction of interdisciplinary coupling is desirable, and is explained in Chapter 6. For the designs in this dissertation, the chosen disciplines are aerodynamics, structures, and mission task summary of each is listed in Table 2.1. The decomposition of the aerodynamics, structures, and mission disciplines is depicted in Figure 2.5. Above each discipline box is the subset of system-level design variables that are discipline inputs ($\{x\}$ in Equation 2.3) and below is the subset of discipline outputs($\{y\}$ in Equation 2.3). The degree of coupling is apparent. Within each discipline box are the additional design variables that are local to that discipline. For each subproblem optimization then, the total design variable vector consists of the inputs from the system-level *and* the local design variables. Also inside the discipline box are the subproblem design constraints, all of which are local.

Figure 2.6 indicates the computing platforms used to perform the optimizations. Subproblem optimization is run in parallel. In an academic environment, this means that each discipline optimization could run simultaneously on different computers or processors. In industry, this means that aerodynamics and structures labs that may be in different buildings or even different states may perform their tasks concurrently without directly exchanging

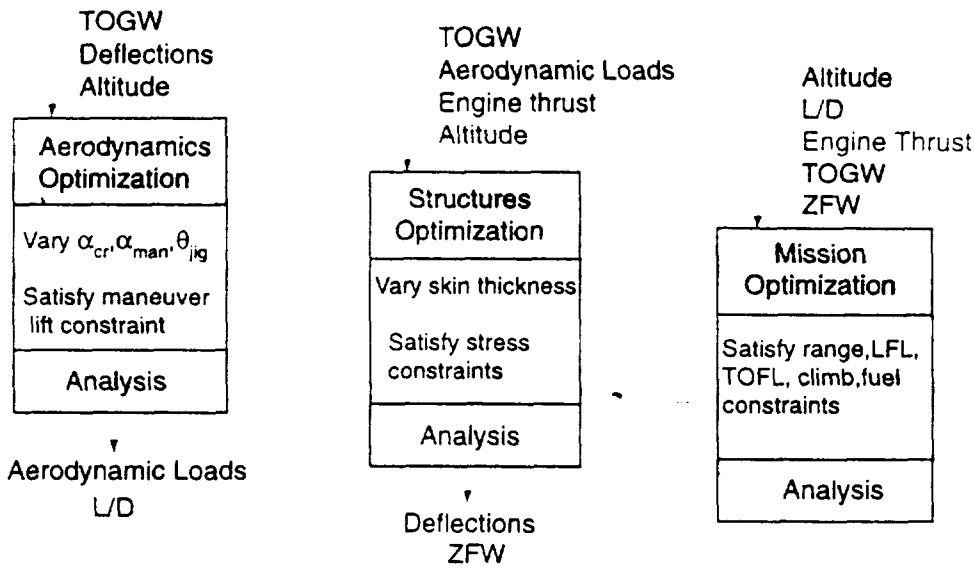

Figure 2.5: Computed results and design variables for each of the disciplinary design problems

information. Time for one system-level optimization cycle is the time of the longest subproblem optimization which itself could be run on parallel processors to reduce wall clock time.

2.3.2 Response Surfaces in Collaborative Optimization

In this design process, response surface estimation is used to model disciplinary analyses and subproblems, simplifying data transfer and reducing computation time, with minimal accuracy loss [73, 74]. In fact, response surfaces can help accuracy in the event of poor gradient information due to finite differencing of a disciplinary analysis. Gradient problems appear as numerical noise that manifests itself as low amplitude, high frequency variations in the computational results for changing values of the design variables. This noise results from representing continuous phenomena in a discrete fashion [38] and from internal iteration in the analyses. Collaborative optimization incorporates response surface fits in two ways. A response surface fit of the subproblem analysis, as shown in Figure 2.7 (a), is generated by *solving the analysis* for a set of design variables $\{x\}$, and obtaining a corresponding set *set of computed state variables*, $\{y\}$. The subproblem optimizer can use the response surface approximation in *lieu of the analysis* to minimize the subproblem objective function (J).

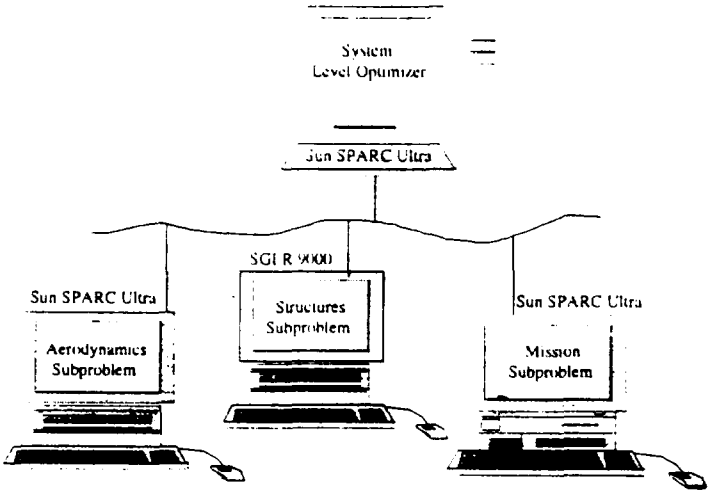

Figure 2.6: Computing platforms for the subproblem and system-level optimizations.

This approximated value of J^* is passed back to the system-level optimizer. In the results to follow, the aerodynamics analysis was modeled in this way to overcome unacceptable gradient information from the code used to generate inviscid force coefficients and wing loading. Details of the aerodynamics response surface generation may be seen in Chapter 6.

An additional approach is shown in Figure 2.7 (b), in which an entire *subproblem* can be approximated by a response surface. In this case, the response surface is generated by *solving the subproblem optimization* for a set of target variable design vectors, $\{z\}$, and obtaining a corresponding *vector of subproblem objective function values* $\{J^*\}$. The system-level optimizer then uses this response surface, *in lieu of the subproblem optimization*, to approximate $\{J_i^*\}$ as a function of the target vector, $\{z\}$ [72]. Structures and mission subproblem results were approximated in this way in order to speed the optimization at the system-level.

Incorporation of the response surface methodology of the subproblem optimizations necessitates a slightly different handling of the system-level optimization. To maximize the accuracy of the response surfaces, fits are not made of the entire possible design range, but of a local subspace, or trust region, inside which the current system-level cycle optimization will occur. The initial trust region is centered on the baseline, or target, aircraft. Since a response surface is a fit of the subproblem design space within this defined trust region, the system-level can only find a local optimum, or minimize its objective function, within this region. Each design cycle will work within a new trust region, which presumably

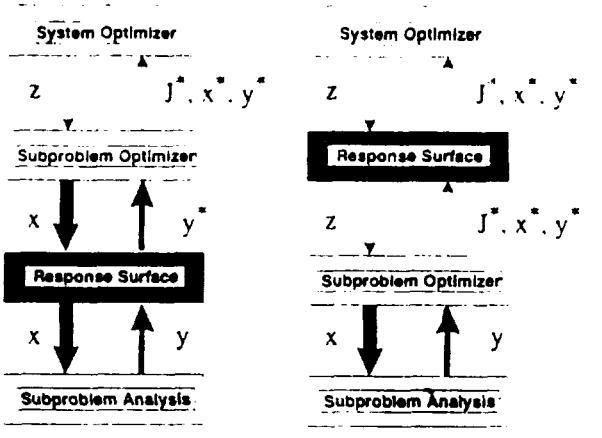

Figure 2.7: (a) Response surface models analysis, (b) Response surface models optimization

has moved closer to the global optimum. As the new point will likely be a local, and not a global optimum, the system-level optimizer must work toward convergence without enforcing the subproblems to be perfectly compatible via constraints. The compatibility process, fully demonstrated in Chapter 7, is handled by introducing a penalty function into the system-level objective. Because there is no guarantee that a quadratic response surface will contain the point for which all $J_i^*\{z\}=0$, and due to the use of trust regions, the system-level optimization problem defined in Equation 2.1 must be expressed as an unconstrained problem:

$$\begin{aligned} min: \; & G(z_1 \ldots z_n) \\ w.r.t.: \; & Z = \{z_1 \ldots z_n\} \end{aligned} \tag{2.4}$$

where G is the desired objective, for example TOGW, -Range, or cost, combined with a penalty function which will enforce compatibility as in:

$$G = -Range + K\left[\sum_{1}^{i} J_i^*(Z)\right] \tag{2.5}$$

The sum is over all subproblems. K is the penalty function scaling the emphasis on compatibility. Details of response surface generation of the analyses and subproblems of this research can be found in Sections 6.5.1 through 6.6, and the objective function used for the designs in this research is developed in Section 7.2.

2.3.3 The Collaborative Optimization Process

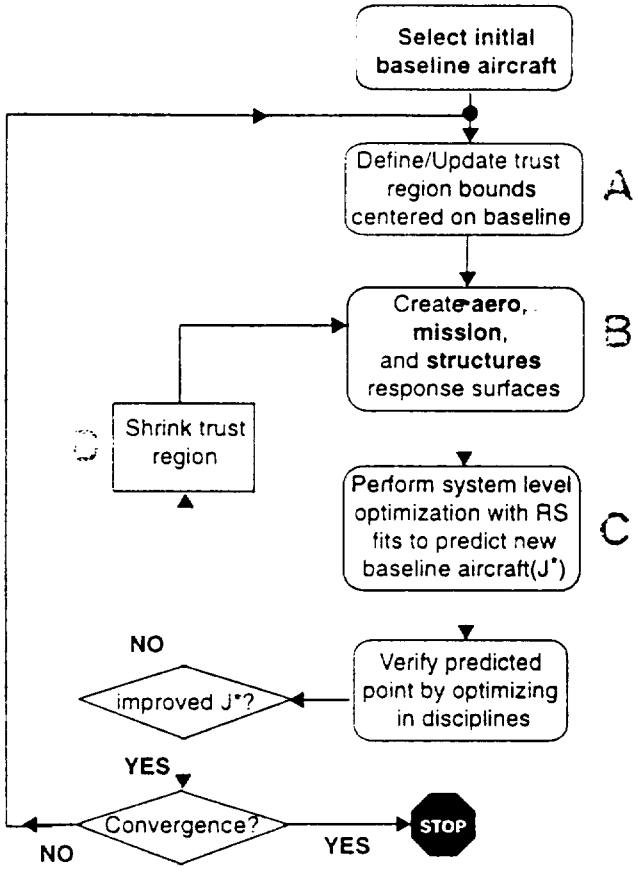

Figure 2.8: Global optimization process

This design process, collaborative optimization using response surface estimation (COURSE), is depicted at a high level in Figure 2.8. Figures 2.9, 2.10, and 2.11 expand upon the A, B, and C blocks of the global flowchart in Figure 2.8. Upon completion of the analyses and the design variable selection, the optimization process is run iteratively in four major steps: trust region definition and updating, response surface creation, system-level optimization, and new design point verification. These steps are described briefly below; further details are described in the discussion of an actual aircraft optimization process.

1) **Trust region definition** At commencement, the user must have an idea of the absolute bounds of the design variables. For example, it is possible that the maximum and minimum possible values of the design TOGW of an HSCT are 1 000 000 lb and 500

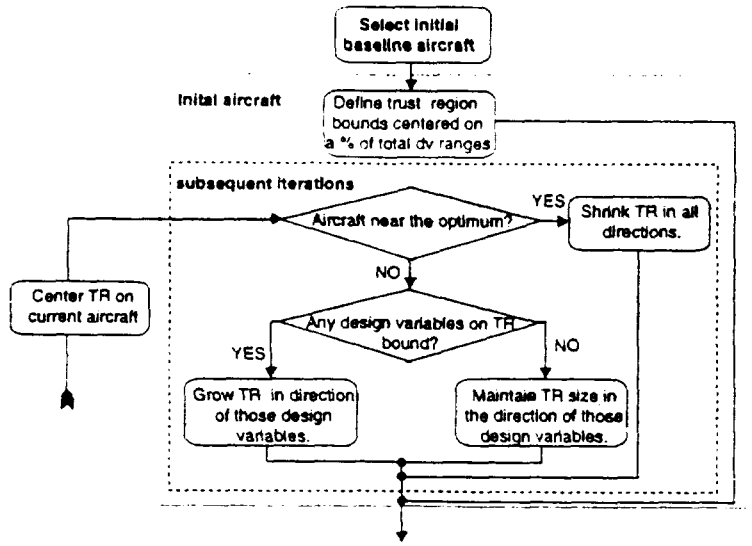

Figure 2.9: Global optimization process detail A: Trust region update.

000 lb. respectively. The optimum aircraft will, by definition, lie somewhere between these two values. Recall that each system-level cycle is composed of response surface approximations of the subproblems within a trust region for the cycle. As the cycles progress, the trust region will move, always centered upon the current design, and will change in size. After the first iteration, when the optimum aircraft inside the initial trust region has been found, any design variable which has hit the upper or lower bound of the trust region should be noted. As shown in Figure 2.9, the new trust region then grows in the direction of this design variable. For the other variables, the trust region size remains the same. This same procedure is followed in each iteration. As the system cycles progress, and the aircraft approaches the global optimum, the trust region begins to shrink in all directions.

2) **Response surface creation** As shown in Figure 2.10, upon trust region definition, response surface fits are made of each discipline. To create the fit, the required number of aircraft in the trust region is selected, and mission and structures attempt to match these aircraft in a least-squares sense via optimization. A fit of these results, the response surface, is provided to the system-level optimizer. Aerodynamics, as described in Chapter 6, is handled differently. A response surface is created of the aerodynamics *analysis*, and a subproblem optimizer which uses the aerodynamics response surface is embedded in the system-level optimization setup. Given the fits of the mission and

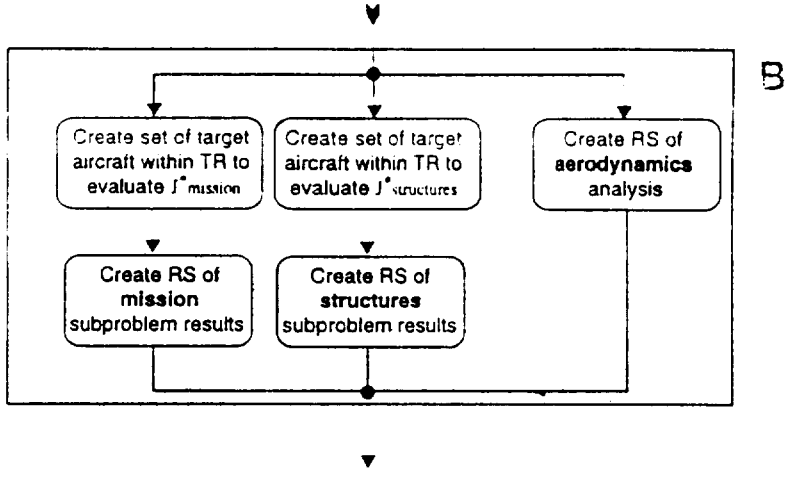

Figure 2.10: Global optimization process detail B: Response surface creation.

structures optimization results, (J^*), and the aerodynamics subproblem optimizer to determine J^* for that discipline, all of the information is available to find the optimum aircraft within the trust region.

3) **System level optimization** Figure 2.11 re-visits the system-level optimization configuration. This unconstrained problem attempts to reduce the TOGW of the aircraft and drive the interdisciplinary discrepancies to zero.

4) **New design verification** Block D of Figure 2.8 indicates action taken if there is not an improvement at the system-level during a given cycle. When the optimizer selects a new aircraft, it is the optimum design within the trust region based upon the response surface fits, and should be superior to that of the previous cycle in terms of the system-level objective function in Equation 7.2. The next step is to check the design in the *actual* disciplines, to ensure the accuracy of the fits. As the fits are quadratic, the actual subproblem answer may differ from the predicted solution if the true result is not quadratic. If the system-level objective based upon results of the actual subproblem verification runs is an improvement over the *previous* objective, then this new aircraft is accepted, made into the new trust region center point, and the next cycle is started. However, in the case of a worse design point, the design is rejected. This situation means that one or more response surface fits did not accurately represent the subproblems. Therefore, the response surfaces must be regenerated from

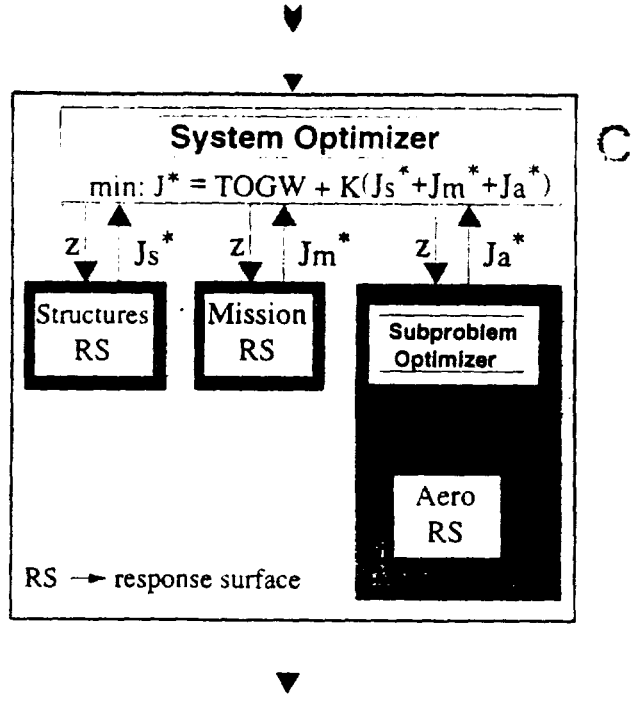

Figure 2.11: Global optimization process detail C: Cycle optimization.

the previous point within a smaller trust region. A smaller region will restrict the design from moving as far in the current cycle, but will ensure more accurate response surface fits and an improvement in the global objective. The system-level optimization and verification is then performed on the new fits, and this process is repeated until an improved design is found.

This procedure is based upon that described in Reference 6. Additional details and test cases are provided there.

Chapter 3

Aerodynamics Analysis

3.1 Introduction

Given a set of inputs such as the flight condition and wing geometry, the multidisciplinary optimization (MDO) of an aircraft requires an aerodynamics analysis module for determination of surface pressures and velocities, lift and drag. In this work, the inviscid portion of the analysis provides inputs to a boundary layer code for viscous drag computation and determination of lift-to-drag ratio. The analysis is a combination of industry-standard codes and textbook methods. A surface panel method, A502 [18,87], was chosen to calculate the wing and fuselage pressure distribution and lift coefficient, and all inviscid wing-body drag. The remaining inviscid drag calculations, as well as the engine, fuselage and tail parasite drag, are based largely upon the methods used in the Program for Aircraft Synthesis Studies (PASS) [41]. Preparation of geometric data for input to A502 can be a tedious, expensive task; therefore an automated process was developed to create the wing-body combination from a number of fixed parameters and optimization design variables. As the success of this aircraft depends upon the extent of attainable laminar flow, it is essential to have a viscous model that captures the properties of the streamwise and crossflow boundary layers, allowing for transition calculation. This portion of the analysis consists of a finite difference compressible boundary layer code along with an auxiliary analysis code to compute crossflow properties. The goals for a boundary layer analysis to be used within a design optimization framework are threefold:

(1) Reasonably accurate calculation of skin friction.

Load Cases	n	Mach Number	$q(lb/ft^2)$	% fuel
Cruise	1	2.4	535	50
Transonic climb	1	1.2	644	90
Low-speed pull-up	2.5	0.6	367	95
High-speed pull-up	2.5	2.4	723	80
Taxi	1.5	0	0	100.0

Table 3.1: Load cases

(2) Sufficient modeling to enable approximate boundary layer transition prediction.

(3) Very low computational expense.

Navier-Stokes codes provide the most accurate simulation of boundary layer activity on aircraft wing-body combinations. There are reasons to avoid such codes in this situation. One is item (3) above. As the design process of these aircraft involves multidisciplinary optimization, there are many function evaluations required in a reasonable period of time. Although the disciplinary optimizations are run in parallel on separate machines, some CFD methods are still far too expensive to use in the conventional manner for the MDO task considered here.

3.2 The Aerodynamics Design Problem

3.2.1 Design Cases

Five aircraft load cases are listed in Table 3.2.1. It is possible to analyze many design conditions with collaborative optimization, but to ensure a problem manageable by one designer, only two are selected. The critical condition chosen for analysis in addition to the cruise condition is that of the high-speed pull-up. In the aerodynamics analysis, the flight conditions differ in two ways: angle of attack and wing deflections. The cruise deflections are comprised of the jig twist and 1-g structural deflections, while for the maneuver condition, the total deflections are a combination of the jig twist and the 2.5-g structural deflections. The loads applied to the structural model, then, are the aerodynamic loads computed in the maneuver flight condition added to the inertial weights of the aircraft structure. As explained in Section 4.7, the fuel and wing inertial weights are applied as a distributed load over a selected portion of the wing structure, and the propulsion weight as point loads in representative locations.

This aeroelastic coupling is represented in Figures 2.1 through 2.3, and for collaborative optimization, in Figure 2.5. Traditionally, convergence of the aeroelastic solution requires iteration between tightly coupled aerodynamics and structures codes, but collaborative optimization, as will be shown in Chapter 7, converges this solution without direct communication between the two disciplines.

3.2.2 Flow of the Aerodynamics Analysis

Figure 3.1 is a schematic of the flow of the aerodynamics discipline, showing the separate solution of the cruise and maneuver conditions given the inputs, and the values computed by aerodynamics. Given the planform geometry, built-in jig twist, altitude, and angle of attack, the lift distribution, total lift, and drag are computed. In the cruise condition, the outputs are aircraft lift-to-drag ratio and the cruise lift. Subsequently, the maneuver condition computes the maneuver lift, and the maneuver wing loads, which are compressed into spanwise distributions of bending moment and torque. Further details on the method for computation of spanwise bending moment and torque distributions from the wing pressure distribution are given in Section 6.2.

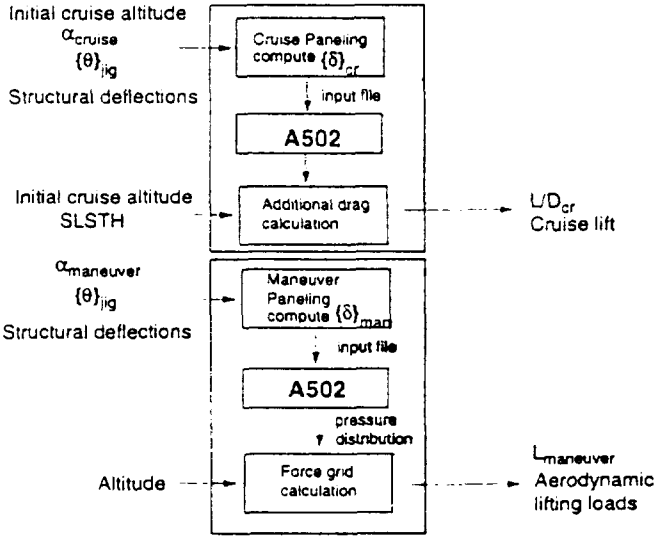

Figure 3.1: Organization of aerodynamics discipline analysis

3.3 Aerodynamics Modeling

The goal for geometric modeling is to develop an automated process creating the wing-body combination from a number of fixed parameters and optimization design variables. The process consists of an initial definition of the components, a coarse paneling, paneling refinement (increasing grid density), and computation of intersection curves in order to create a single wing-body unit for analysis by a full potential code. Once the unit is defined, wing and body wakes must be added. A package was created and incorporated into the aerodynamics analysis, making it possible to run cases automatically from input, through the geometry generation and flow calculations. This process significantly reduces the time and expense involved in making the three-dimensional potential-flow calculations.

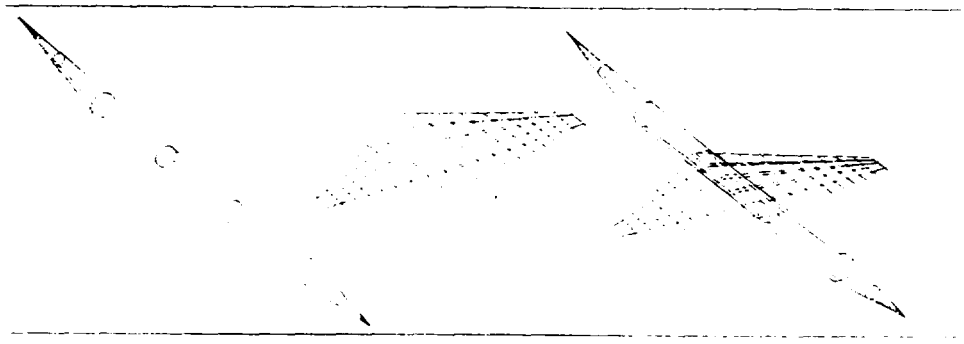

Figure 3.2: Sample wing and fuselage components coarsely paneled from design variables

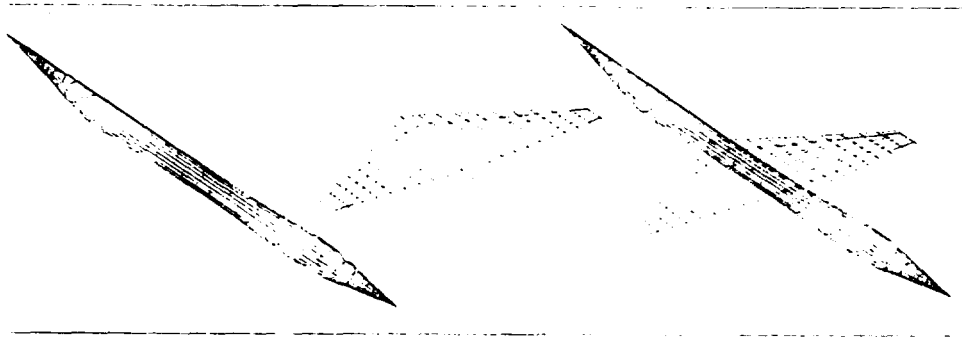

Figure 3.3: Sample wing and fuselage components re-paneled for a finer grid

An aircraft wing, seen with a fuselage in Figure 3.2, is initially created from a limited number of variables. Among the wing inputs are: thickness-to-chord ratio, wing area, span, taper ratio, and leading edge sweep. Initial fuselage definition is from overall length, nose

and tail fineness ratios, diameter at the base of the nose and tail cones, diameter at points along of the fuselage, and amount of fuselage tail upsweep. A panel code such as A502 is sensitive to unit normal direction of each panel, so at this step care must be taken to ensure that unit normals point outward. The original grid density may consist of coordinate data with even an order of magnitude fewer points than that required for the actual potential code calculations. The wing-body combination is then run in the code Binter [35], which refines the initial geometry grid according to inputs defining the desired grid density and nodal distribution. The repaneled sample is shown in Figure 3.3 where it can be seen that the wing cuts through the fuselage in such a way that the grid points do not match along the intersection. The former will lead to inaccurate results, and the latter will not run in any surface panel method. A view of the wing-body intersection shown cut along the symmetry plane is shown in Figure 3.4.

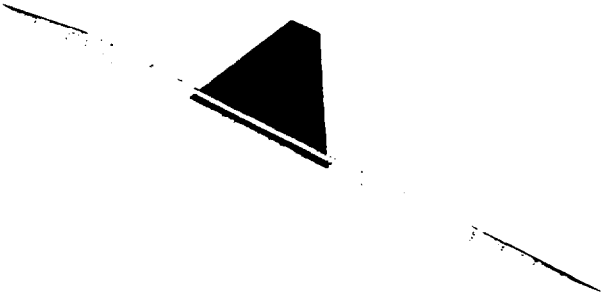

Figure 3.4: Intersection of wing and fuselage. Note grid points on wing and fuselage do not match.

Figure 3.5: Wing-fuselage intersection and cutout

The repaneled grid is altered again, keeping constant the current paneling. The purpose is instead to compute the intersection curve between the wing and fuselage, and to "sew" the pieces together, ensuring grid point matching along this portion of the model. Therefore, the intersecting components are repaneled such that adjacent elements on either side of the

intersection curves line up satisfactorily for the potential code. These curves of intersection between components are calculated using a hybrid curve-fit/surface-fit approach. The total

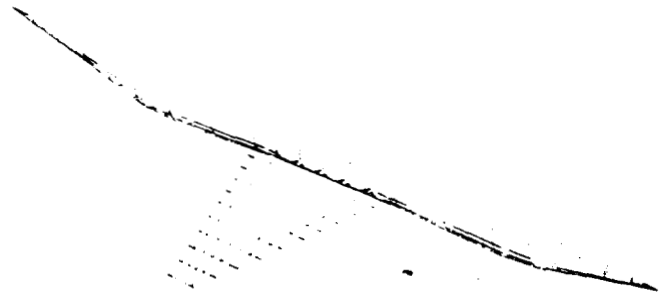

Figure 3.6: Final wire-frame of model including wing and body wakes

number of cuts along the fuselage from nose to tail remains the same. The wing paneling may change in that any "strip" of panels which was fully inside the fuselage is truncated. Figure 3.5 shows the newly intersected portion of the model, along with a view of the fuselage with a wing cut-out. The last step in preparing the model for a run in A502 is the addition of wing and body wakes. In the case of A502, semi-infinite wake filaments are added to the trailing edge of the defined grid, so the wake is only physically paneled to the rear of the fuselage. The final wire-frame of the model is shown in Figure 3.6, cut along the symmetry plane.

Upon combining the final grid with auxiliary flight condition data, such as Mach number, angle of attack, reference data, and boundary conditions, the surface panel method A502 is run and returns surface pressures and force coefficients. A sample result of surface pressures is shown in Figure 3.7.

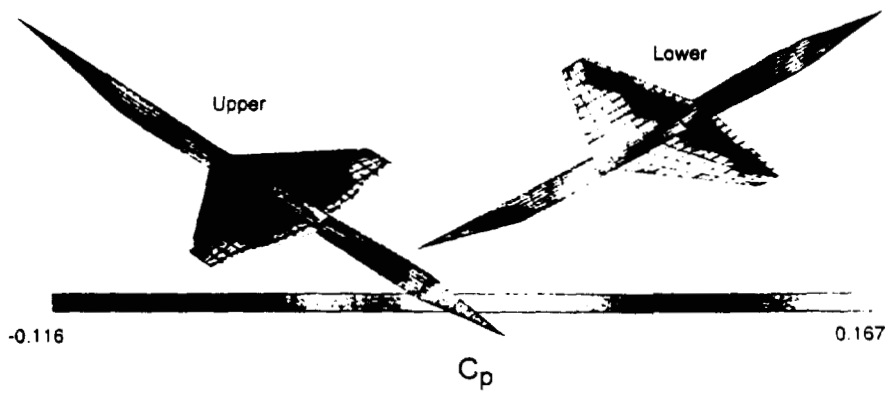

Figure 3.7: Pressure coefficient on model.

3.4 Inviscid Aerodynamics Analysis

When selecting a code for inviscid aerodynamics analysis, many methods were investigated, from 2-D strip theory, to lower and higher-order panel methods, to Euler codes.

Supersonic panel methods solve the linearized Prandtl-Glauert equation for inviscid, irrotational flow.

$$(M_\infty^2 - 1)\,\phi_{xx} + \phi_{yy} + \phi_{zz} = 0 \tag{3.1}$$

This equation is not accurate in the transonic regime, and depends upon the assumption of small disturbances. Within the limitations of the Prandtl-Glauert equation, the higher-order distributions used in methods such as the Boeing code, A502, allows surface paneling models to be used for supersonic flow. Lower-order codes such as the Woodward-Carmichael code, usually use a flat "average" panel to define corner points. This causes gaps to exist between the edges of the adjacent panels. Flat panels leak rather badly everywhere except at the control point where the discrete boundary conditions are imposed. A502 uses four triangular subpanels and a flat interior parallelogram in part to avoid this leakage. Also the numerical solutions are less sensitive to size, shape and arrangement of panels than in earlier methods, although the code will not run if panels are inclined highly to supersonic freestream flow. The higher order singularity distributions require much more analytic work to derive the influence-coefficient equations, and demand many more arithmetic operations then the simpler lower-order (constant-strength) methods, resulting in higher run costs [27]. Despite the cost, due to the increased accuracy and reliability of the higher-order methods, and because A502 has been used extensively at Boeing and NASA on complex configurations in subsonic and supersonic flows, the surface panel method was selected over the simpler options.

Euler methods are somewhat more trusted in industry than surface panel methods. The Euler equations are much more versatile than the Prandtl-Glauert, and though inviscid, Euler methods can analyze rotational and transonic flows. Not linearized, the Euler equation also has the capability to capture strong shocks. For these reasons, A502 and the Euler code FLO-107 were run on the same wing in order to compare pressure distributions. Validation is important, as the aerodynamic loads become system level variables and thus affect other disciplines. Accuracy of any given code will affect the resulting aircraft design. Wing geometry and flight condition parameters of the test planform are:

Agrawal Wing Geometry and Flight Condition			
Parameter	*Value*	*Parameter*	*Value*
$S\ (ft^2)$	529.3	$h\ (ft)$	40 000
$c_{root}\ (ft)$	22.5	$Mach$	2.0
$b\ (ft)$	37.9	$\alpha\ (deg)$	4.0
$\Lambda_{LE}\ (deg)$	32	AR	2.71
λ	0.242	t/c	0.05

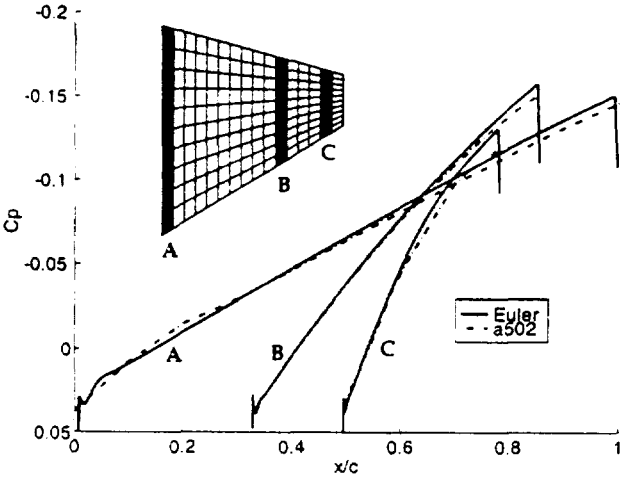

Figure 3.8: Upper surface C_p on Agrawal wing, A502 and Euler (FLO-107) results.

The chordwise pressure coefficient at various spanwise stations of this geometry appears in Figure 3.8. Reinforcing the claim of rather linear chordwise C_p distributions, the results agree quite nicely. In order to save computation time, the aerodynamics analysis were run on the coarsest grid that provides acceptable accuracy. The Euler grid consisted of 97 chordwise points and 49 spanwise, while the A502 results were generated from a much coarser grid, 11 chordwise and 17 spanwise stations. In the Euler result in Figure 3.8 nonlinearities can be seen that are not present in the A502 result. The spikes and waviness in the pressure coefficient appears due to the manner in which the Euler method handles the leading and trailing edge computations and is a function of grid density. Numerical noise such as this can cause problems in boundary layer transition analysis, as the boundary layer code depends upon pressures from the inviscid analysis to compute properties of the viscous flow field.

As A502 compares favorably with the Euler code on the geometries in this research, and since the modeling and computational expense is much less for the surface panel method, A502 was chosen as the inviscid aerodynamics code. However, collaborative implementation is well suited to handle code substitution if necessary. The procedure for altering a discipline in the collaborative optimization process is fairly non-invasive as this change does not affect other disciplines, so long as the expected subproblem outputs can be computed from the given system level variables.

3.5 Viscous Aerodynamics Analysis

In some codes used for high-lift design, 3-D panel codes are coupled with 2-D boundary layer codes, thus capturing the correct 3-D pressure distribution, but ignoring the effect of crossflow on the boundary layer [16]. This is common practice, which can be insufficient in the case of transition prediction, as it is possible that the boundary layer transition will at times be crossflow-critical. One of the reasons for the low sweep of the supersonic natural laminar flow wing is to reduce this physical phenomena, so the benefits must be shown through some sort of crossflow property analysis. In multidisciplinary optimization however, the implementation of a full 3-D CFD model would be prohibitively expensive, so a compromise must be made. While keeping the computational costs reasonable, some of the boundary layer properties in the spanwise direction must be captured, such as the crossflow Reynolds number. The fact that the wings analyzed in this research are simply swept lends a hand. The viscous and inviscid computations are performed independently, with the boundary layer code taking the inviscid local flow properties as inputs, and the crossflow analysis developed incorporating supersonic theory and empirical results.

3.5.1 Streamwise Boundary Layer Analysis

Equation 3.2 governs 2-D compressible boundary layer flow.

$$\begin{aligned}
\text{Continuity}: &\quad \frac{\partial \rho}{\partial t} + \frac{\partial}{\partial x}(\rho u) + \frac{\partial}{\partial y}(\rho v) = 0 \\
\text{x momentum}: &\quad \rho\left(\frac{\partial u}{\partial t} + u\frac{\partial u}{\partial x} + v\frac{\partial u}{\partial y}\right) \approx -\frac{\partial p_e}{\partial x} + \frac{\partial}{\partial y}\left(\mu\frac{\partial u}{\partial y}\right) \\
\text{y momentum}: &\quad \frac{\partial p}{\partial y} = 0 \\
\text{Energy}: &\quad \rho\left(\frac{\partial h}{\partial t} + u\frac{\partial h}{\partial x} + v\frac{\partial h}{\partial y}\right) \approx \frac{\partial p_e}{\partial t} + u\frac{\partial p_e}{\partial x} + \frac{\partial}{\partial y}\left(\kappa\frac{\partial T}{\partial y}\right) + \mu\left(\frac{\partial u}{\partial y}\right)^2
\end{aligned} \tag{3.2}$$

For the designs in this dissertation, the streamwise variations of boundary layer properties are computed by a finite-difference boundary-layer code [11] run in stripwise 2-D mode. This code receives edge velocities from the panel method, capturing the correct 3-D pressure distribution along a given 2-D strip, and returns the streamwise boundary layer properties.

Temperature differences in the boundary layer of high speed flows are generated by viscous dissipation of kinetic energy. A constant pressure high speed shear layer is equivalent to a low speed flow in which distributed heat sources within the fluid replace the energy dissipation [11]. The relation between coupled (compressible) and uncoupled (incompressible) boundary layers is as follows: the compressible shape factor $H = \frac{\delta^*}{\vartheta}$, or the ratio of displacement thickness to momentum thickness, increases with Mach number, as the viscous dissipation of kinetic energy into heat raises the temperature and lowers the density near the surface, so $\frac{\rho}{\rho_e} < 1$. As a result, $\int_0^\infty \frac{\rho u}{\rho_e u_e}\left(1 - \frac{u}{u_e}\right) dy$, the momentum thickness (θ), is a smaller fraction of $\int_0^\infty \left(1 - \frac{\rho u}{\rho_e u_e}\right) dy$, the displacement thickness (δ^*), than if $\frac{\rho}{\rho_e} = 1$. [11]

The shear stress in a 2-D thin shear layer is defined by $-\overline{\rho u' v'}$, which is one of six Reynolds turbulent stresses in a shear layer. In 2-D, w and $w' = 0$. In general, $-\overline{\rho u_i' v_j'}$ acts in the x_i direction on a surface perpendicular to the x_j direction. $-\overline{\rho u' v'}$ is the rate of turbulent transfer of x-component momentum in the y direction. Thus as density decreases, this quantity decreases, which corresponds to a decrease in momentum, which agrees with the earlier description of an increase in the shape factor as Mach number and temperature increase. It is known that by nature, compressible boundary layers are more stable than their incompressible counterparts. This is due in part to heat transfer effects and pressure gradient effects in compressible flow.

In a compressible boundary layer, at least four additional quantities (density, viscosity,

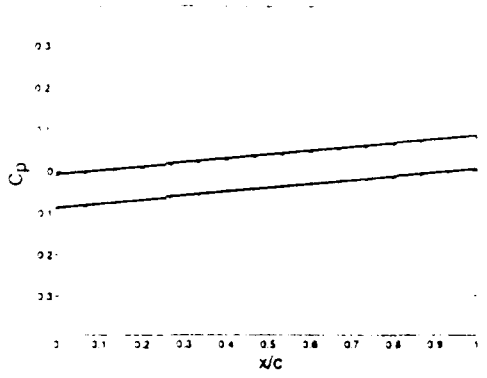

Figure 3.9: Upper and lower linear Mach 2 pressure distributions for a lifting for a biconvex airfoil.

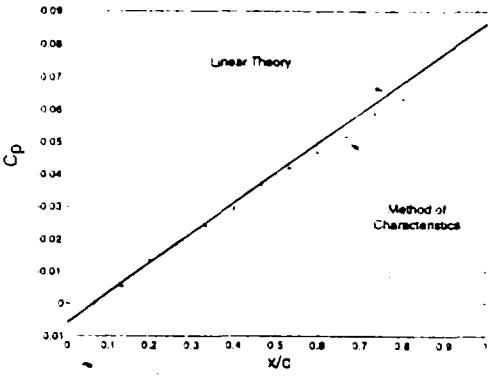

Figure 3.10: Pressure distribution from linear theory and from method of characteristics at Mach 2

temperature and rate of heat transfer) must be considered in addition to those in incompressible flows. Thus, a parameter that is connected with the rate of heat transfer between the fluid and the wall must be considered [67]. When the fluid is incompressible, heat can exchange only if the wall temperature is originally higher or lower than the fluid temperature. When the fluid is compressible, however, heat evolved in the boundary layer produces a thermal boundary layer in addition to the velocity boundary layer. This additional parameter plays a part in stability, as transfer of heat from the boundary layer to the wall can now occur regardless of the initial relative temperatures. Generally, heat transfer from the fluid to the wall has a stabilizing effect on the boundary layer, which is why wall cooling helps avoid transition due to TSI growth. The details of heat transfer effects, and the procedure to specify the handling of these effects in the boundary layer analysis are expanded in Appendix A.3.

Pressure gradient effects govern the streamwise development of the boundary layer as well. As the freestream flow increases in Mach number, the pressure gradient on an airfoil changes shape, becoming favorable and nearly linear in the low supersonic regime. Figure 3.9 shows the upper and lower pressure distributions of a parabolic biconvex airfoil at Mach 2 (along with linear fits). Figure 3.10 shows the difference between the upper surface pressure distribution calculated by linear theory and by the more accurate method of characteristics.

The pressure gradient in this case is fully favorable along the entire chord. As there is no adverse pressure gradient, any inviscid instability due to inflection in the velocity profile will be due to heat transfer from the wall to the fluid. For low supersonic Mach numbers,

which are the range of interest of this work, higher-mode disturbances are not expected to be dominant. Transition then, will be caused by the growth of either streamwise 2D Tollmein-Schlichting (TS) waves or crossflow instability in the boundary layer.

3.5.1.1 Streamwise Boundary Layer Transition Prediction

Boundary layer transition is one of the most poorly understood aspects of fluid dynamics, however, semi-empirical methods are sufficient to capture the general behavior of the transition front necessary in the drag-structures-mission tradeoffs of NLF supersonic transport design. As more experimental data becomes available, more sophisticated techniques can be substituted in the general framework developed in Reference 77 and used in this design process.

$$[\phi'''' - 2\alpha_l^2\phi'' + \alpha_l^4\phi''] = iR[(\alpha_l\tilde{u} - \tilde{\omega})(\phi'' - \alpha_l^2\phi) - \tilde{u}''\alpha_l\phi] \tag{3.3}$$

The Orr-Sommerfield equation, derived in Appendix A.1 and shown in dimensionless form in Equation 3.3 governs the growth and decay of infinitesimal wavelike disturbances in two dimensional (2-D) or three dimensional (3-D) shear layers. Useful because unstable growth of disturbances is a precursor to free transition in boundary layers, the Orr-Sommerfield equation is derived from the unsteady Navier-Stokes equations with the thin shear layer and parallel flow simplifications. The thin shear layer assumptions include steady 2-D flow, the dominant diffusion layer in the cross stream direction, and parabolic flow (flow uninfluenced by downstream events). In addition, the Reynolds stress is significant only in these shear layers. The parallel flow assumption states that the local velocity in the y direction, $v(y)$, is zero while those in the x and z directions are not.

The problem of boundary layer stability is an eigenvalue problem of Equation 3.3.The Orr-Sommerfield equation is based upon the assumption that the disturbance resulting from the instability of a shear layer is a 2-D sinusoidal traveling wave whose amplitude is growing in space (as usual in boundary layers) or time, or both. The real parts of the terms in the exponential in the disturbance represent the growth rate, while the imaginary parts represent the frequency and wavelength of the (sinusoidal) oscillation. These, together with the Reynolds number, are the eigenvalues. Either temporal or spatial theory is used in the solution process. Temporal theory is concerned with the evolution over time of an initial disturbance in a given neighborhood. Spatial theory is concerned with the evolution of a

disturbance of fixed frequency as it moves downstream of a source, and is applicable to the boundary layer analysis of interest. If the Reynolds number, wavelength, and the frequency (or equivalently the phase velocity = (wavelength x frequency)) are set, the spatial growth rates are determined: finding them is the eigenvalue problem. The amplitude and relative phase ϕ, the eigenfunction, vary across the layer. For spatial amplification theory, the resulting solution will be a function of (Re, α_i,α_r,ω)=0. There will exist one eigenfunction and one complex eigenvalue α for each pair of values ω, R. The OS is a linearized equation so only sinusoidal oscillations are meaningful - it only holds for early stages of transition, the initial stages of disturbance growth.

Compressible e^n stability theory and the Orr-Sommerfield equation are the basis to find the streamwise Tollmien-Schlichting amplification envelope as a function of Re_ϑ, Mach number, and shape factor. According to the theory of the e^n method, transition starts when a small disturbance introduced at a critical Reynolds number has amplified by a factor of e^n. There is some discussion in industry as to the correct value of n, but one generally accepted value is 9, and is used for the analysis in this research. The method is wholly empirical, as there is an empirical correlation for the length of the transition region of a boundary layer in a low-turbulent stream. Obviously, high amplification rate will imply a short transition region, as the integrated value of e^n will occur at a lower x value.

Once the spatial amplification rates of the disturbance are determined, the e^n method can be applied, which involves integrating the rate to obtain an amplification factor. For each disturbance frequency applied to the OS equation, a respective amplification rate is integrated from the neutral stability point to a downstream location in order to obtain the amplification factor as in Equation 3.4.

$$n = \ln \frac{A}{A_o} \tag{3.4}$$

$\ln \frac{A}{A_o}$, defined as the log of the ratio of the magnitude of the disturbance at x to its value at the defined neutral point, is the "n" in the e^n method. A_o is the value on the lower branch of the neutral curve and A is the local amplitude. $n = 9$ includes the effects of a density gradient, $\ln(x)$, wall temperature and concave curvature.

Given the velocity profile $U(y)$, the viscosity (from $Re = \frac{u_e \delta}{\nu}$), and the wavelength (real part of α), there is a certain frequency ω (or c) for which the amplification in x , α_i, is a maximum. This frequency which produces a maximum amplification is considered the "most

unstable frequency". The growth rate of the disturbance with the most unstable frequency downstream from the point of instability is the one integrated to obtain the amplitude of that disturbance. A homogeneous, linearized equation, Orr-Sommerfield will only predict the most-unstable eigenvalue (that is, the frequency, if the wavelength is prescribed) and the initial stages of disturbance growth.

The boundary layer formulation used in the transition region is derived from intermittency-weighted averages of laminar and turbulent correlations [11]. A locus of neutral points (spatial amplification rate $\alpha_i = 0$) forms the boundary between stability and instability. (Incidentally, spatial and temporal stability characteristics are the same for neutral stability). This neutral stability curve is the boundary of the region in which low Reynolds number ($Re_\delta = 1000$) infinitesimal disturbances are amplified. The disturbance is a function of y only, and the last term in the Orr-Sommerfield equation is symmetric - it is the viscous diffusion term in the vorticity transport equation, and so appears as fourth derivatives of the stream function (see Appendix A.1).

The solutions $U(y)$, the boundary layer velocity profiles, which generate eigenvalues, are eigenfunctions. The equation is used to perform stability analysis on laminar boundary layers, given $U(y)$, numerically. Ideally, one wants to work with a velocity profile which is constant in shape throughout the boundary layer. Only if the flow is similar will $U = U(\eta)$ not be a function of x (will not change as one moves downstream). If the flow happens to be non-similar, each streamwise location of $U(y)$ is determined numerically and is given a specified Reynolds number at that x location and the rate α_i is obtained for each ω (disturbance frequency) considered.

The hope is to use this method of the Orr-Sommerfield equation in conjunction with the e^n method to predict if and where transition will occur. Amplification rates predicted in this manner can, in fact, give a rough estimation of the point of downstream transition. The disturbance waves are Tollmien- Schlichting waves, which are the first indication of laminar instability.

The critical Reynolds number varies with the distance from the surface, roughness, vibration, and pressure distribution. Above the critical Reynolds number, the disturbances are not damped by viscosity, but are amplified until the laminar character of the flow disappears. Transition occurs downstream from the x station at which the critical Reynolds number is encountered.

Given this information, how is it known that the boundary layer will transition at all?

As proven in Section A.2, it is sufficient for instability that $U''(y) = 0$ somewhere in the velocity profile, at a point of inflection. This is the case for a laminar boundary layer in an adverse pressure gradient or for compressible laminar boundary layer undergoing heat transfer from the wall to the fluid. The disturbance has some constraints, in that it is a function of ϕ, and $u = \frac{\partial \phi}{\partial y} \equiv u(y)$ so $u'' \equiv u''(y)$, therefore $\phi \equiv \phi(y)$. In addition, each of the eigenvalues is the same in the y direction at a given x direction.

As the Orr-Sommerfield equation is fourth order, the solution process can be quite tricky. One method is to reduce the effective order of the equation set. To get a numerical solution of 2-D flows, a first-order system of equations and boundary conditions can be developed. Central-difference equations for this set are written, and the resulting system is converted to matrix-vector form and solved by the block-tridiagonal elimination method. Borrowing from the ideas of Drela [22], 2-D linear-amplification ratios (n) are predetermined for all important frequencies and arranged as amplification envelopes for various shape factors and Mach numbers as functions of momentum thickness Reynolds number (Re_θ). Algebraic fits to these envelopes are used during the boundary layer calculations to sum amplification ratios (n) very quickly, and the generally accepted value of $n = 9$ is considered the starting point of transition. The fits used for analysis in this dissertation are essentially those of Drela with a temperature ratio correction. The correction is based upon e^n calculations on biconvex airfoils at flight conditions spanning the range of interest for HSCT analysis [77]. The resulting fits, for which the equations are developed below, are compared to e^n calculations in Figure 3.11. The fits, developed in the Aircraft Design Group at Stanford University, are scheduled to be compared with a full 3-D e^n stability code [45] and enhanced for future calculations.

Defining n:

$$n = \int_{Re_{\theta_o}}^{Re_\theta} \frac{dn}{dRe_\theta} Re_\theta \tag{3.5}$$

where Re_{θ_o} is the point at which the Tollmien-Schlichting waves begin to grow and defined in Reference 22 as a function of shape factor. Here it is taken in Reference 77 as:

$$Re_{\theta_o} \approx 700 \left(\frac{T_w/T_e}{1.9} \right)^{0.7} \tag{3.6}$$

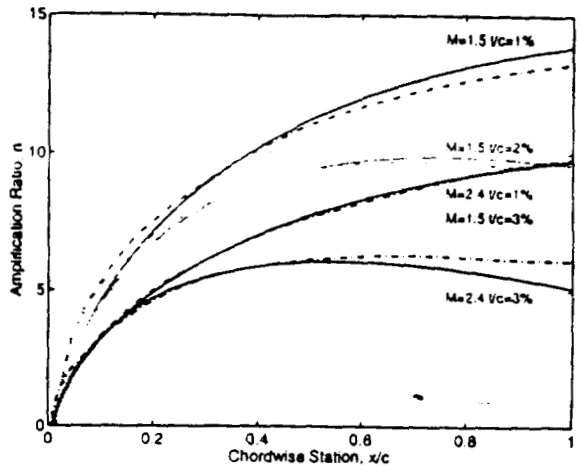

Figure 3.11: Comparison of streamwise amplification ratio fits and e^n calculations. (solid=fit, dashed=e^n). From [77]

In this research, the new definition is made:

$$\frac{dn}{dRe_\theta} = \frac{\left(\frac{dn}{dRe_\theta}\mid_{Drela} - K_2\right)}{K_1} \tag{3.7}$$

K_1 and K_2 are defined as:

$$K_1 = \left[\left(\frac{T_w}{T_e}\right)^{4.87} - 1\right]^{0.725} + 1 \tag{3.8}$$

$$K_2 = (H_{k_{LE}} - H_k)\left(1 - \frac{T_e}{T_w}\right)(0.22) \tag{3.9}$$

where the H_k is:

$$H_k = \frac{\delta^*}{\theta}\mid_{incompressible} \tag{3.10}$$

$\frac{dn}{dRe_\theta}\mid_{Drela}$ is the original equation from [22] depicting the change in n with momentum thickness Reynolds number. Drela defines it as:

$$\frac{dn}{dRe_\theta}\mid_{Drela} = 0.01\left[(2.4H - 3.7 + 2.5\tanh[1.5(H - 3.1)])^2 + 0.25\right]^{\frac{1}{2}}$$

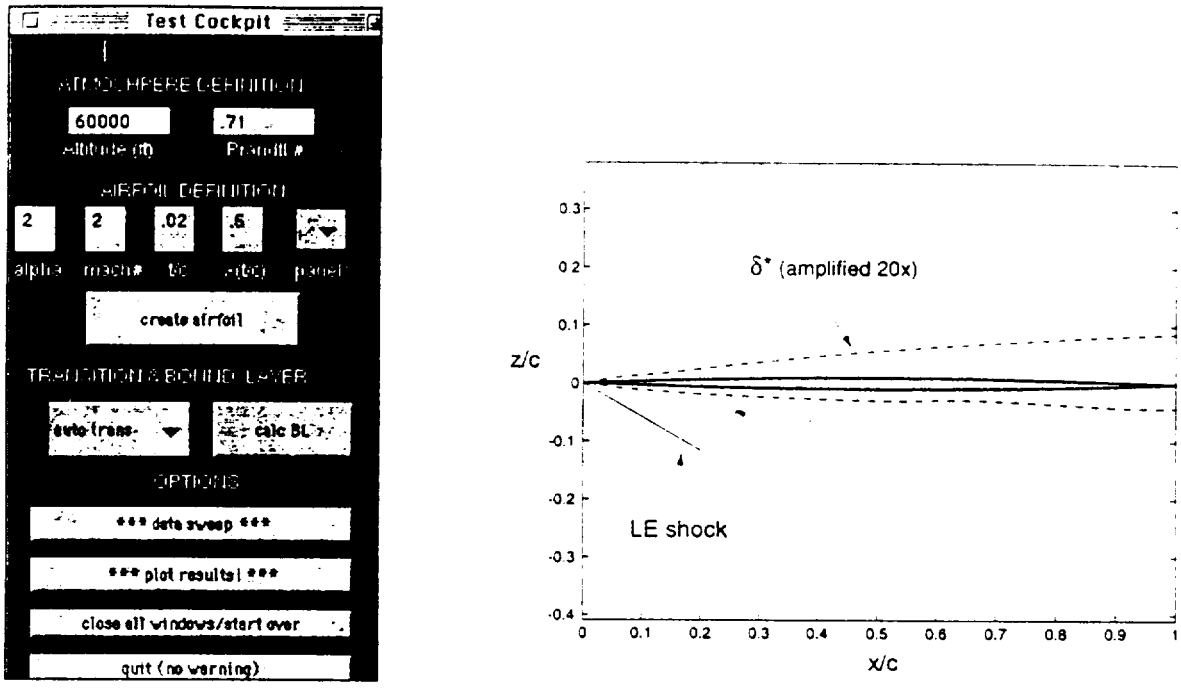

Figure 3.12: SABLA user interface and sample plot of an airfoil with shock and boundary layer exaggerated for viewing.

3.5.1.2 2-D Boundary Layer Studies

The Supersonic Airfoil Boundary Layer Analysis program (SABLA) was developed early in this research to provide a user-friendly, interactive way to study the effect of airfoil parameters on both boundary layer properties and inviscid lift and drag coefficients. In SABLA, the user is able to define the supersonic airfoil type, thickness, position of maximum thickness and flight condition. After a quick inviscid analysis using linear theory and method of characteristics, the user is prompted to select the method of boundary layer transition: free, fixed at a given percentage, or point-and-click selection of transition location. *SABLA* then uses the above analysis to compute the viscous drag coefficient, chordwise distribution of c_f, θ, δ^*, and n, and entropy rise through the leading edge shock. With a full graphics system, the capability to compute automated parametric studies with user defined ranges, and a built-in warning system to indicate when a shock is detached or when the assumption of small-disturbances is being violated, *SABLA* is a useful tool for preliminary supersonic airfoil performance and design trade-offs.

Using *SABLA*, Figures 3.13 through 3.18 were created to demonstrate the effect of α,

Mach number, and $\frac{t}{c}$ on chordwise distributions of displacement thickness (δ^*), momentum thickness (θ), and spatial amplification factor (n) for a 2-D biconvex airfoil. The horizontal line at $n = 9$ in Figures 3.14, 3.16, and 3.18 indicates transition.

The displacement thickness and momentum thickness above are defined as follows:

$$\delta^* = \int_0^\infty \left(1 - \frac{\rho u}{\rho_e u_e}\right) dy \tag{3.11}$$

$$\theta = \int_0^\infty \frac{\rho u}{\rho_e u_e} \left(1 - \frac{u}{u_e}\right) dy \tag{3.12}$$

where y is the distance from the surface, and the subscript e corresponds to the value at the edge of the boundary layer. δ^* is derived from conservation of mass in steady flow, and θ results from momentum conservation in the x, or streamwise, direction. Their ratio $H = \frac{\delta^*}{\theta} > 1$ is often used in boundary layer analysis.

It is apparent from Figures 3.14, 3.16, and 3.18, that stability is favorably affected by an increase in each of the parameters for thin biconvex airfoils in low supersonic Mach numbers. Local velocity on the airfoil and shape factor H are also proportional to Mach number, $\frac{t}{c}$, and α. Often, an increase in H leads to an increase in stability. Mach number has quite a strong effect due to the nature of δ^* and θ. The favorable effect of increasing $\frac{t}{c}$ is a consequence of the more favorable pressure gradient with increased thickness as well is the higher local velocity. It should be noted that the effect due to α in Figures 3.13 and 3.14 are shown for the upper surface. The lower surface is adversely affected by the decrease in local velocity with respect to the freestream and transition occurs earlier than that for aero incidence.

Friction coefficient is the dimensionless wall shear force:

$$C_f(x) = \frac{\tau_w(x)}{\frac{1}{2}\rho_e u_e^2} \tag{3.13}$$

For constant ρ_e, C_f is inversely proportional to u_e^2, and for the thin sections of interest, decreases with increasing H.

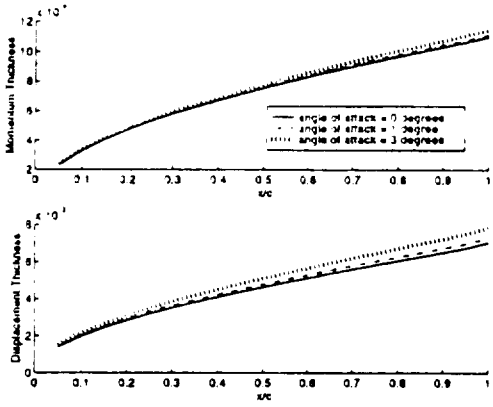

Figure 3.13: 2-D Boundary layer properties for varying α. Mach = 2.4, Re = 235×10^6-250×10^6

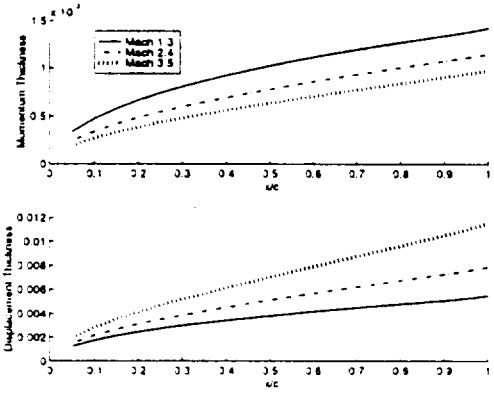

Figure 3.15: 2-D Boundary layer properties for varying Mach number. Re = 136×10^6, 250×10^6, 370×10^6

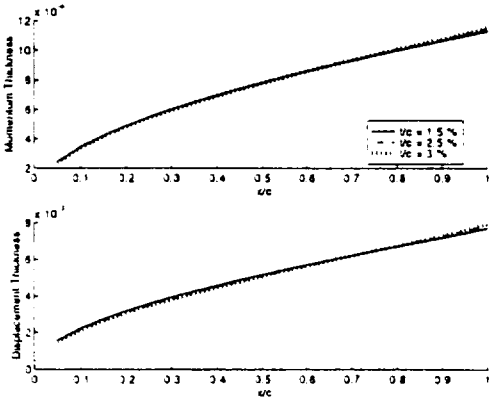

Figure 3.17: 2-D Boundary layer properties for varying t/c. Mach = 2.4, Re = 250×10^6-260×10^6

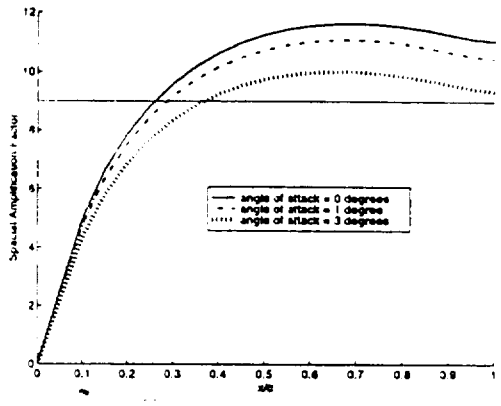

Figure 3.14: Streamwise amplification factor for varying α. Mach = 2.4, Re = 235×10^6-250×10^6

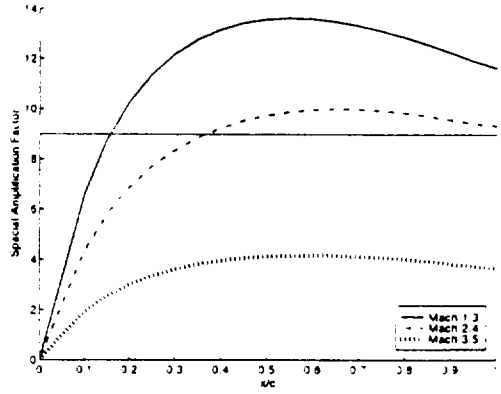

Figure 3.16: Streamwise amplification factor for varying Mach number. Re = 130×10^6, 250×10^6, 370×10^6

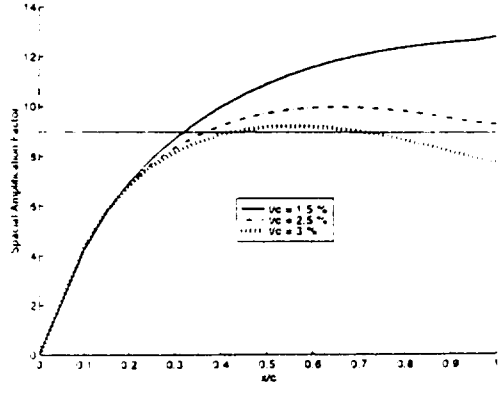

Figure 3.18: Streamwise amplification factor for varying t/c. Mach = 2.4, Re = 250×10^6-260×10^6

3.5.2 Crossflow Boundary Layer

This section describes an analytical crossflow analysis used to compute the crossflow Reynolds number and to help determine if a supersonic leading edge wing is crossflow critical.

The crossflow Reynolds number is defined as:

$$R_{cf} = \frac{\rho_e |w_{max}| \delta_{0.1}}{\mu_e} \tag{3.14}$$

ρ_e and μ_e in Equation 3.14 are the local density and viscosity, respectively, at the edge of the boundary layer. $\delta_{0.1}$ is the height above the surface at which the crossflow velocity reaches $1/10^{th}$ the maximum value, and w_{max} is the maximum local crossflow velocity.

The crossflow computations in this are performed via a method initially developed by Dr. Richard Tracy, and are a combination of empirical results and geometry assumptions that generates an estimation of crossflow Reynolds number based upon the wing geometry, flight condition, and empirical solutions.

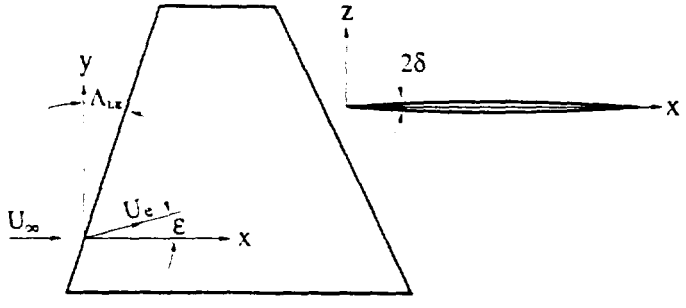

Figure 3.19: Left: Top view of swept wing leading edge. Right: Wing cross section

The resulting equations compare favorably with 3-D Navier-Stokes solutions and experimental data. [77] Once a critical crossflow Reynolds number is determined, the chordwise position at which the wing becomes crossflow-critical can be computed. Figure 3.19 shows the top view of a swept wing leading edge along with the cross-sectional view. The sweep and thickness affect the amount by which the local velocity direction is offset from the freestream.

For a slender wedge,

$$\epsilon = \delta \sin \Lambda \tag{3.15}$$

and for continuously varying δ and Λ:

$$\Delta\epsilon = \Delta\delta \sin\Lambda \tag{3.16}$$

Modeling the airfoil as a series of infinitesimal wedges the curvature of the inviscid streamline becomes:

$$\frac{d^2 y_s}{dx^2} \equiv y_s'' = \frac{d\epsilon}{dx} = \frac{d\delta}{dx}\sin\Lambda \tag{3.17}$$

As the surface curvature in the y plane is constant, the surface geometry is:

$$\frac{d\delta}{dx} \equiv \frac{d^2 z_w}{dx^2} \equiv z_w'' \tag{3.18}$$

defining the relationship between the inviscid streamline curvature and the surface geometry as $y_s'' = z_w'' \sin\Lambda$.

The 1954 Loos-Sowerby [44, 75, 86] crossflow solution is a 3-D analytic computation of the boundary layer on a plate with constant external streamline curvature similar to the Blasius boundary layer in a uniform external flow. [77] For constant inviscid streamline curvature y_s'', the crossflow profile is:

$$u_n(z) = F(z) U_e y_s'' x \tag{3.19}$$

where $F(z)$ is a tabulated function from Reference 75 and U_e is the inviscid external flow. Given the maximum value of $F(z)$ (for small disturbances so $U_e \approx U_\infty$) the maximum crossflow is:

$$u_{n_m} \approx -.32 U_\infty y_s'' x \tag{3.20}$$

At this point the solution process is divided into two procedures, which are later combined. The first solution assumes the crossflow is a function of the local inviscid streamline curvature only, while the second integrates the effect of upstream curvatures to compute the local crossflow. The local similarity solution does not incorporate any flow history, while

the integrated solution retains all flow history.

3.5.2.1 Local Similarity Solution

Assuming local similarity for non-constant streamline curvature y_s'', combining equations 3.17 and 3.20 yields the maximum crossflow value:

$$u_{n_m} \approx -.32 U_\infty x z_w'' \sin\Lambda \tag{3.21}$$

and from [86] taking the boundary layer height to be

$$y_{0.1} \approx 4.4\sqrt{\frac{\nu_\infty x}{U_{infty}}} \quad \text{where} \quad y_{0.1} = y(u_n = 0.1 u_{n_m}) \tag{3.22}$$

leads to a crossflow Reynolds number defined as:

$$R_{cf} \equiv \frac{|u_{n_m}|\, y_{0.1}}{\nu_{infty}} = \left(-0.32 U_\infty x z_w'' \sin\Lambda \frac{4.4}{\sqrt{\frac{U_\infty}{\nu_{infty} x}}} \frac{1}{\nu_{infty}} \right) \tag{3.23}$$

$$= -1.41 \sqrt{\frac{U_\infty x}{\nu_{infty}}} x z_w'' \sin\Lambda \tag{3.24}$$

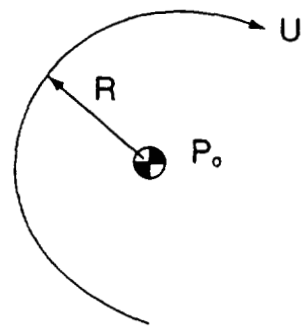

Figure 3.20: Radius of curvature of the boundary layer streamlines.

As the flow of concern here is supersonic, the compressibility effects must be taken into account. The density in the boundary layer with respect to that in the freestream flow is approximated as:

$$\frac{\rho_{bl}}{\rho_\infty} \approx \left(1 + \frac{\gamma - 1}{2} M_\infty^2\right)^{-1} \tag{3.25}$$

The radius of curvature of the boundary layer streamlines, as seen in Figure 3.20 for a given pressure gradient, scales with the density of the local flow, while the velocity scales with the inverse of the density.

$$\begin{aligned} P = \ & \tfrac{1}{2}\rho U^2 + P_o \\ & \text{therefore} \quad : R \propto \rho \\ & \text{and} \quad : u_n \propto \frac{1}{R} \propto \frac{1}{\rho} \propto \left(1 + \frac{\gamma - 1}{2} M^2\right) \end{aligned}$$

It is well known that the boundary layer thickness scales is inversely proportional to density, so the crossflow Reynolds number becomes:

$$R_{cf} \approx -1.41 x \sqrt{\frac{U_\infty x}{\nu}} \left(1 + \frac{\gamma - 1}{2} M^2\right)^2 z''_w \sin \Lambda \tag{3.26}$$

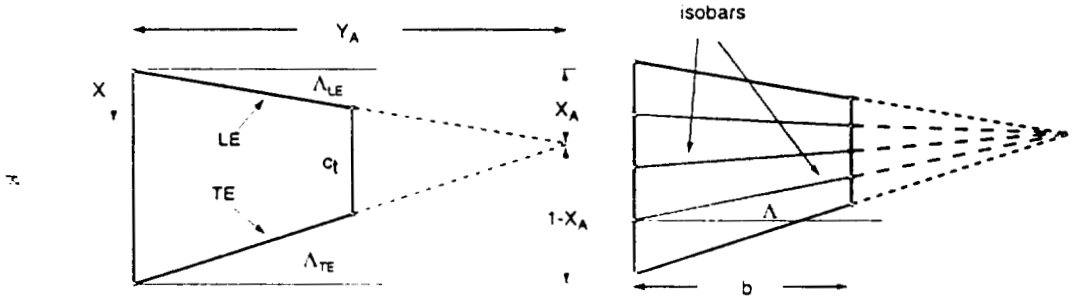

Figure 3.21: Planform view of wing geometry definitions for crossflow.

The local isobar sweep (Λ), and the surface geometry (z''_w) in Equation 3.26 must be defined. Figure 3.21 shows the planform view of a trapezoidal wing with sweep and conical taper. Assuming a constant spanwise distribution of airfoil shape, the isobars radiate from the tip along lines to a X value. The leading edge isobar has the sweep of the leading edge,

the trailing isobar has that of the trailing edge, and the intermediate isobars vary as:

$$\Lambda = \arctan\left(\frac{X_A - X}{Y_A}\right) \tag{3.27}$$

where X_A and Y_A are the coordinates of the wing vertex - the intersection of the extended leading and trailing edges as shown in Figure 3.21:

$$Y_A = \frac{c}{\tan(\Lambda_{LE}) + \tan(\Lambda_{TE})} \quad \text{and} \quad X_A = Y_A \tan(\Lambda_{LE})$$

c is wing chord at the spanwise station of interest.

The value of z''_w is a function of airfoil shape. In the case of the natural laminar flow wing, the airfoil is biconvex and parabolic defined by maximum thickness τ, and the chordwise position of maximum thickness x_τ. z_w and its derivatives then, are derived as:

$$z_w = \frac{1}{2} m \xi (1-\xi)^n$$

$$\text{where } \xi = \frac{x}{c}\ ,\ n = \frac{1}{x_\tau} - 1 \text{ and } m = \frac{\tau}{x_\tau (1-x_\tau)^n}$$

$$z''_w = \frac{\tau m}{2c}\left[-2n(1-\xi)^{n-1} + (n-1)\, n\xi (1-\xi)^{n-2}\right] \tag{3.28}$$

Given these definitions, the crossflow Reynolds number can be written as a function of airfoil thickness, wing sweep, taper, and Mach number. Armed with these definitions of z_w and Λ, and recognizing the convenience of including the chord Reynolds number into the cross flow equation, Equation 3.26 becomes:

$$R_{cf} \approx -1.41\sqrt{Re_c}\, c \xi^{\frac{3}{2}} z''_w \sin\Lambda \left(1 + \frac{\gamma - 1}{2} M^2\right)^2 \tag{3.29}$$

3.5.2.2 Integrated Crossflow Solution

An alternative to the local similarity solution is the integrated crossflow solution in which the flow is integrated in the chordwise direction. In this case, the derivation through Equation 3.20 is identical, however, Equation 3.21 becomes:

$$u_{n_m} \approx -.32U_\infty \int_x^0 z''_w \sin \Lambda dx \tag{3.30}$$

and instead of Equation 3.26 the crossflow Reynolds number develops as:

$$R_{cf} \approx \left[-1.41\sqrt{Re_x}\left(1+\frac{\gamma-1}{2}M^2\right)^2\right]\int_0^x z''_w \sin(\Lambda)\, dx \tag{3.31}$$

The definitions of Λ, Y_A, X_A, and z''_w are as determined in Equations 3.27 through 3.28. Incorporating the definition of linear taper and parabolic airfoil leads to:

$$R_{cf} \approx \left[-1.41\sqrt{Re_c}\xi^{\frac{1}{2}}\left(1+\frac{\gamma-1}{2}M^2\right)^2\frac{\tau m}{2c}\right]\times$$
$$\int_0^x \left[-2n(1-\xi)^{n-1}+(n-1)\,n\xi(1-\xi)^{n-2}\right]\sin\left[\arctan\left(\frac{X_A-X}{Y_A}\right)\right]dx \tag{3.32}$$

This equation can be analytically or numerically integrated at a given spanwise wing station from the leading edge to the trailing edge to determine the crossflow Reynolds number on a trapezoidal wing. As mentioned, the true crossflow Reynolds number is expected to lie in between the local similarity and integrated solutions. After correlating this approach with other methods [77] and with experiments, a 50 % -50 % weighted average of the similarity and crossflow procedures is used to predict crossflow Reynolds number.

Figure 3.22 shows a sample result of this crossflow analysis along with a three-dimensional Navier-Stokes solution on the same wing. This particular section of the supersonic leading-edge wing has a chordwise Reynolds number of 29 million and the Tracy crossflow method agrees quite well with 3-D Navier-Stokes up to approximately 85 percent chord. The "Agrawal" results were obtained from Reference 5.

3.5.3 Composite Amplification Factor

For the crossflow transition, the criterion due to Malik et al. [46] is used in which transition is predicted when the crossflow Reynolds number passes a Mach number dependent threshold.

$$Re_{c_{f_{crit}}} = K\left(1+\frac{\gamma-1}{2}M^2\right) \tag{3.33}$$

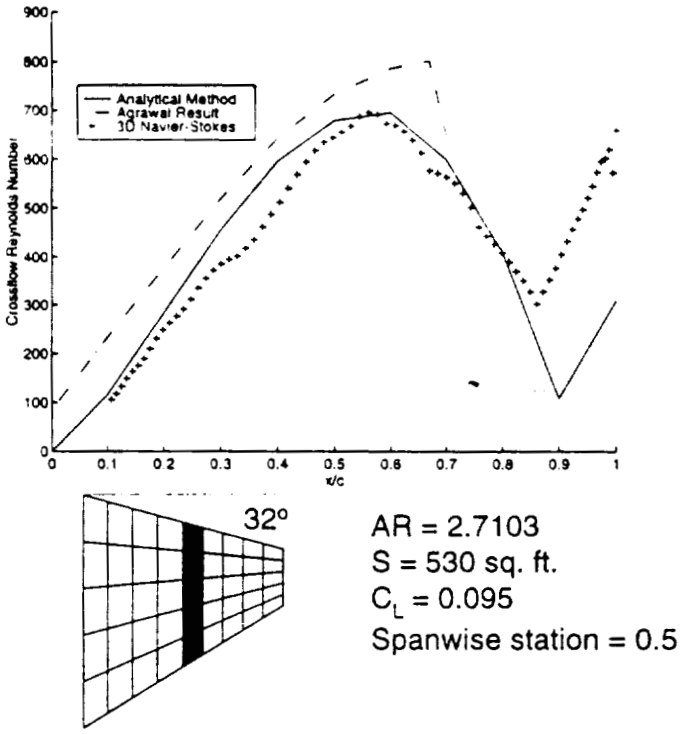

Figure 3.22: Crossflow Reynolds number on wing at Mach 2.0.

Any finite wing boundary layer may transition due to some combination of the streamwise and crossflow boundary layer instabilities. An infinite wing of no sweep would be subject only to streamwise instabilities. If this wing were swept slightly, some crossflow would be introduced, and at a 90 degree sweep angle, the entire flow would be "crossflow".

For a wing subject to some of each type of instability, it is possible the boundary layer will become unstable from a combination of the streamwise and crossflow effects, while if only one or the other were considered, no transition would be predicted. This combined 3-D effect is denoted the Composite Amplification Factor (CAF), N^*, and is a normalized combination of the two instabilities. This relationship is a subject of some discussion in the boundary layer research community. For the computations in this research, the relationship depicted by Equation 3.34 is used.

$$N^* = \left[\left(\frac{n}{n_{crit}} \right)^2 + \left(\frac{Re_{cf}}{Re_{cf_{crit}}} \right)^2 \right]^{\frac{1}{2}} \tag{3.34}$$

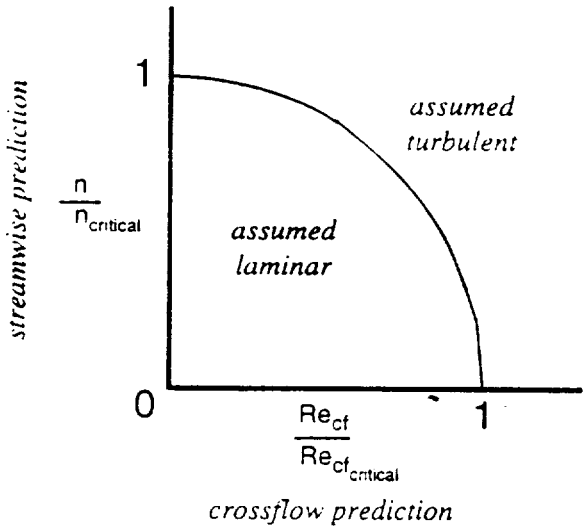

Figure 3.23: Composite amplification factor: Definition

If either the streamwise or crossflow instabilities are critical or if the *combination* is critical, N^* will be greater than one.

Figure 3.23 shows the assumed relationship between the streamwise and crossflow amplification ratios as a line plot.

Figure 3.24 shows the streamwise amplification ratio, crossflow Reynolds number, and composite amplification factor for a trapezoidal wing. In this result, white depicts regions of transitioned (turbulent) flow. For the conventional HSCT, the wing boundary layer will

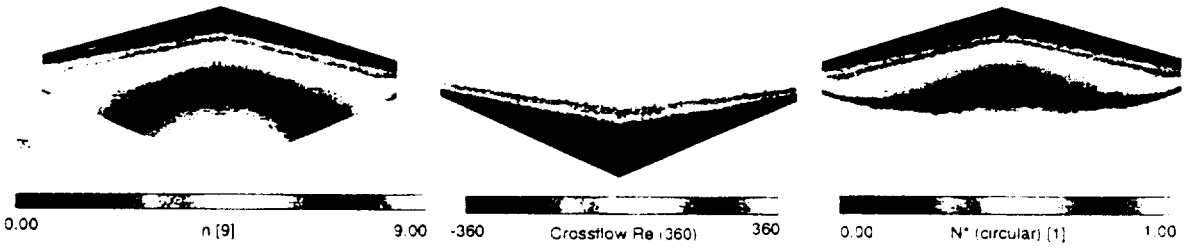

Figure 3.24: (Left to right) Streamwise amplification factor (n), crossflow Reynolds number and composite amplification ratio (N^*) on supersonic wing. White regions depict turbulent flow.

always transition very early inboard of the break, as almost the entire wing is dominated by the crossflow arising from the very high sweep of the wing (see Figure 1.7).

Figure 3.25 shows change of N^* on a NLF planform with sweep. Clearly, given an

otherwise fixed planform, there is an optimal sweep for maximizing laminar flow. When parameters such as thickness, wing area, span, and taper are altered, the optimal sweep value will also likely change. Thus optimization techniques will be required to maximize natural laminar flow.

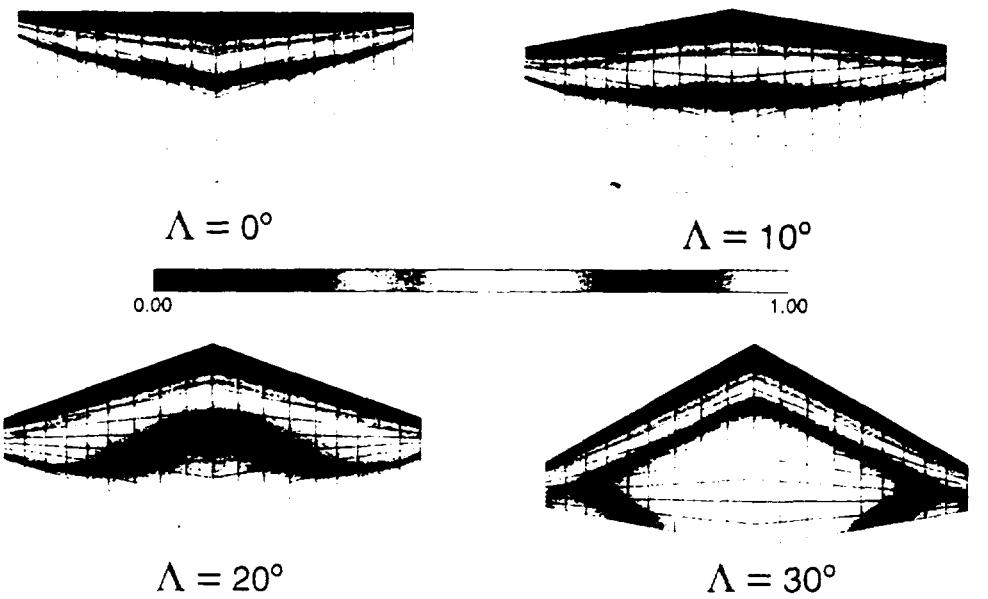

Figure 3.25: Composite amplification factor verses leading edge sweep for typical NLF planform.

3.6 Auxiliary Analysis Calculations

The basic structure of the aerodynamics analysis is shown in Figure 3.1. Once the pressures have been computed by A502, they are passed to the streamwise boundary layer analysis, which uses them to evaluate the skin friction drag and n for potential transition due to TSI. Next the crossflow analysis is performed, which is a function of flight condition and the wing geometry and which determines R_{cf}. N^*, the composite amplification factor, is then computed from n and R_{cf}, deciding the position of chordwise transition for each spanwise strip of the wing. After the streamwise boundary layer code is run again with the fixed transition location, the friction drag coefficient is computed and added to the other drag values. These empirically determined values are the parasite drag of the fuselage, propulsion system, and empennage, empennage wave drag, and a markup for interference

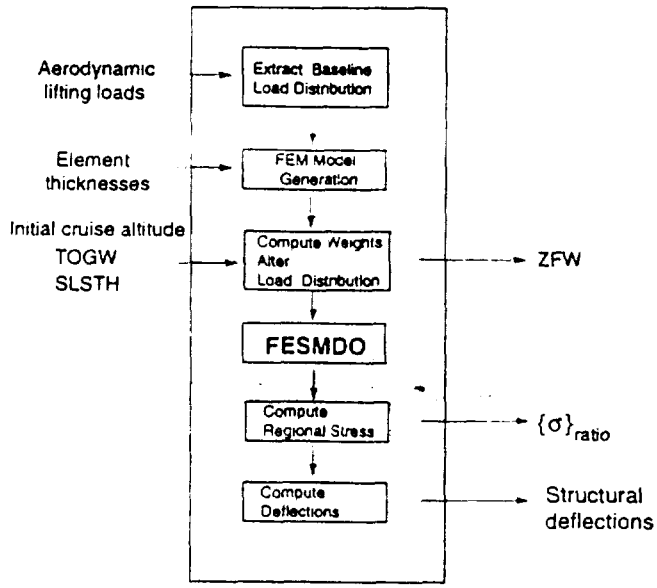

Figure 4.1: Organization of structures discipline analysis

and aircraft gross weight, and with additional parameters, the structural weight and inertial loads due to the wing, fuel, and engines are computed. The structural code then determines the finite-element model stresses and structural deflections. As an optimization subproblem, structures will generally need to find a set of element thicknesses which will provide a low computed aircraft zero-fuel weight without violating stress and deflection constraints. Within the collaborative optimization framework used in this research, the structures subproblem will attempt to match a target zero-fuel weight along with other target parameters.

4.3 The Finite-Element Model

A code developed for NASA Langley by Duc Nguyen, Finite Element Software for Multidisciplinary Design Optimization (FESMDO) [54], computes stresses and deflections given material properties, element thicknesses, and loads. The wing finite-element model is generated automatically from geometry design variables, element thicknesses, and fixed material properties.

The sample finite-element model in Figure 4.2 depicts a conventional high-speed transport wing. This 100 node sample is comprised of 172 bar elements and 324 triangular plate

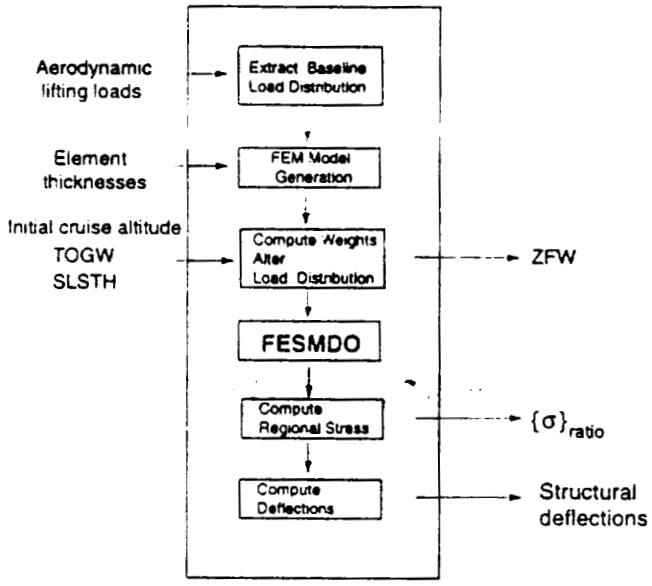

Figure 4.1: Organization of structures discipline analysis

and aircraft gross weight, and with additional parameters, the structural weight and inertial loads due to the wing, fuel, and engines are computed. The structural code then determines the finite-element model stresses and structural deflections. As an optimization subproblem, structures will generally need to find a set of element thicknesses which will provide a low computed aircraft zero-fuel weight without violating stress and deflection constraints. Within the collaborative optimization framework used in this research, the structures subproblem will attempt to match a target zero-fuel weight along with other target parameters.

4.3 The Finite-Element Model

A code developed for NASA Langley by Duc Nguyen, Finite Element Software for Multidisciplinary Design Optimization (FESMDO) [54], computes stresses and deflections given material properties, element thicknesses, and loads. The wing finite-element model is generated automatically from geometry design variables, element thicknesses, and fixed material properties.

The sample finite-element model in Figure 4.2 depicts a conventional high-speed transport wing. This 100 node sample is comprised of 172 bar elements and 324 triangular plate

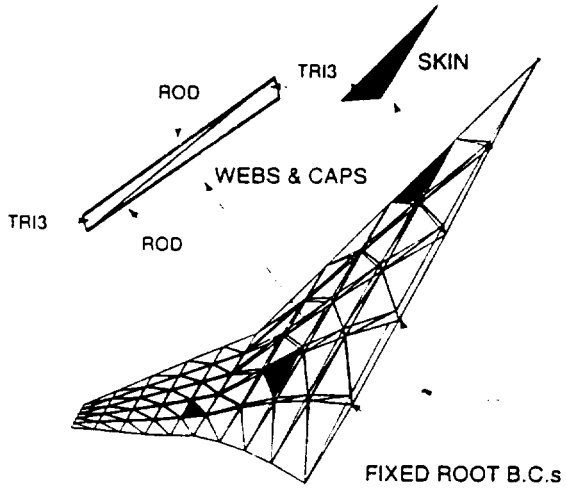

Figure 4.2: Sample finite-element model

elements (180 skin panels, 144 spar and rib web panels). In this view, the triangular panels

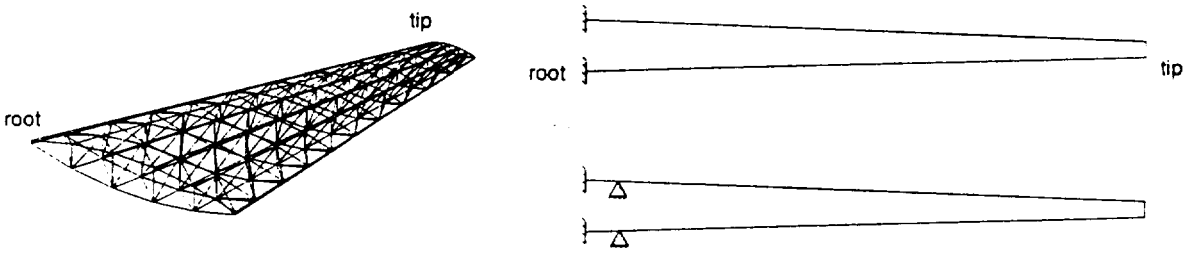

Figure 4.3: Wing FEM boundary conditions: Wing-only and simulated fuselage configurations. Constraints are applied to each node at the indicated spanwise stations.

making up the upper and lower skin and the spar and rib webs are visible. Additionally, the spar and rib caps are composed of 2-node rod elements which experience axial stress only. In the case where the entire wing is structurally modeled (as opposed to just the truncated wing-box), the leading and trailing edges have no rod elements, and the root has no rib webs. For the wing-only analysis, the boundary conditions fix all six degrees of freedom (DOF) of the upper and lower nodes of the wing root. The wing-body analysis is approached differently. Unlike the aerodynamics analysis, in which a fuselage is actually built into the surface geometry, the structures analysis accounts for the fuselage through boundary conditions only. This is due to the complexity of modeling a fuselage for finite-element analysis. When analyzing a wing-body case in the structures discipline, the wing

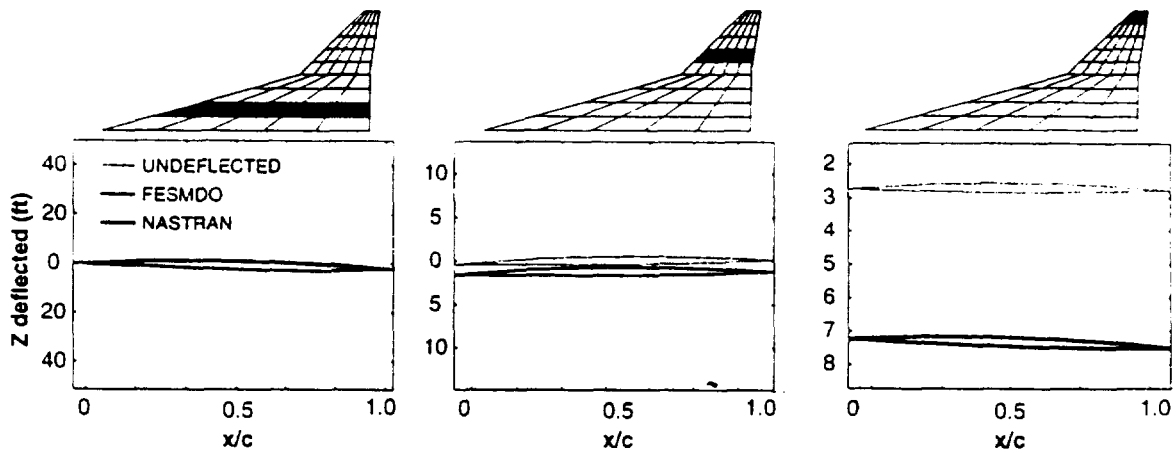

Figure 4.5: HSCT wing deflection comparison of NASTRAN and FESMDO

4.4 Validation of Finite-Element Code

FESMDO is the code used to compute deflections and stresses of the wing model. As this structural code had never before been used, NASTRAN [63], the industry-standard finite-element analysis code, was used to ensure an acceptable level of accuracy from the new analysis. Before incorporating FESMDO into the structures analysis, the code was compared with the Cray version of NASTRAN at NASA Ames. The author compared several models, including a flat, wide cantilever beam, a doubly tapered multi-element beam, and two supersonic transport wing models. FESMDO predicted virtually identical results in all cases for the nodal deflections, and plate stresses agreed quite well also. Results for the plate element stresses of the HSCT model for the two codes is shown in Figure 4.6, and associated deflections appear in Figure 4.5.

Each test model was run in NASTRAN using both 4-node quadrilateral (QUAD4) elements and 3-node triangular (TRI3) elements for skin, spar, and rib plates. The current version of FESMDO does not support 4-node quadrilateral plate elements, but allows 3-node triangular plate elements in addition to 2-node rod elements. Nodal displacements and truss element stresses compared favorably, however some discrepancies in the stresses of the spar webs, even between QUAD4 and TRI3 models evaluated in NASTRAN indicate problems predicting stresses with use of triangular plate elements. Upon release of a version of FESMDO which allows the use of quadrilateral elements, the finite-element model should be updated.

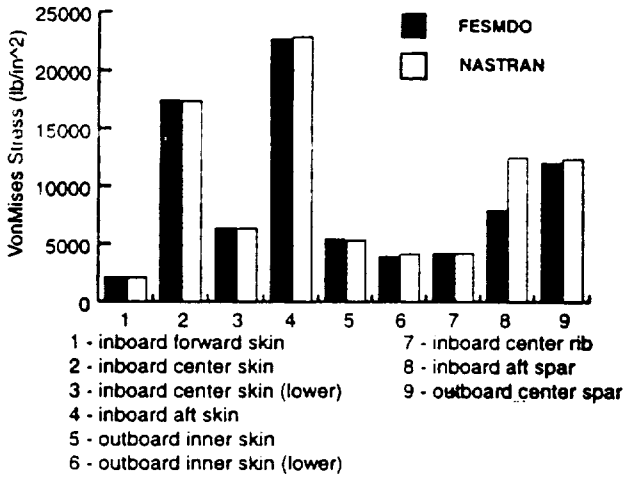

Figure 4.6: HSCT wing plate stress comparison of NASTRAN and FESMDO

4.5 The Iterative Fully-Stressed Solver

Given element materials, thicknesses, and nodal loads, FESMDO determines the stress of each element and displacement of associated nodes. To test the response of the structural model to these properties, an iterative fully-stressed solver (IFSS) was created. Given an finite-element model with a fixed load and an initial thickness distribution, this solver alters the element thicknesses after each evaluation of FESMDO such that upon convergence, each element is either minimum gauge or fully-stressed. The element thickness update is performed every iteration as follows:

$$t_i = t_{i-1}\frac{\sigma}{\sigma_{yield}} \tag{4.1}$$

The stress ratio $\frac{\sigma}{\sigma_{yield}}$ is the ratio of the Von Mises stress of each element to the maximum allowable stress of the material, where the Von Mises stress is defined as:

$$\sigma_{vonmises} = \sqrt{\sigma_x^2 + \sigma_y^2 - \sigma_x\sigma_y + 3\tau_{xy}} \tag{4.2}$$

Maximum allowable values of $\sigma_{vonmises}$ are listed in Table 4.1.

Figures 4.7 and 4.8 display fully-stressed results for both the conventional HSCT wing and the supersonic natural laminar flow wing with a fixed load. Figure 4.8 shows the stress ratio of selected spars. In general, rib elements are subject to little stress and are assigned

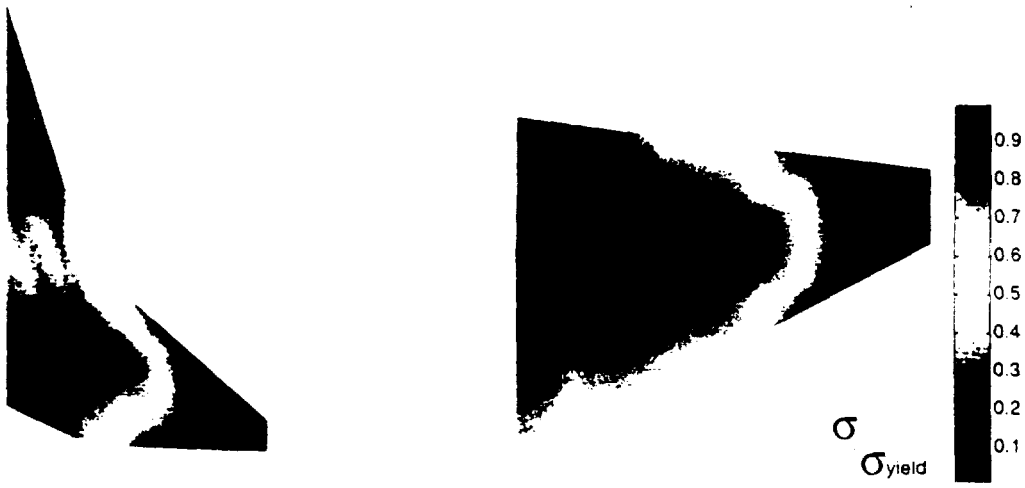

Figure 4.7: Fully-stressed solution, $\frac{\sigma}{\sigma_{yield}}$, for top skin. Elements are all either fully stressed or minimum gauge

minimum gauge thickness by the IFSS. In optimization, only if deflection constraints are placed upon the structure will the ribs require additional thickness, as they may be required to help stiffen the wing.

The strake of the conventional HSCT wing is not highly stressed, nor is the area near the tip. This is also the case of the spars of this wing in Figure 4.8. The inboard portion of the spars at the leading edge and near the mid-chord of the structural box, then, are not highly stressed either. The root of the spars is most highly stressed in the rear third of the wing. The highly-stressed portion of the NLF wing is a more uniform area near the root, and stresses decrease outboard.

4.6 Thickness Design Variable Selection and Grouping

It is necessary, in structural optimization, for the optimizer to size finite-element model thicknesses in order to meet deflection and stress constraints under load. These thicknesses also set the weight of the model. In order to design each element in an optimization individually, the thickness of each of the hundreds or thousands of elements in a finite-element model would become local design variables. This formulation would prohibitively increase the size of the optimization problem and consequently the time required for optimization. For this reason, it is common in multidisciplinary optimization to group these element

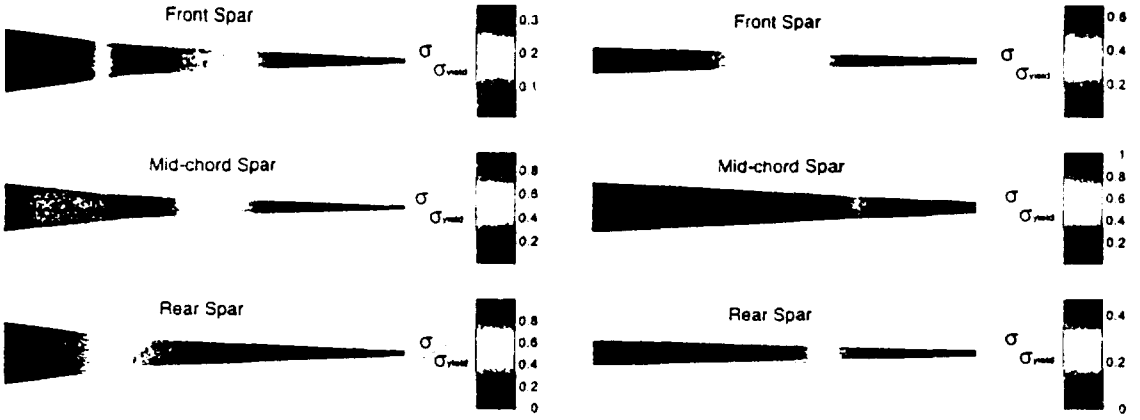

Figure 4.8: Fully-stressed solution, $\frac{\sigma}{\sigma_{yield}}$ result for selected spars. Elements are all either fully stressed or minimum gauge. LEFT: Conventional HSCT wing. RIGHT: Supersonic NLF wing.

thicknesses in a reasonable manner. For example, grouping together areas of low loading and high loading, or areas which need thick elements with areas which only need minimum gauge, should be avoided. To assist in the element grouping, the results of an iterative fully-stressed solver (see Section 4.5) might give insight into reasonable element groupings. A list of the options examined for this research follows.

FEM Thickness Design Variable Options for Optimization		
	Option	*Potential Shortcoming*
(1)	Each element assigned a *DV*	Extreme computational expense
(2)	Fully stress the structure each iteration	Convergence problems, fully stressed design not ideal for some aeroelastic solutions
(3)	FS initially, subsequently scale FS structure thicknesses	If nature of loading changes, distribution will be incorrect
(4)	Group thicknesses by regions of similar stress using IFSS result	If stresses are also grouped, gradient problems confuse the optimizer
(5)	Spanwise distribution of thickness	Neglects chordwise changes
(6)	Spanwise distribution of thickness with a linear chordwise distribution parameter	Most accurate for linear chordwise stress distribution

In each of the six options, the manner in which the element stress constraints are handled affect the solution. Convergence problems occurred in initial attempts at large-scale optimization due to grouping element stresses for use in optimization. [71] In those cases, design variable option 4 was used. Elements are grouped into regions of properties and each region is assigned a design variable in the structural optimization. The stresses can then be handled in two ways. For example, within a given region, the highest element stress can be attributed to the entire element set, and subsequently, the optimizer chosen thickness could be applied to the entire region. Obviously, though reducing the size of the design problem, some accuracy would be lost and problems such as oversizing some elements may occur. Options 5 and 6 are a better approaches, and are used for the optimizations of the conventional HSCT aircraft and the supersonic NLF aircraft, respectively. This involves grouping the element thicknesses for design variable reduction, while allowing the optimizer to analyze the stress of each element individually.

As stated, the initial structural optimization test runs for this research, results of which can be seen in [71], used results of the iterative fully-stressed solver described in Section 4.5 to assist in finite-element thickness grouping. This initial set follows:

Initial finite-element grouping			
Wing section	*Material*	*Wing section*	*Material*
Upper inboard skin	Ti	Inner center spar webs	Al
Lower inboard skin	Ti	Outer spar webs	Al
Upper outboard skin	Ti	Rib webs	Al
Lower outboard skin	Ti	Spar caps	Al

Element groups are split according to wing location (upper, lower, inboard of wing span break, outboard of span break) and element type (skin, web, cap). Each of the group thicknesses is a design variable in the structural optimization and the corresponding stress for each group is involved in a constraint.

Structural variable and constraint management for the aircraft designed in this dissertation has been updated. In order to better reflect actual fabrication practices, the thickness distribution was changed to enforce linear thickness distribution from root to break and from break to tip on the upper and lower skin and on the spars. The ribs remained as one group, and each element stress is handled individually by the optimizer:

Updated finite-element grouping	
Wing section	*Material*
Skin Root	Ti
Skin Break	Ti
Skin Tip	Ti
Spar Web Root	Al
Spar Web Break	Al
Spar Web Tip	Al
Rib Webs	Al
Spar caps	Al
Rib caps	Al

The aerodynamics analysis normally desires some washout in the wing for optimum performance. For the conventional HSCT wing (Figure 1.15), the loading and wing configuration combine to naturally induce structural deflections that lead to washout.

For the low-sweep natural laminar flow wing (Figure 1.16), the situation is quite different. The aerodynamics analysis will still benefit from washout, however the nominal structural deflections lead to washin. The original skin, spar, and rib thickness design variable combination, as developed in the structural analysis, does not allow structures to use inertial loading to obtain washout. It is only possible to design a stiff wing with no twist at all. In response, two local design variables were added to the structures optimization problem. These additional degrees of freedom allow the optimizer to move the elastic axis by adding material to the spars in the chordwise direction. The design variables are a thickness mark-up at the leading and trailing edges, and spar thickness varies linearly between them.

4.7 Loads Applied to Finite-Element Model

The loads on this structure are applied as forces to the upper and lower nodes of the finite-element model. The aerodynamics loads, calculated from forces at the centroid of each aerodynamic panel, is interpolated to the finite-element model nodal points. These aerodynamic loads are then split evenly between the upper and lower surfaces, applied as suction to the upper surface nodes and pressure on the lower. Additional loads applied to

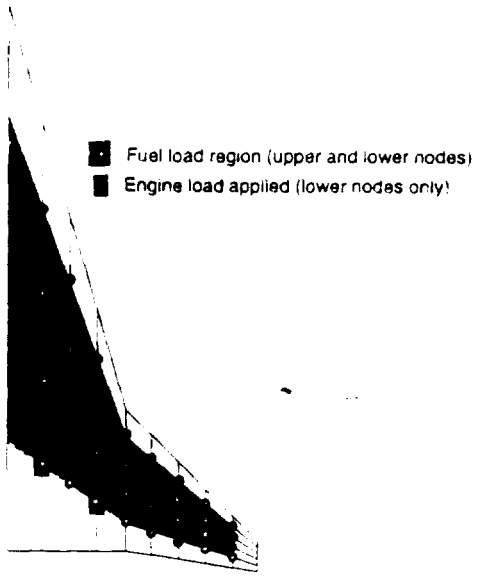

Figure 4.9: Applied inertial loads due to fuel, engines and nacelles.

the structure are the distributed inertial loading due to fuel volume and wing structural weight, and the concentrated point masses of the engines and nacelles, seen in Figure 4.9. Forces from landing gear, high-lift devices, thermal effects, and additional wing systems are omitted.

The fuel volume distribution within a wing is a function of fuel tank location. Though fuel tank design is not addressed in this research, the effect of three methods of distributing fuel load to the nodes of the finite-element model was explored so a reasonable method could be selected. A crude assumption for this exploratory analysis is that the wing volume is otherwise empty, and baseline structural optimization was performed using each approach as show in Figure 4.10. As defined in Equation 2.3, the structural optimization goal is to minimize the discrepancy between the inputs and outputs of the structural analysis and a set of prescribed targets, with respect to finite-element thicknesses and subject to stress constraints.

In method A, the wing is assumed to have a number of spanwise "tanks", and the filling is performed from root to tip. Once the entire fuel volume has been stored, any remaining wing volume is empty. The less realistic Method C is similar, but the filling starts at the tip and moves to the root. In the example, Method A leaves the outboard 4 (of 9) tanks empty, with tank 6 partially full. Method C fills all but tank 1, which is closest to the

Value	*Method A*	*Method B*	*Method C*
$J^*_{structures}$	0.707	0.707	.707
time to optimize (min)	171	171	104
fuel vol (ft^3)	8270	8272	8271
fuel volume/wing volume	0.830	0.830	0.830
tip deflection (in)	88	117	117
FEM weight (lb)	47355	26824	25560
wing weight (lb)	53112	53110	53112
stress ratios (skin,skin,spar,rib)	.67,.66,.47,.12	.97,.97,.62,.16	.98,.97,.64,.14
skin thick (in) (root/tip)	.207/.048	.096/.048	.092/.048
spar thick (in) (root/tip)	.184/.062	.145/.050	.106/.072

Table 4.2: Structures optimized results testing fuel distribution methods. Structural box is 85% of the wing chord. If the fuel volume is greater than or equal to the wing volume, the methods would produce identical results.

wing root. Method B essentially fills each tank by the ratio of fuel volume to wing volume, approximately 85 percent for this example. The three analyses are otherwise identical. Table 4.2 compares optimized results using each method. Table 4.3 compares results of the same three methods and their effect on an iterative fully-stressed solver result. The optimization case differs from the fully-stressed case because the optimizer is trying to match a specified wing deflection distribution and the fully-stressed solver has no such constraint.

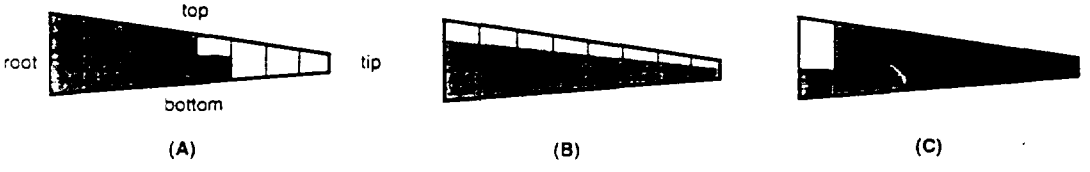

Figure 4.10: Fuel distribution methods

Methods B and C yield similar results in optimization. Specified at the root and tip and interpolated linearly in between, the wing skin in both cases goes to minimum gauge at the tip, and is highly stressed at the maximum. Method B is used for the optimization studies in Chapter 7.

Value	*Method A*	*Method B*	*Method C*
# of iterations	111	94	78
fuel vol (ft^3)	8691	8691	8691
fuel volume/wing volume	0.741	0.741	0.741
tip twist (deg)	-8.5	-7.31	-6.57
tip deflection (in)	191.4	181.3	174.3
FEM weight (lb)	28 113	25 108	23 812
wing weight (lb)	52 805	52 805	52 805

Table 4.3: Structures discipline fully-stressed results testing fuel distribution methods. Structural box is 85% of the wing chord.

Aircraft Auxiliary Weights (in lb)			
Component	*Equation*	*Conventional*	*NLF*
Passengers	165 $n_{passengers}$	41 250	41 250
Baggage	40 $n_{passengers}$	10 000	10 000
APU	7 n_{seats}	1750	1750
Electrical and electronics	1500 + 13 n_{seats}	4750	4750
HVAC	15 $n_{passengers}$	3650	3750
Operational items	40 $n_{passengers}$	10 000	10 000
Attendants	150 n_{attend}	750	750
Crew	205 n_{crew}	410	410
Hydraulics/pneumatics	0.65 S_{wing}	5379	4989
Landing gear	0.04 TOGW	29 800	21 400
Fuselage	$1.35(d_{fuse} * l_{fuse})^{1.28}$	48 128	48 128
Surface controls	3.5 $(S_{horiz} + S_{vert})$	2926	2713

Table 4.4: Aircraft auxiliary weights (in *lbs*)

4.8 Structural Weight Calculations

Multidisciplinary optimization of aircraft requires procedures to determine the placement of internal load bearing material and structure of an aerospace vehicle. This is a difficult synthesis problem. As a result, in the conceptual design phase empirical evidence and statistical correlation assist in the structural and non-structural weight definition [40]. Component weights for the baseline aircraft in this research are: shown in Table 4.8.

The weight of the wing, fuel, and propulsion system are based upon the finite-element model sizing, the fuel volume, and the engine size, respectively.

Wing weight calculation is initiated with the weight summation of each element of the model from the material properties and element volume. The actual weight of the wing is

greater than the structural weight of the structural model due to the necessary addition of fastening elements, manufacturing constraints such as minimum gauge of the load carrying elements, weight of the non-structural mass elements and local strength requirements that will not be captured during early design. According to Kamorov [40] a *construction factor*, Φ, can be used in weight estimation research, which has a history dating back to Soviet railroad construction. The construction factor depended on the aircraft type, component, and manufacturing methods, but was generally defined as $\Phi = \frac{W_{real}}{\rho V_{theor}}$. The denominator is the product of material density and volume of the theoretically optimized structure. For the current wing structural analysis, the weight markup is similarly based upon empirical data. Studies of detailed HSCT structural analyses were made to determine a representative differential between structural model weight and true wing weight. Care was taken to ascertain what was and was not included in the wing weight, as items like APU, wiring, main gear, and other items located in the region of the wing are not handled identically from study to study. A compilation of this empirical data led to a wing weight markup of 1.5 for the 250 passenger aircraft optimized in this dissertation.

The horizontal tail, vertical tail, and rudder weights are based empirically on aircraft component sizes and weights such as tail area, thickness, taper ratio, chord and sweep, and aircraft TOGW and wing area [41]. Similarly, the propulsion system weight is a function of the number of engines, the sea-level, static thrust, and the cruise velocity.

Chapter 5

Mission Analysis

5.1 Introduction

The mission analysis within this multidisciplinary optimization concept computes aircraft range and design constraints such as available power and distances for take-off and landing. There exists a range of options for mission and trajectory analysis, from fully-integrated optimization codes to simple estimations. An initial mission study was performed with the Program for Aircraft Synthesis Studies (PASS) [41], which utilizes simple analyses and optimizes given geometry and performance design variables, and performance constraints. PASS is a stand-alone integrated program incorporating aerodynamics, structural, stability, and performance modules based largely on the equations of Reference 68 and statistical correlation with known performance. The mission performance analysis in this research includes computation methods from PASS, and additional statistical data.

The focus of this research is the large-scale implementation of an optimization architecture and of the aerodynamic and structural analysis of a new HSCT concept, thus the mission and performance discipline is the least complex. The discipline provides an acceptable approximation of the aircraft response. One benefit of collaborative optimization is the ability for designers to perform relatively straightforward analysis substitutions without upsetting the remaining disciplines. Therefore a more advanced mission analysis, such as FLOPS [48], could replace the current computations with little difficulty.

5.2 The Mission Design Problem

Given lift-to-drag ratio, take-off gross weight, zero-fuel weight, initial cruise altitude, sea level static thrust, and all free wing planform and fuselage design variables, the mission analysis computes the aircraft range, drag-to-thrust ratio for climb, available fuel volume and the field lengths. Figure 5.1 depicts the flow of the mission discipline, showing inputs and computed values. The details of selected computations are included in this chapter.

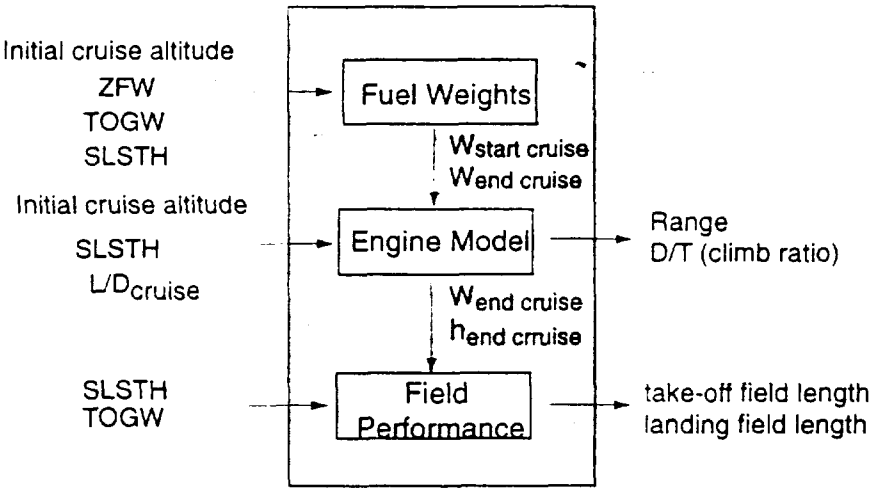

Figure 5.1: Organization of mission discipline analysis

5.3 Propulsion System Modeling

Supersonically, the most efficient engine moves small volumes of air at high velocities (turbojets/military fighters) while at lower speeds, the opposite is preferred (turbofans/subsonic cruisers). An engine optimized for supersonic cruise performance may be inadequate and noisy at the low speeds of takeoff and landing. An engine optimized for takeoff and landing would create higher drag at cruise, and have reduced fuel efficiency.

The ideal configuration of a modern supersonic transport would include two sets of engines. Efficient, quiet turbofans would be used at low speeds, and powerful turbojets at cruise. The compromise is a variable cycle turbofan engine, or VCE, which strives to meet the ideal with one engine. The turbofan engine is comprised of fan, compressor, combustor, high pressure turbine, and low pressure turbine sections. After compression, the bypass air flows into the fan duct and the rest into more compression and the combustor. The

expected HSCT combustor would likely be multi-stage, for instance burning a rich mixture in the first stage, and a leaner one in another stage [20]. The underwing position of the supersonic transport engine means the intake velocity is slightly lower than that of the freestream, reducing problems and increasing potential for pressure recovery. This location is beneficial for engine maintenance, and removal, and potential of intake shocks to assist in wing lift.

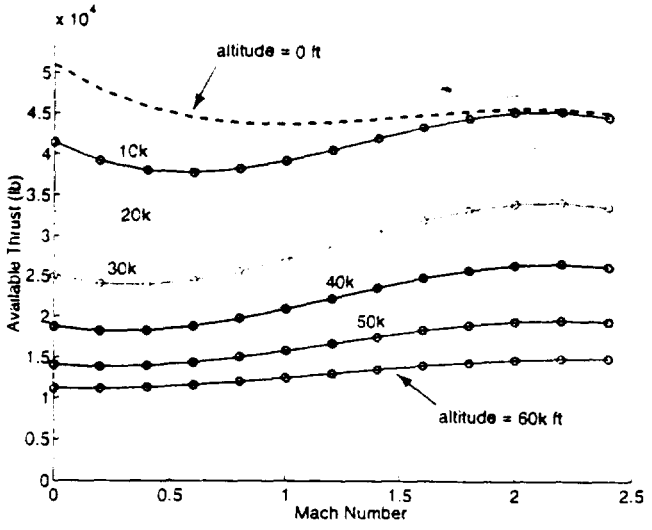

Figure 5.2: Original engine available thrust vs Mach number and altitude (SLSTH = 60 000lb)

The VCE in this design problem is a low bypass ratio engine with a design Mach number of 2.4. One focus of this engine is a low lapse rate with altitude. Figure 5.2 shows the variance of available thrust as a function of Mach number and altitude for an engine used in the initial design attempt of the conventional HSCT, that produces insufficient thrust at high speeds and altitudes. The search for a better, more representative engine ended at NASA's High Speed Research program, from which expected engine performance data was obtained. Given an SLSTH of 50 000 pounds, the variation of available thrust of the new engine versus Mach number and altitude appears in Figure 5.3.

One of the useful parameters describing engine performance is specific fuel consumption, or sfc. The sfc measures how efficiently an engine uses supplied fuel to produce work: the fuel flow rate per unit power output [36]. For turbojets and fans, the sfc is usually expressed as the thrust specific fuel consumption or $tsfc$. It is defined as the weight of the fuel burned

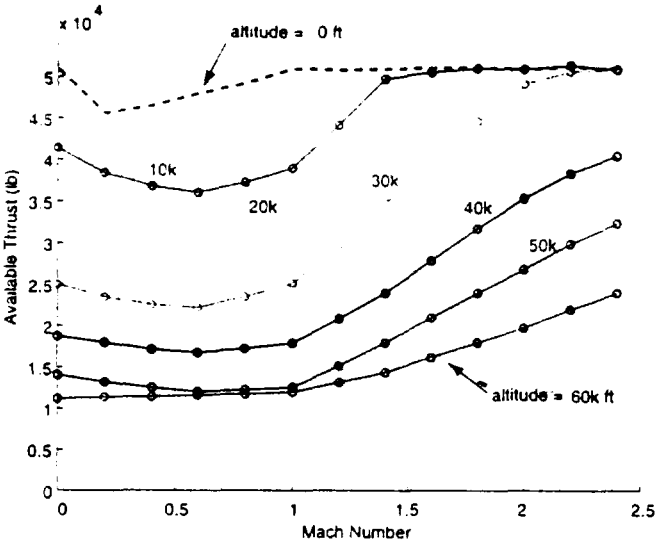

Figure 5.3: Updated Engine available thrust vs M_{cr} and h (SLSTH = 60 000lb)

per unit time, per unit thrust with units of lbs of fuel per hour per lb of thrust or $\frac{(lb_{fuel}/hr)}{lb_{thrust}}$ or 1/hr [42]. Obviously, low values of $tsfc$ are desired. The engine $tsfc$ used in this analysis in the cruise condition is approximately $1.25\frac{(lb_{fuel}/hr)}{lb_{thrust}}$.

True engine performance is affected by many additional factors such as compressor air bleed for air conditioning, power loss due to hydraulics and inlet and exhaust duct losses. A 2.0-3.0 % markup in $tsfc$ reasonably estimates these losses [42]. With $tsfc$ known, the overall engine efficiency can be computed. This efficiency, η_{net}, is the ratio of useful work performed by the system to the heat energy available from perfect fuel combustion. As a dimensionless parameter, η_{net} can have more fundamental value than the dimensional $tsfc$. From [68]:

$$\eta_{net} = \frac{TV}{T\ tsfc\ h_f} = \frac{V}{sfc\ h_f} \tag{5.1}$$

where h_f is the heat energy available per unit weight of fuel, with a value of about 18 400 $\frac{BTU}{lb}$, or $14.5 \times 10^6 \frac{ft-lb}{lb}$ for JP-4. The variation of η_{net} with Mach number is shown in Figure 5.4 (from Reference 42) for many jet engines to transonic Mach numbers. A dashed line represents the predicted efficiency of the engine in this analysis. With a design Mach number of 2.4, the efficiency is lower than that of the other engines at subsonic and transonic speeds, but increases linearly to a value of approximately 0.48 at the cruise Mach

number. The linear increase of efficiency to the design Mach number is a fair approximation to empirical data. In this analysis, at cruise altitudes and at the cruise Mach number of 2.4, $\eta_{net} \approx 0.48$.

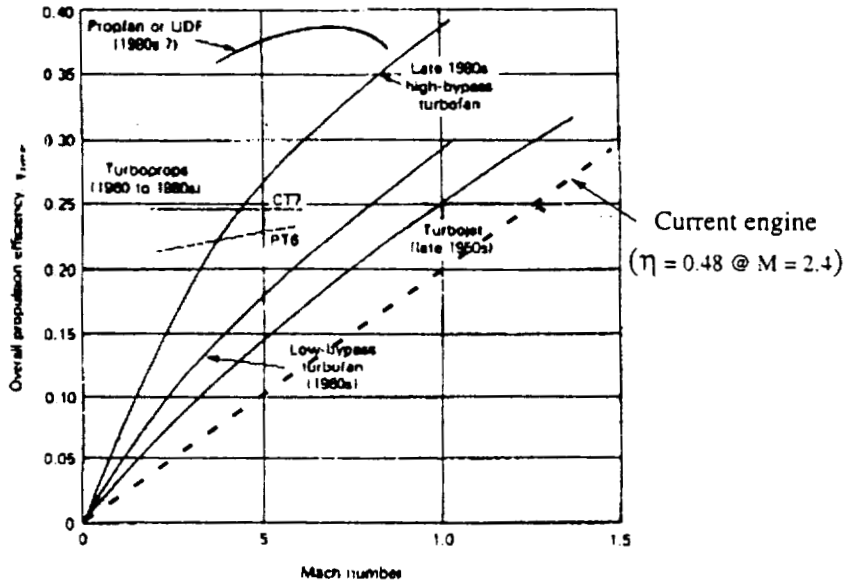

Figure 5.4: Engine efficiency (η_{net}) versus Mach number for selected engine types. [68]

5.4 Flight Profile

The aircraft designs in this research are subject to a minimum range constraint of 5000 nautical miles. [1] Calculation of range is a function of the flight profile definition. This is a line plot of altitude versus distance, with segmental descriptions of segments such as takeoff, climb, and cruise. The block mission and the reserve portion are plotted independently.

A sample flight profile, not to scale, is shown in Figure 5.5, and is representative of a basic transport aircraft. Some of the reserve segments are based upon those in References [42] and [21]. To compute range, the the fuel attributed to each portion of the flight profile must be determined. The following list describes the fuel weight calculation for each flight segment.

[1] A nautical mile, equivalent to 1.15 statute miles, is a unit of length equal to the distance along 1 minute of longitude at Earth's equator.

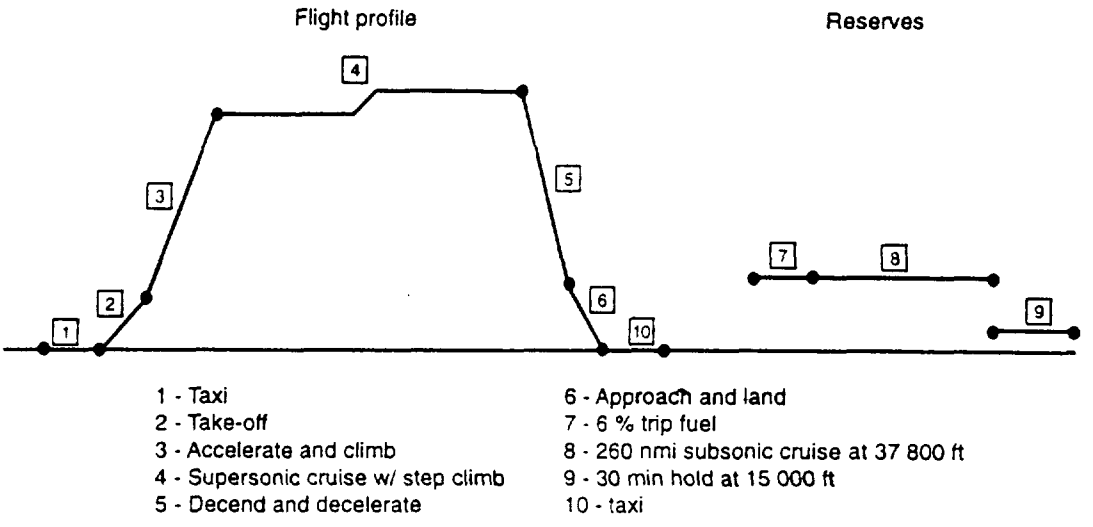

Figure 5.5: Sample flight profile (altitude versus distance) and reserve segment.

- (1 and 2) Taxi and Takeoff: The required fuel for maneuvering for a high-bypass-ratio turbofan is estimated, from empirical data, as 0.7% of the $TOGW$ [68]. This preliminary segment is allotted half of the fuel, or 0.35% $TOGW$.

- (3) Climb: The actual requirements for climb are a complicated combination of subsonic and supersonic segments, and are described in FAR 25.115. A simple approximate method for preliminary design of turbofan powered aircraft is adopted from [68].

  An estimation, developed from a statistical fit of many aircraft, is made of the additional fuel required to climb to cruise altitude in terms of a percentage of the $TOGW$. An altitude factor of:

$$CF = \frac{h_{cruise}}{10000} 0.43$$

  is the percentage of $TOGW$ determining required fuel weight for climb. This fuel weight penalty is approximately 2.6 % of the $TOGW$ at the typical cruise altitudes for supersonic transports. This is *not* the fuel used in climb, but the increase in fuel required to climb compared to the fuel required to cruise the distance covered in climb. The idea behind this approximation is that energy is required even to lift the weight to cruise altitude. There are additional losses, such as penalties from flying below optimum cruise altitude during climb and the effect of this lower altitude on

$tsfc$ [68]. This approach assumes that the engine is sized by the top-of-climb thrust requirement and not by the transonic climb. Though in many cases the assumption is not ideal, the approximation makes this analysis simpler.

Though the computation of fuel for climb was developed from the data on a number of aircraft, there are shortcomings with respect to the HSCT. The difficult part of the climb for a supersonic transport is the transonic/low-supersonic acceleration portion, when the aircraft is at about 30 000 feet of altitude and a Mach number of around 1.0. In this research, true climb and descent are not detailed, due to their complexity and the lack of focus in this research on detailed mission development. Again, this is an advantage of collaborative optimization (CO). Replacement of this simplified computation can be easily performed without disruption of the other disciplines, such as aerodynamics and structures.

- (4) Cruise: During the cruise segment, as the aircraft weight decreases, the aircraft must climb in order to maintain constant lift coefficient. An assumption of constant cruise C_L, along with the constant cruise Mach number, allows for the computation of (higher) final cruise altitude given the initial cruise altitude as an input. This altitude increase resulting from fuel burn during cruise leads to supersonic climb during cruise. In practice, there may be more of a step climb at some time in the cruise portion of the flight profile, as shown in segment 4 of Figure 5.5.

  The fuel allotted for cruise is the total fuel load excepting reserves, ground maneuvering, take-off, landing, and climb.

- (5 and 6) Descent and landing: This portion is handled as (1 and 2).

- (7) 6 percent trip fuel reserve: This amounts to 6 percent of all fuel excepting that used in ground maneuvering

- (8) subsonic cruise reserve: This is a 260 n.mi. trip at an altitude of 37 800 feet. Given this distance, a Mach number and an altitude, the time of this segment is computed. Given also the engine thrust- specific-fuel-consumption ($tsfc$), the fuel weight of this section can be computed.

- (9) 30 minute hold reserve: This segment, at an altitude of 15 000 feet, is computed in the same way as the the fuel weight in (8).

- (10) Taxi is grouped with (5 and 6)

Once the fuel weight due to each segment is computed, the weights at the start and end of cruise are made available, and the range can be calculated as a result. Each of the preceding calculations is an approximation based upon statistical data. The estimations in take-off and climb segments are fairly simple for an actual HSCT analysis, however the fact that these aircraft fly for long ranges, for which the cruise portion is the dominant portion of the total trip, make this approach acceptable. It is clear though, that a more enhanced analysis in this area would be beneficial. A flight profile representing steps 1 through 9 above is plotted in Figure 5.6 and depicts the analysis simplifications.

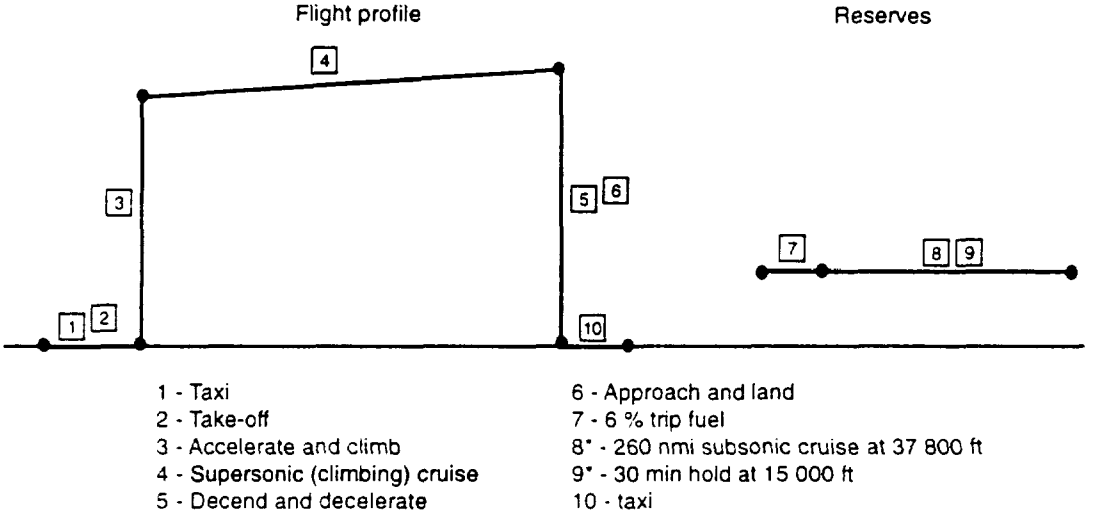

Figure 5.6: Simplified flight profile: Note the step climb in cruise is eliminated and the reserve fuel computation (8 and 9) is simplified

5.5 Mission Analysis Computations

5.5.1 Aircraft Range

The range computation in the mission analysis is based upon the Breguet range equation:

$$Range = \frac{V}{tsfc}\frac{L}{D}\ln\frac{W_{initial}}{W_{final}} \tag{5.2}$$

where V is the velocity, and $tsfc$ is the thrust-specific fuel consumption. To simplify the multidisciplinary optimization problems in this research, cruise L/D, an input to the mission optimization subproblem, is assumed constant. As previously shown, $tsfc$ is unchanged throughout the cruise segment, as is V (then entire cruise segment is above 36 000 ft). So, given $TOGW$, ZFW, and fuel weights for each flight segment, the aircraft range can be computed.

5.5.2 Required Field Lengths for Take-off and Landing

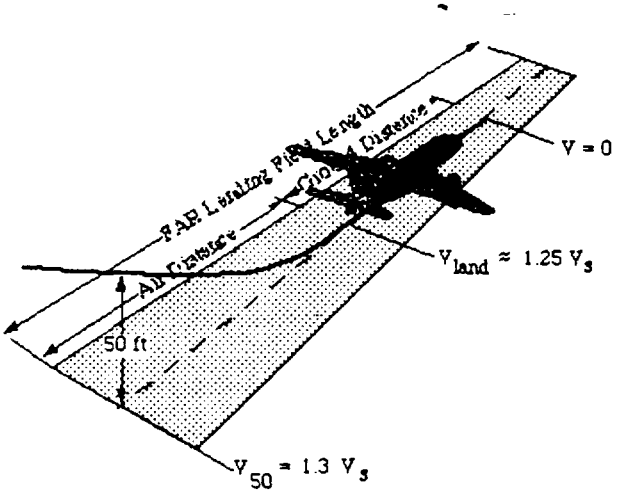

Figure 5.7: FAR Landing field length

Landing field length (LFL) requirements are detailed in FAR 25.125 and shown in Figure 5.7. LFL distances consist basically of two segments, an air run from a height of 50 feet to the runway accompanied by a slight deceleration and flare, and the ground deceleration from touchdown to stop [68].

The air distance can be decomposed into a glide distance and an air deceleration distance. From [68], this is approximated as:

$$d_{air} = d_{GL} + d_{decel} = 50\frac{L}{D_{eff}} + \left(\frac{V_{50}^2}{2a} - \frac{V_L^2}{2a}\right) \tag{5.3}$$

Where $D_{eff} = (D - T)$. Recognizing that for a slight maneuver, $L \approx W$, and substituting

for the acceleration, Equation 5.3 becomes:

$$d_{air} = \frac{L}{D_{eff}} \left[50 + \frac{1}{2g} \left(V_{50}^2 - V_L^2 \right) \right]. \tag{5.4}$$

The ground deceleration distance is defined as:

$$d_G = \frac{V_L^2}{2a} = \frac{V_L^2 W}{2gR} \tag{5.5}$$

where: R is the effective average resistance or total stopping force $\mu (W - L) + D$. μ is the braking coefficient of friction taken to be between 0.4 and 0.6 on dry concrete and 0.2 to 0.3 on wet concrete.

The stall speed, the lowest speed for steady flight, in the above equations is computed as a function of the maximum attainable lift coefficient as:

$$V_{stall} = \frac{\sqrt{2TOGW}}{S_w \rho C_{L_{max}}} \tag{5.6}$$

Both V_{50}^2 and V_L^2 are taken as fixed percentages (120%) of the stall speed for safety reasons, meaning the landing distance is linear in V_s^2 plus an offset to account for the glide flare. this means that for airplanes with similar $\frac{L}{D}$ values and braking systems, the LFL equation will be of the form:

$$d_{land} = A + BV_s^2 \tag{5.7}$$

The simplified LFL prediction in this research is derived from data for FAR LFL performance of number of transport aircraft on dry runways. Equation 5.7, supported by this statistical compilation, yields [42]:

$$LFL = 750 + 0.4V_s^2 \tag{5.8}$$

As in the case of the LFL, take-off field length (TOFL) requirements are also detailed in FAR part 25. A drawing depicting the path and intermediate speeds appears in Figure 5.8. An important and often critical part of aircraft design, the TOFL is dependent upon the total weight that can be lifted from the runway to a given height. Take-off performance includes acceleration to the lift-off speed, and climb to 35 feet. The required TOFL is the

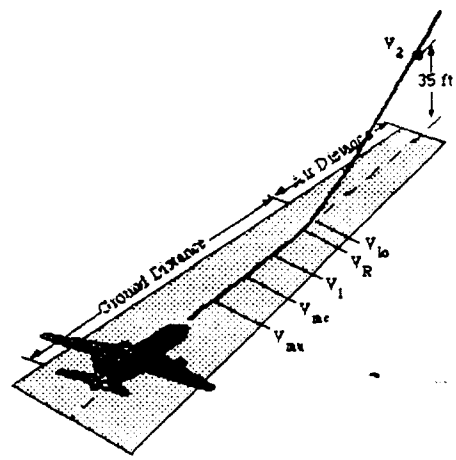

Figure 5.8: FAR Take-off field length

total distance from start to the point when the clearance height is reached.

The full commercial take-off requirements are intricate, involving acceleration and climb with various engines on and off. The preliminary design calculations, for this reason, include a statistical correlation of demonstrated performance and values of parameters which have a first-order effect on TOFL.

Fits have been made to the FAR field length requirements of 2, 3, and 4 engines with and without engine failure versus the parameter [42, 68]:

$$I = \frac{W^2}{\sigma C_{L_{max}} S T_{.7}} \tag{5.9}$$

In this equation σ is the air density ratio, and $T_{.7}$ is the total installed thrust evaluated at 70 % of the lift-off speed which is accepted as $1.2V_s$. The fits for a 4 engine aircraft, which include the supersonic transports, is [42]:

$$TOFL = 486.7 + 26.2I + 0.0093I^2 \tag{5.10}$$

In this work, as in Reference 21, the take-off and landing field lengths must not exceed 12 000 feet and 7000 feet, respectively.

5.5.3 Required thrust for climb

Aircraft must have sufficient thrust not just to take-off and cruise, but to climb at near take-off weight to the cruise altitude. The climb constraint in the aircraft optimizations of this research is expressed as a required value of the ratio drag to thrust during cruise, $(\frac{D}{T})$. Governed by FAR 25.115, climb constraints include second segment climb, and minimum climb gradients with one engine inoperative during take-off, approach, and cruise.

Supersonic transports generally satisfy second-segment climb requirements without difficulty. [42] The critical performance conditions are transonic acceleration, top-of-climb, and take-off. In this analysis, constraints are set to ensure sufficient thrust for take-off (see Section 5.5.2) and top-of-climb.

At the top-of-climb, conservation of energy requires that in order to climb, thrust must exceed the drag according to:

$$W\,(RC) + DV = TV$$

where W is the aircraft weight, RC is the climb rate, and D, T, and V are the drag, thrust, and velocity, respectively. Re-arranging this equation leads to an expression for required drag-to-thrust ratio given available thrust, Mach number, altitude, and climb rate.

$$\frac{D}{T} = 1 - \frac{(RC)W}{VT} \tag{5.11}$$

Given a required climb rate of 300 ft/min, and aircraft weights in the range of those in this dissertation, the aircraft drag must not exceed 95-98 % of the available thrust.

Chapter 6

Reduced Basis Modeling

6.1 Introduction

Any multidisciplinary optimization method, in solving an aeroelastic problem, must account for the interdisciplinary coupling of aerodynamics and structures analyses. In collaborative optimization, this task is performed by the system-level optimizer. The 3-D aerodynamics and structures analysis codes input and output arrays of loads and deflections, respectively, whose sizes are a function of the corresponding grid density. To reduce computational expense, information shared between these disciplines through the system-level optimizer should be only a subset of these arrays. The designer may restrict the design space by working with a relatively small number of the design variables for parameterization of the 3-D surface geometry, the 3-D surface pressure field, and the 3-D deflection distribution. This design variable reduction is accomplished via fitting, or reduced basis modeling. The optimizer then works with the coefficients of these fits [23]. Fitting options include least-squares polynomials, splines, and Fourier polynomials. In this research, the structural deflections and the aerodynamics loading must be available to both aerodynamics and structures, and the aerodynamics analysis is itself modeled as a response surface. The goal of this chapter is to describe the various modeling techniques applied in this research, including discussion of the sensitivity of results to fit accuracy.

6.2 Load and Deflection Design Variable Selection

It is important, when finding the correct compromise between maximum fidelity and minimum number of global design variables, to ensure that the relationship between the optimization disciplines is sufficiently captured. This includes determination of the best way to export results of wing pressures from aerodynamics and wing deflections from structures, as there may be hundreds or thousands of nodal values in a solution. A method must be developed which packages this information compactly.

Figure 6.1: Aerodynamics model for 9 degrees dihedral: Nose view.

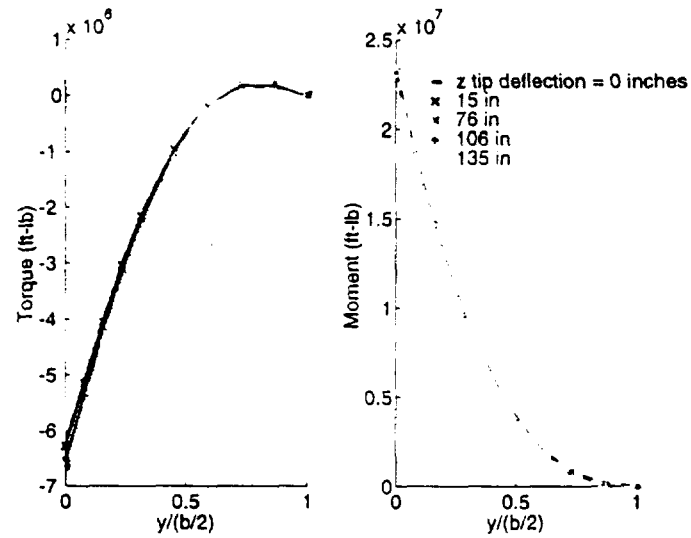

Figure 6.2: Wing load distributions as a function of dihedral. Trapezoidal wing, 3 degrees washout, α = 4 degrees at wing root. Bending moment and torque vary little with tip deflection.

The primary concern of the aerodynamics analysis is to obtain the correct spanwise twist distribution, since spanwise z deflections of the wing (a simplified example of which is shown in Figure 6.1) do little to affect the nature of the loading on the wing. Figure 6.2 is a plot of the spanwise bending moment and torque distributions in the aerodynamics analysis for different wing dihedral angles. The legend shows the associated tip deflection. The plot

supports the claim that z deflection does little to affect these particular load distributions. On the contrary, Figure 6.3 is a plot of this same loading with respect to wing twist. The effect, shown for a range of 5 degrees washout to 5 degrees washin, is orders of magnitude greater. Thus the net change in twist from the structural deflections is more valuable to the aerodynamics analysis than the pure z deflections. The entire deflection grid *would* be used were it not imperative to retain the maximum amount of information with the minimum number of variables to describe that information. As the z deflection does not affect the result of interest, and the twist alone can be conveniently modeled, the twist alone is retained.

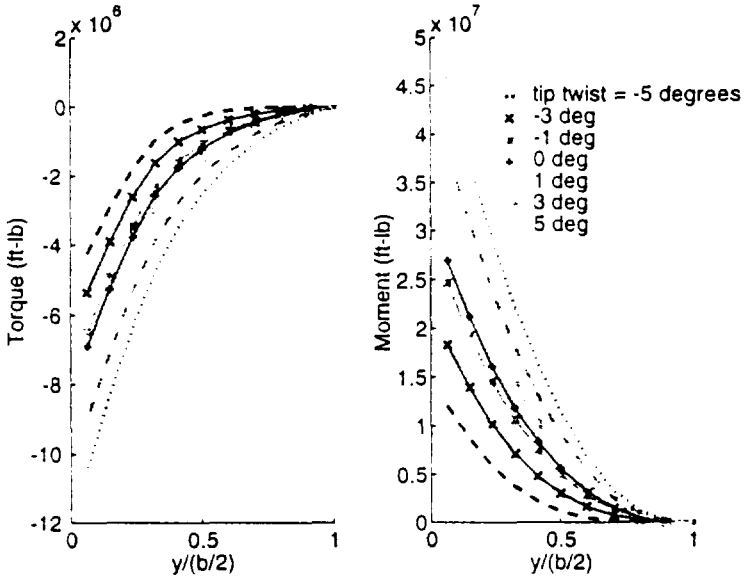

Figure 6.3: Wing load distribution as a function of twist. Trapezoidal wing, no dihedral, $\alpha = 4$ degrees at wing root.

The aerodynamics discipline analyzes two flight conditions selected from those listed in Table3.2.1; a cruise condition, and one of many off-design conditions. The off-design condition selected to be the critical condition for structural analysis is a 2.5 g pull-up maneuver, thus a load factor of 2.5 exists between the 1.0 g cruise and 2.5 g maneuver conditions. In each of the two flight regimes, the analysis can select an associated angle of attack and twist distribution. The cruise condition result computes the lift to support the TOGW and the L/D. Both the pull-up lift and the pull-up load distribution result from the maneuver condition analysis. For any condition, the twist is a combination of the

built-in "jig" twist and the twist due to the structural deflections associated with the flight condition. Aerodynamics locally has the option of altering the jig twist independently of structural twist to aid performance. Similarly, the aerodynamic loads for each condition are the zero-lift loads, the loads due to angle of attack, and the loads due to the total deflections (both jig and structural). Assuming linearity, and recognizing that the structural deflections in any condition are independent from the jig twist, the maneuver spanwise distribution of streamwise twist is:

$$\bar{\theta}_{man} = \bar{\theta}_{jig} + \bar{\delta}_{man}, \tag{6.1}$$

were $\bar{\delta}_{man}$ is the twist distribution due to structural deflections. The corresponding cruise twist distribution would be:

$$\begin{aligned} \bar{\theta}_{cr} &= \bar{\theta}_{jig} + \bar{\delta}_{cr} \\ &= \bar{\theta}_{jig} + \frac{\bar{\delta}_{man}}{2.5} \end{aligned} \tag{6.2}$$

where 2.5 is the maneuver condition load factor.

In reality, even assuming linearity, the relation in Equation 6.2 only holds if $\bar{\theta}_{jig} = \{0\}$. For non-zero jig twist, an aircraft flying at zero angle of attack will experience some structural deflections *different* from the 1-g deflections of the zero jig twist configuration. This effect of the jig twist on the structural deflections is neglected in Equation 6.2. For $\bar{\theta}_{jig} = \{0\}$ is it clear that the only information shared by structures and aerodynamics disciplines are simply the maneuver loads (from aerodynamics) and the maneuver deflections (from structures). Thus the spanwise moment and torque distributions are extracted from the aerodynamics load grid in the maneuver condition and the spanwise twist distribution is compiled from the deflected structure. As will be seen in Chapter 7, this is the approach taken in design and optimization of the conventional HSCT aircraft.

6.3 Design Variable Modeling

Recall that the the structural analysis requires the spanwise torque and bending moment distributions in order to accurately compute the deflections and stresses of the wing elements. Similarly, the aerodynamics discipline uses the streamwise twist resulting from the structural deflection under load. For this reason the spanwise distributions of bending

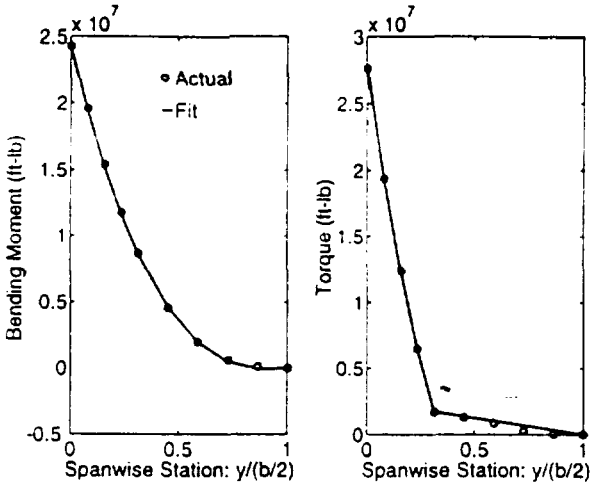

Figure 6.4: Polynomial fits of wing bending moment and torque. Moment is 3rd order, torque is 3rd order inboard, 1st order outboard.

moment, torque, and streamwise twist were studied for many cases to determine their nature, and suitable reduced basis representations were sought. The aerodynamic torque and bending moment were modeled using two different approaches: least-squares polynomial fits, and spline fits. Similarly the spanwise twist distribution in structures is modeled using polynomials and simple splines. Methods were chosen with considerations for accuracy, number of required coefficients, and design variable physicality.

6.3.1 Modeling Aerodynamic Loads with Least-squares Polynomial Fits

Figure 6.4 shows plots of wing bending moment and torque as they vary with span for a typical maneuver condition of the conventional HSCT wing. Though the magnitudes change with wing incidence and altitude, the nature of the curves are well represented by this example. Initially, the chosen model was that of least-squares polynomial fits to the data.

A polynomial defined as:

$$y = b_o + b_1 x + b_2 x^2 + \cdots + b_m x^m \tag{6.3}$$

can be solved by a method of least-squares by a polynomial function fit. Given n ordered pairs of inputs and computed values $\{(x_i, z_i)\}$ for $i = 1, 2, \ldots, n$ a set of equations can be

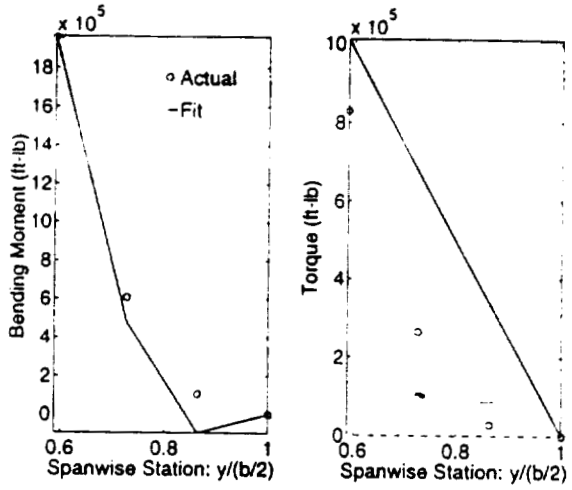

Figure 6.5: Polynomial fits of the wing bending moment and torque from Figure 6.4, outboard spanwise stations.

formed:

$$\begin{aligned} nb_o + b_1 \sum x_i + b_2 \sum x_i^2 + \cdots + b_m \sum x_i^m &= \sum z_i \\ b_o \sum x_i + b_1 \sum x_i^2 + b_2 \sum x_i^3 \cdots + b_m \sum x_i^{m+1} &= \sum x_i z_i \\ &\vdots \\ b_o \sum x_i^m + b_1 \sum x_i^{m+1} + b_2 \sum x_i^{m+2} \cdots + b_m \sum x_i^{2m} &= \sum x_i^m z_i \end{aligned} \tag{6.4}$$

or in matrix form:

$$\begin{bmatrix} n & \sum x_i & \sum x_i^2 & \cdots & x_i^m \\ \sum x_i & \sum x_i^2 & \sum x_i^3 & \cdots & x_i^{m+1} \\ \vdots & & & & \\ \sum x_i^m & \sum x_i^{m+1} & \sum x_i^{m+2} & \cdots & x_i^{2m} \end{bmatrix} \begin{bmatrix} b_o \\ b_1 \\ \vdots \\ b_m \end{bmatrix} = \begin{bmatrix} \sum z_i \\ \sum x_i z_i \\ \vdots \\ \sum x_i^m z_i \end{bmatrix}$$

in which $\{b_o, \cdots, b_m\}$ are the coefficients of the fit.

Physics dictates that the moment and torque go to zero at the wing tip. For say, a third-order moment fit, the constant term is zero, and Equation 6.3 can be rewritten in this case as:

$$Moment = b_1 \left(\frac{span}{2} - y \right) + b_2 \left(\frac{span}{2} - y \right)^2 + b_3 \left(\frac{span}{2} - y \right)^3 \tag{6.5}$$

in which y is the non-dimensional spanwise location on the wing. Equation 6.5 requires that $Moment$ and $\frac{dMoment}{dy}$ are zero at the wing tip where $y = \frac{span}{2}$. The torque equation is handled in this manner as well.

Due to the nature of the conventional HSCT wing, the spanwise torque distribution is not a smooth function, rather it has a break at the point where the leading edge sweep changes dramatically. For this reason two separate polynomial fits are matched at this location. The symbols on the plots are the actual values as computed by the aerodynamics

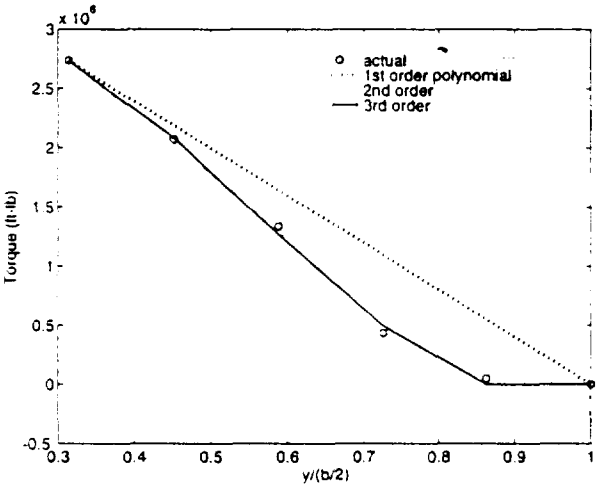

Figure 6.6: Torque polynomial fits of varying order, 4 outboard spanwise stations.

analysis, and the lines are the polynomial fits determined to represent these actual values. The coefficients of the polynomial fits are eventually passed to the system-level optimizer. Figure 6.5 is a close-up of Figure 6.4 on the outboard 4 stations of the 9-station panel approximation of the wing. In this zoomed view, it is clear that the fits in the outboard region are not accurate. The first-order polynomial then, may not be sufficient to fit the outboard torque. A comparison of torque fit using second and third order polynomials appears in Figure 6.6. The higher order fits more accurately predict the torque, however, there are two goals of a successful model: accuracy and sufficient order reduction. The use of a third order polynomial fit inboard *and* outboard drives up the number of global variables which must be passed around in the optimization, increasing the complexity and run-time of the optimization. The moment polynomial has a different issue. The fit predicts a negative moment just inboard of the tip (not matching the slope at the tip). If the reduced basis model used incorrectly predicts negative moment values, that would necessarily lead

to negative forces at the tip, and a very improper nodal loading. For the above reasons, alternate fits were selected to model both the bending moment and torque, and are described in the following section.

6.3.2 Spline and Alternate Least-Squares Load Models

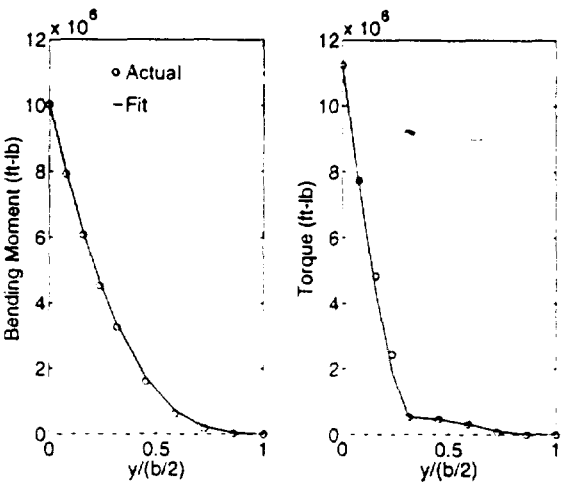

Figure 6.7: Spline fits of torque and alternate least-squares fit of moment distribution.

A spline can be more accurate than a single polynomial because it is a piecewise cubic polynomial fit between each of any chosen knot points. In the case of the least-squares polynomials, the coefficients are the values taken as the design variables. In the case of the splines, design variables are the chosen knot points at which to exactly match the value to be fit. A spline was chosen to rival the two polynomials which modeled the torque in the previous section. The splines, like the polynomial least-squares fits, are designed to take advantage of known physics of the problem such as zero lift at the tip, fixed root boundaries, and slope matching at grid points. For this design problem, four knot points, in addition to the known zero moment and zero torque value at the root, were deemed sufficient. This fixes the number of design variables at four. The location of these four points must also be chosen to best match the fitted variable. A fit of a sample torque distribution using this method appears in Figure 6.7. Figure 6.8 focuses on the outboard fit of the torque distribution. Note the improvement over the linear fit in Figure 6.5. Though Section 6.3 indicates that higher order polynomial fits can improve accuracy in this region, the increased number of variables required to describe the fit is prohibitively expensive. The

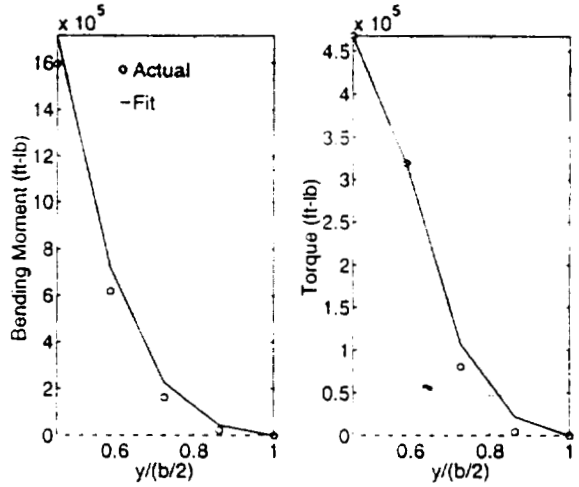

Figure 6.8: Spline fits of torque and alternate least-squares fit of moment distribution. 4 outboard spanwise stations.

cubic spline fit captures the essence of the spanwise distribution with far fewer variables for both moment and torque. In the case of the moment, a problem with the spline is that

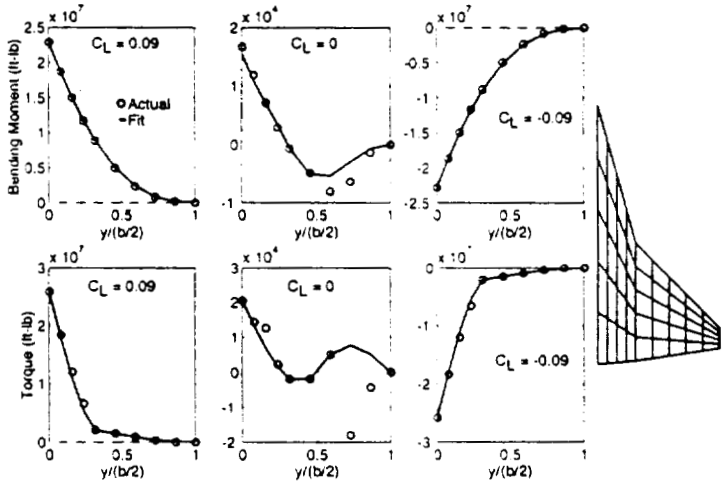

Figure 6.9: Moment and torque fits versus lift coefficient

the force distribution (essentially the derivative of the moment) is not correctly embedded within the moment distribution. A third approach was then attempted to fit the spanwise distribution of bending moment.

It is possible to develop a simple model of the force distribution which integrates in a manner such that the error in spanwise bending moment is minimized. Developing a

piecewise linear force distribution by defining the force at each of four knot locations yields a piecewise cubic moment. Values of the 4 forces must be found which bring the resultant moment as close as possible to the actual moment. This requires the solution of the following problem:

$$\begin{aligned} min: \ Error = & \sum_{1}^{N} [M(i)_{actual} - M(i)_{computed}]^2 \\ w.r.t.: \ & f_1, f_2, f_3, f_4 \end{aligned} \tag{6.6}$$

This forms a linear system of equations that can be solved directly for the force value by evaluating the moment at every spanwise location. The resulting force values represent the best possible piecewise linear force distribution for matching the moment. In addition, we are in control of the nature of the force distribution. In this case the four forces are passed as the system-level design variables. Figure 6.7 shows the actual and predicted moments using this system. Note in Figure 6.8 the moment distribution tip slope requirement is satisfied in this method unlike with polynomials, in which the moment is permitted to change sign near the tip as in Figure 6.5. Figure 6.9 shows moment and torque distributions along with

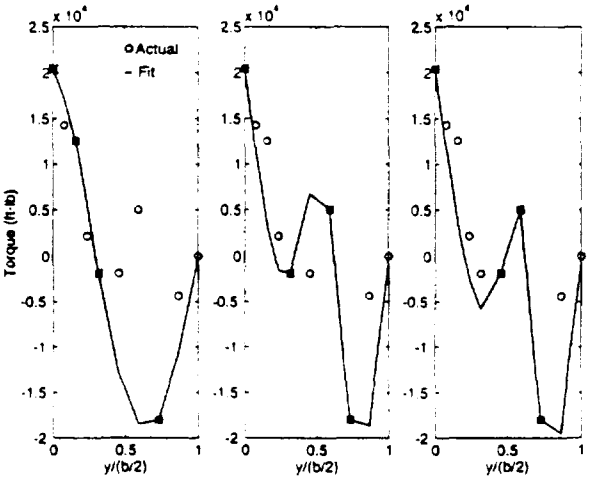

Figure 6.10: Torque fits versus spline knot location: Non-lifting case.

their fits for three lift coefficients. The torque is fit with the cubic spline and the moment with the alternate least squares method discussed in Section 6.3.2. It can be seen that for the non-lifting case, the torque fit is not very good. It is clear that for this case alternate

spline "knots" at which to match the true torque should be selected. For examples see Figure 6.10, in which the 'x' marks the spline knot at which the torque is forced to match the actual value. For the designs studied in this research however, the positive lifting case is representative, and the selected spline knot locations are acceptable. Additional benefits to using a spline for the torque and the assumed forces for the moment is that the passed variables are four forces and four torques. These values are more intuitive to the user than polynomial fit coefficients.

6.3.3 Deflection Design Variable Modeling

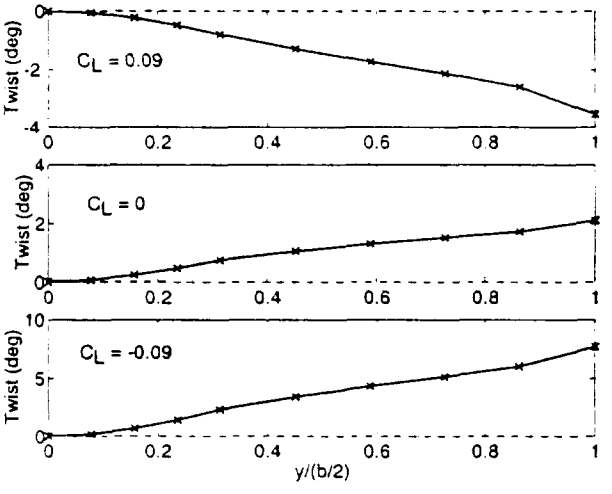

Figure 6.11: Structural twist versus lift coefficient, with applied loads from Figure 6.9.

It was shown in Section 6.2 that the primary concern of the aerodynamics analysis with regards to the structural analysis is to obtain the correct spanwise twist distribution. The twist distribution resulting from structural deflection under load was studied for many cases to determine its nature. As a function of the skin, spar, and rib finite element thicknesses, propulsion sizing, and fuel distribution as well as aerodynamics loading, a variety of maneuver twist distributions may appear in the process of designing an aircraft. Applying the loads corresponding to Figure 6.9 to a typical FEM model yields structural deflections leading to the twists in Figure 6.11. In all cases, the twist is rather smooth, and should be easy to model. Two methods of fitting the positive lifting case in Figure 6.11, a third order polynomial fit and a simple spline, are compared to the actual twist in Figure 6.12. Each does a sufficient job of portraying the twists. The simple spline is the method of choice. As

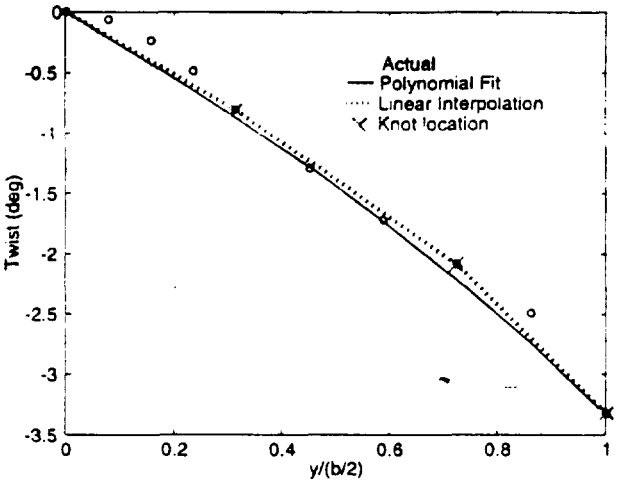

Figure 6.12: Structural twist fitting options.

previously mentioned, it is desirable to select system-level design variables which are easily recognizable and a good representation of the aircraft. In the simple spline method, the design variables are actual twists at given spanwise locations, while the design variables in the polynomial fit case are coefficients which are not so recognizable. Three spline knot locations, corresponding to three system-level design variables, are sufficient to describe the twist. In this research, both the built-in jig twist and the spanwise distribution of the structural twist are modeled by spline fits.

6.3.4 Extracting Structural Nodal Load Grid from Spanwise Fits

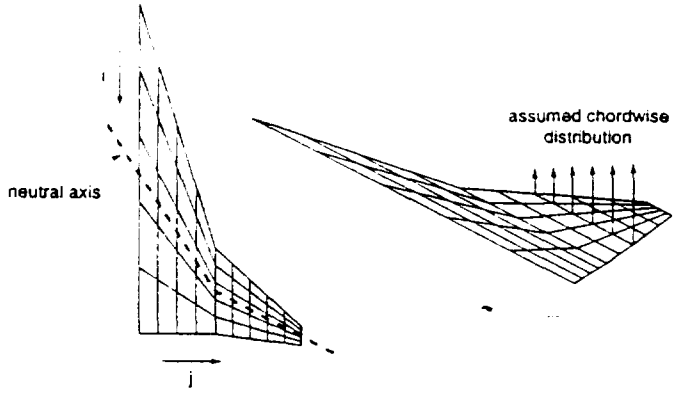

Figure 6.13: Structural load extraction parameters.

In the aerodynamics discipline, the wing grid and the panel pressures are computed. Combining this information with the known flight conditions, the spanwise wing loading is computed, from which the spanwise moment and torque distributions are built. The coefficients of the fits to the moment and torque are inputs to the structures discipline and are used to rebuild the spanwise distributions of bending moment and torque. With a goal of reconstructing the actual wing load distribution, structures must, in the process, back out the spanwise lift distribution (from the moment fit) followed by the spanwise local torque distribution (from the wing loading and the torque fit). The local torque is essentially the pitching moment at each spanwise station of the wing due only to loads at that spanwise station.

Spanwise moment distribution dictates the spanwise lift distribution $F(j)$ where:

$$F(j) = \sum f(i,j) \tag{6.7}$$

Figure 6.13 defines the i and j directions. The spanwise torque, when decomposed at each spanwise station into the local torque due only to nodal forces along the chord at that station, provides the local moment about the neutral axis.

$$T_{local}(j) = \sum f(i,j)\,(x(i) - x_{na}(i)) \tag{6.8}$$

To determine the chordwise distribution of force values at a spanwise station given the local torque and the force, the chordwise distribution shape, as shown in Figure 6.13, must be

specified. As discussed in Sections 1.3.1.2, and 3.5.1 and as shown in Figures 1.12 and 3.10, the chordwise pressure distribution for the low-cambered supersonic thin airfoils of the HSCT is very close to linear. The forces are defined as:

$$f(i,j) = m(j)\,x(i,j) + b(j) \tag{6.9}$$

Solving for $m(i)$ and $b(i)$ allows computation of $f(i,j)$. $f(i,j)$ then splits between nodes of the upper and lower surfaces.

This procedure captures essential aspects of the aerodynamics loading for application to the structural finite element model. Excessive or inaccurate fitting techniques can cause a loss of information. For this reason, the accuracy of this method affects the optimization results, and it is imperative that the aerodynamics and structures disciplines are working with the same forces and deflections. The following section discusses the effect of bending moment and torque fit accuracy on the structural calculations.

6.4 Effect of the Aerodynamics Loads Model on Structural Analysis Results

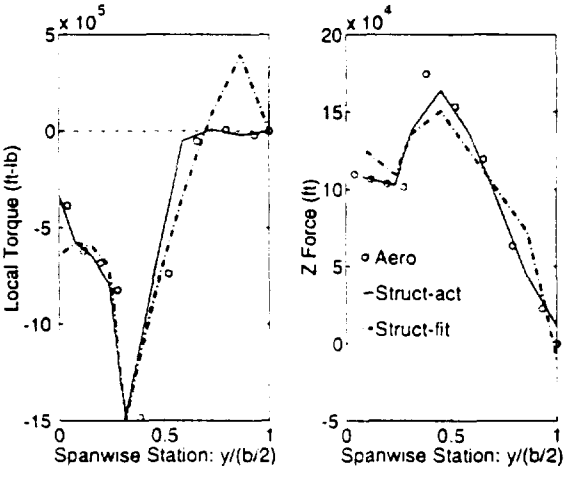

Figure 6.14: Spanwise distributions of local torque and lift. Shown are values computed by aerodynamics (Aero), structural results given polynomial moment (cubic) and torque (cubic inboard, linear outboard) fits (Struct-fit), and structural results given actual moment and torque computed by aerodynamics with no fitting (Struct-act).

Section 6.3 discussed the methods of fitting the loads and deflections in order to come up with a reasonable number of design variables. Accuracy was a primary goal. In the process of determining whether a particular reduced basis model is suitable, the effect of the aerodynamic load data on the accuracy of the structures discipline is analyzed. It was clear from the previous section that the methods vary in accuracy, but how much does this fit accuracy actually affect the analyses which use them as inputs? In this section the results of the least-squares polynomials and of the spline (torque) and assumed force fit (moment) are evaluated by determining how much their accuracy affects the forces, local torques, and deflections computed in the structural analysis. In order to assess the effect

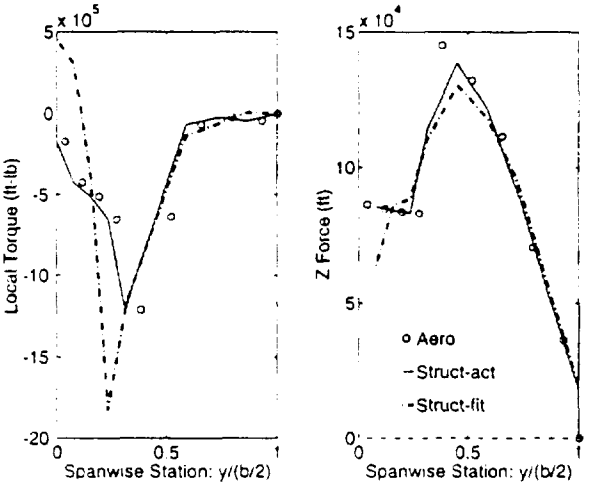

Figure 6.15: Spanwise distributions of local torque and lift. Shown are values computed by aerodynamics (Aero), structural results given least-squares moment and cubic spline torque fits(Struct-fit), and structural results given actual moment and torque computed by aerodynamics with no fitting (Struct-act).

of the fits on the structures discipline accuracy, this analysis is run using first the fits of the spanwise distributions of moment and torque, then using the moment and torque distributions as computed by aerodynamics. In the process of obtaining the full nodal load grid, structures extracts from the moment and torque distributions the spanwise lift distribution and the spanwise local torque distribution. For comparison purposes, these latter two values were computed in aerodynamics also, directly from the panel code output, with no fitting. Figures 6.14 and 6.15 show plots of local torque and spanwise lift as computed by aerodynamics (Aero), by structures given the moment and torque fits (Struct-fit), and by structures given the actual moment and torque distributions (Struct-act). It

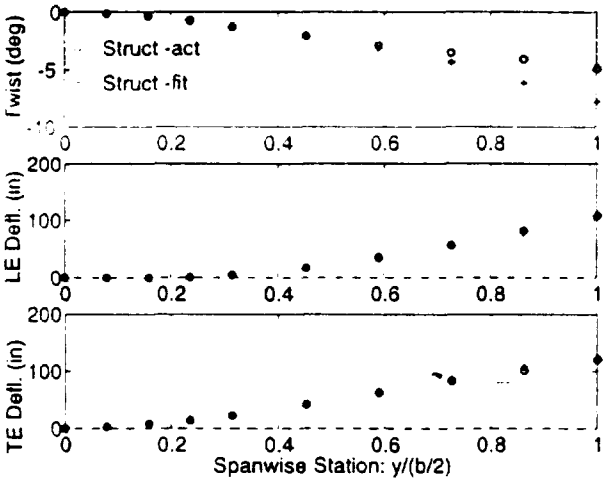

Figure 6.16: Spanwise distributions of structural deflections and twist. Shown are structural results given polynomial moment and torque fits (Struct-fit), and structural results given actual moment and torque (Struct-act).

should be noted that aerodynamics computes the spanwise load distribution from panel centroid data, and structures computes values at nodal points (panel edges). The root nodes on the structural finite element model are fixed, so the values are essentially shifted from the centroids of aerodynamic panels, to the nodes (excepting the root) of the structural model. The fits in Figure 6.14 are the original polynomial fits in moment and torque, with linear outboard fit in torque. The "fit" curves in Figure 6.15 were computed using the least-squares fit for the bending moment and a cubic spline for the torque. The lines in Figure 6.14 show that given the actual moment and torque distributions, structures does a much better job of approximating the aerodynamics local torque and lift than if given the fits. Therefore, a much better system of fits then polynomial is necessary to capture especially the outboard moment and torque values. The splines and alternate least-squares model previously discussed comprise that system, and Figure 6.14 shows much better results. Of additional interest is the effect the fit accuracy in the structures analysis has on the structural deflections and computed twist. Figure 6.16 shows the leading and trailing edge z displacement along with the resultant spanwise twist due to the load grid computed from the actual moment and torque values and from those extracted from polynomial fits. Figure 6.17 shows the same result from the least-squares and spline fits. Additionally, for the selected fitting method, Figure 6.18 shows the entire z-deflection grid in given the actual moment and torque and the fits, and a plot of the difference in the two. The largest

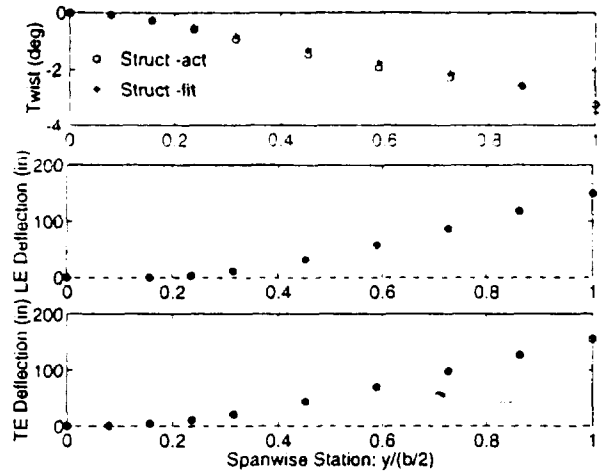

Figure 6.17: Spanwise distributions of structural deflections and twist. Shown are structural results given least-squares moment and cubic spline torque fits(Struct-fit), and structural results given actual moment and torque (Struct-act).

difference is just under two inches, and occurs near the tip.

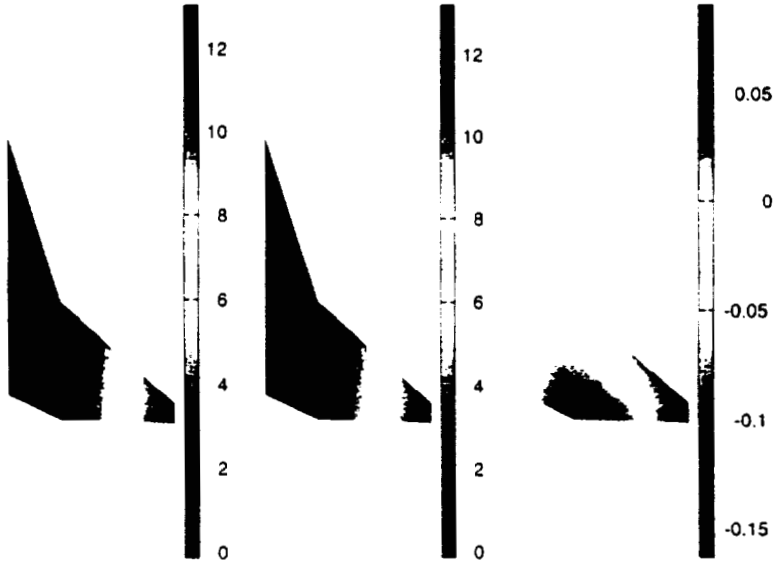

Figure 6.18: Structural z deflection contours from actual and fit loadings. a) Actual loading. b) Fit loading (least-squares moment fit and cubic spline torque fit) c) Difference in deflections from actual and fit loading. (All dimensions in feet)

6.5 Response Surface of the Aerodynamics Analysis

The aerodynamics analysis is based on the surface panel method A502. The optimizations performed in this design process are gradient-based, and this leads to a problem with the aerodynamics discipline. Convergence of aerodynamics alone was difficult to achieve, (the optimizer would often get stuck in one region of the design space and at times never move far from the starting point) and investigation revealed poor gradients from A502, a sample of which appear in Figure 6.19. It was revealed that though the code A502 is written in double precision, this large code depends a great deal upon internal file I/O. These files do *not* carry information to double precision. This causes an inability to capture the sensitivity of the computed values, such as force coefficients, to very small changes in inputs. Several attempts to increase the internal precision of A502 improved the situation, but did not fully rectify the problem. The gradient-based optimizer used in this research absolutely needs this smooth gradient information with small perturbations. Other A502 users have also experienced problems obtaining smooth gradients from A502, both subsonically and supersonically. As a result of these problems, a response surface is created of the aerodynamics analysis. The procedure to create the aerodynamics model is described in the following section.

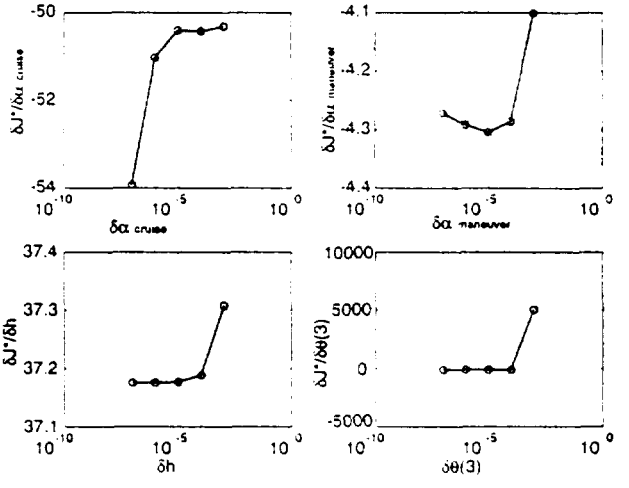

Figure 6.19: A502 gradient of objective function versus perturbation of selected design variables.

6.5.1 Aerodynamics Response Surface Creation

For a fixed planform the aerodynamics analysis has to vary with many inputs:

- angle of attack for the cruise and maneuver conditions (α_{cr} and α_{man})
- Engine thrust ($SLSTH$)
- Initial cruise altitude, h_{init}
- Fit coefficients of the structural deflections , $\delta(3)$
- Fit coefficients of the built-in jig twist distribution, $\theta(3)$

for a total of 10 variables. The output required of the aerodynamics analysis in order to perform optimization is:

- Cruise lift
- Cruise L/D
- Maneuver Lift
- Fit coefficients of the spanwise bending moment, $f(4)$
- Fit coefficients of the spanwise torque, $T(4)$

for a total of 11 outputs.

In order to create a response surface of this analysis suitable for the required optimization, a method was developed which supplies the required information in the fewest number of function evaluations. The method is efficient enough as long as it runs faster than the slowest optimization discipline. To create a quadratic response surface in 10 variables, $\frac{(n+1)(n+2)}{2}$ or 66 runs of the analysis are necessary. Recalling that each run of the analysis required two function evaluations, one of the maneuver condition and one for the cruise, the number of function evaluations doubles. This number can be reduced by analyzing the physics of the aerodynamics problem. Though the maneuver and cruise conditions run with different twists, they each include the jig twist. If, then, the option is given to combine the jig and structural deflections into a total twist *before* running the analysis, the total number number of variables according to the response surface would be 7, for a total of 36 runs, or 72 function evaluations for a savings of over 45 percent. Additionally, if it is recognized that

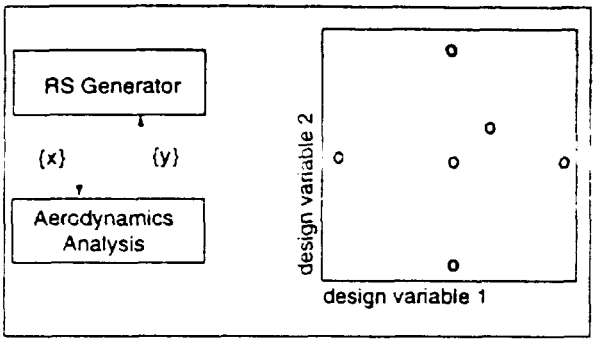

$$\{x\} = \{\alpha_{cr}, \alpha_{man}, SLSTH, \delta(3), \theta(3)\}$$
$$\{y\} = \{TOGW, \frac{L}{D}, Lift_{man}, f(4), T(4)\}$$

Figure 6.20: Aerodynamics response surface creation.

the only effect altitude has on some outputs is to scale them with density, then the scaling can be performed after the response surface result is obtained, leaving the altitude out of the design variable list. This further reduced the number of required function evaluations to 56. Now that the number of design variables is decided, it must be said what to fit. Instead of fitting the composite discipline result J*, each of the outputs is fit independently, so there is a total of 11 response surfaces.

There is a basic method for defining the design space and selecting the points for evaluation. A center point is chosen, one which seems to represent the center of the current system-level design space. Then perturbations are picked for how far to move in any direction alone and in combination. A sample design space for a two-dimensional slice of this multidimensional response surface appears in Figure 6.20. The procedure is to generate and solve a linear system based upon first order and second order combinations of variables and results of the $\frac{(n+1)(n+2)}{2}$ data points in each response surface, and is termed Multiple Linear Regression.

6.5.2 Multiple Linear Regression

Multiple linear regression can be applied to give the least-squares fit to any polynomial function in any number of variables. Essentially coefficients of a fit are found such that the sum of squares of the errors is a minimum. Given the desire to fit a function J yielded by independent variables x and y, a quadratic response surface can be created from $\frac{(n+1)(n+2)}{2}$ linearly independent combinations of x, y and corresponding J.

The point set is created by perturbing each variable alone as well as pairs of variables simultaneously, spanning the space around the initial, or *base* point. Subtracting each of

Variable	Cruise Condition	Maneuver Condition
α_{cruise} (deg)	3.3	-
$\alpha_{maneuver}$ (deg)	-	3.3
$twist_1$ (deg)	-1.78	-1.9
$twist_2$ (deg)	0.58	0.3
$twist_3$ (deg)	-1.1	-1.6
$SLSTH$ (lb)	50 000	50 000

Table 6.1: Response surface center design point.

the points in the space from the base point yields $\frac{(n+1)(n+2)}{2} - 1$ points, denoted by dx, dy, and dJ.

For any given choice of coefficients A,B, ...E the square of the "error" for the first data point is:

$$\left[Adx + Bdy + Cdxdy + Ddx^2 + Edy^2 - J\right]^2 \tag{6.10}$$

Summing the squared error for each of the data points gives the total sum-of-squares for all the errors. This yields an expression identical to the one above, except that dx is replaced by $\sum_{i=1}^{N-1} dx_i$ and $dydx^2$ is replaced by $\sum_{i=1}^{N-1} dy_i dx_i^2$, and so on. In the following, let $[*]$ denote the sum of the bracketed expression over all data points. Taking the partial derivative of this total sum of squares with respect to each coefficient, and setting each partial to zero gives the minimum sum of squares in an equation of the form: $[A][coeff] = [RHS]$ and the coefficients are found in the usual way, where $[coeff] = [A]^{-1}[RHS]$.

This procedure is followed for each of the variables to be fit. That is: if the variables of interest are L/D, Root Moment, and C_L, then three sets of coefficients are to correspond to each of these dependent variables.

Given a new set of independent variables $[x, y]$, the dependent variable is recreated by subtracting the base point from the point of interest and solving:

$$dJ = Adx + Bdy + Cdxdy + Ddx^2 + Edy^2 \tag{6.11}$$

$$\text{and} \quad J = dJ + J_o \tag{6.12}$$

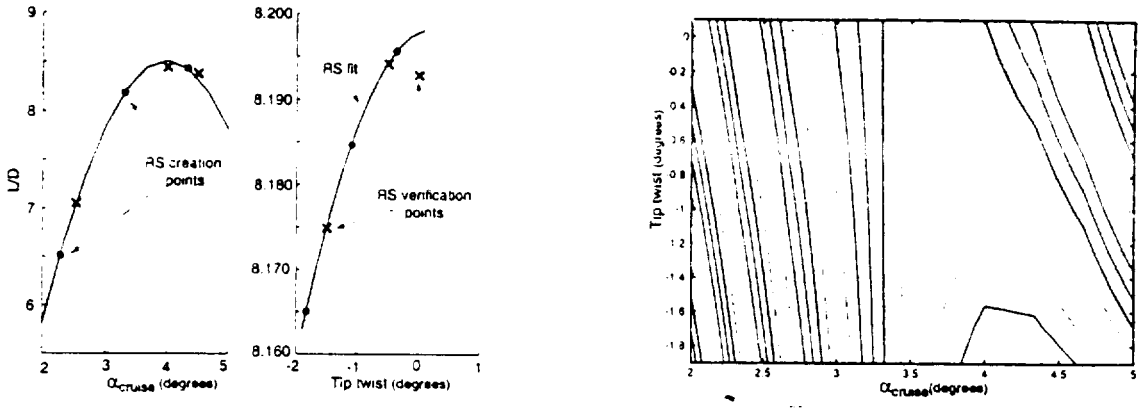

Figure 6.21: Aerodynamics response surface: L/D versus α_{cruise} and Tip twist. Line plots show response surface fitness, L/D surface and contour plots show design space.

6.5.3 Aerodynamics Response Surface Fitness

Applying multiple linear regression to the aerodynamics design variables yields a fit for each aerodynamics computed value of interest. As part of a greater optimization problem, the aerodynamics response surface is re-created essentially every cycle of the system level optimization. The choice of design space to fit, and of points within this design space to use in creating the fit are in part governed by the system-level trust region. Aerodynamics response surface variables such as $SLSTH$ and maneuver deflections are dictated by the current system-level design. Variables local to aerodynamics, such as angles of attack and jig twist, are not governed by the system-level trust region. In this case it is up to the designer to determine the location and size of the aerodynamics design space to fit for the current cycle. Local variables which yield cruise lift and L/D within the system-level trust region must be selected by the designer. This is further evidence that though collaborative optimization is a great benefit in optimizing complex systems, it is not a process which will run itself from beginning to end. Intelligent human intervention is necessary. So how accurate is a fit of the aerodynamics design space? Figures 6.21 and 6.22 help to demonstrate. For a typical response surface of the natural laminar flow aircraft, a fit is made about the center point in Table 6.1. The dependence of L/D on tip-twist and α_{cruise} appears in Figure 6.21, and root torque as a function of twist at the span-break and $\alpha_{maneuver}$ appears in Figure 6.22. The line plots show the points used to make the fit, along with intermediate results from the aerodynamics analysis to test the fit. The contour plots give a better idea of the shape of these slices of the design space. It is clear that root torque is easy to fit, it is quite

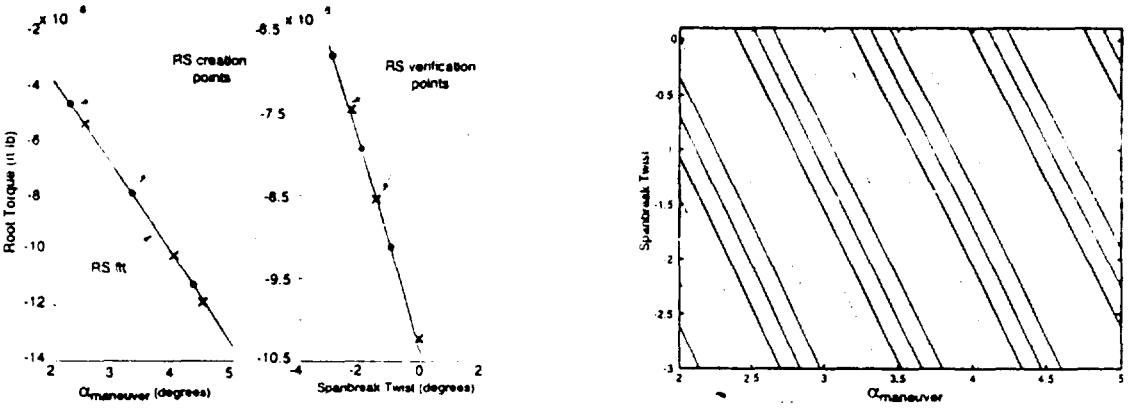

Figure 6.22: Aerodynamics response surface: Root torque versus $\alpha_{maneuver}$ and span break twist. Line plots show response surface fitness, root torque surface and contour plots show design space.

linear and extrapolation is not a problem. L/D is a quite quadratic, though extrapolation in the tip-twist dimension leads to inaccuracies. This is why the designer must be sure to pick a reasonable space to fit to allow the aerodynamics optimization subproblem to work within the system-level trust region. Generally, the perturbation values for jig twist and angle of attack is about $\pm$ one degree for the initial system-level optimization cycle. This perturbation value grows or shrinks with each cycle as needed. As in the system-level trust region update algorithm, if a design variable moves to the edge of the current trust region, the perturbation value may grow for the next cycle. If, upon inspection, the aerodynamics response surface is not an accurate representation of the aerodynamics analysis, the trust region governing the design variables local to aerodynamics shrinks.

To check the accuracy of the aerodynamics fit and its effect on the optimization solution, the design variable set selected by the optimizer to match the target values are checked in the *actual* aerodynamics analysis. Generally, this method of fitting aerodynamics proved accurate and efficient and, by definition, solves the gradient issues.

6.6 Response Surface Fits of Disciplinary Optimizations

6.6.1 Using Post-Optimality Gradient Information with Response Surface Fits

Given the vector of system-level design-variables, $\{z\}$, with n elements, applied as targets in the subproblems, and the vector of computed values $\{y\}$ and local design variables $\{x\}$ of a particular discipline, any subproblem objective is expressed as:

$$J_i^* = \sum_{1}^{a} (z_j - x_j)^2 + \sum_{a+1}^{b} (z_k - y_k)^2 \tag{6.13}$$

To make a quadratic fit of this function in the conventional manner, a set of coefficients must be found such that:

$$J_{rs}^* = c_o + \sum_{i=1}^{n} c_i z_i + \sum_{i=1}^{n}\sum_{j=1}^{n} c_{i,j} z_i z_j \tag{6.14}$$

which requires $m = \frac{(n+1)(n+2)}{2}$ data points for evaluation.

In collaborative optimization, the postoptimality condition [13, 14], dictates that the derivative of the discipline objective with respect to each system-level design variable is:

$$\frac{\partial J^*}{\partial z_k} = -2\,(x_k - z_k) \tag{6.15}$$

Therefore the solution to a collaborative optimization subproblem determines not only the value of J^*, but also the derivative of the objective, $\frac{\partial J^*}{\partial z_k}$ with respect to each target variable. Use of this information reduces the expense of response surface generation. The solution at the optimum, then, yields J^* and n solutions $\frac{\delta J^*}{\delta z_i}$, for a total of $n+1$ equations for each of m $\{z\}$ vectors. Given any two sets of $\{z\}$, say for $m = 1$ and $m = 2$, there is then: $J^*_{m=1}$, $J^*_{m=2}$, $\left\{\frac{\delta J^*}{\delta z_i}\right\}_{m=1}$,and $\left\{\frac{\delta J^*}{\delta z_i}\right\}_{m=2}$ in which the latter two have n elements apiece. However, only three pieces of information are required to make a quadratic fit. So for each pair of points, there exists 1 redundant equation.

Given the m points, there are $\frac{m(m-1)}{2}$ distinct pairs, so for the entire set there are as many redundant equations. As there are $m\,(n+1)$total equations, and the amount of

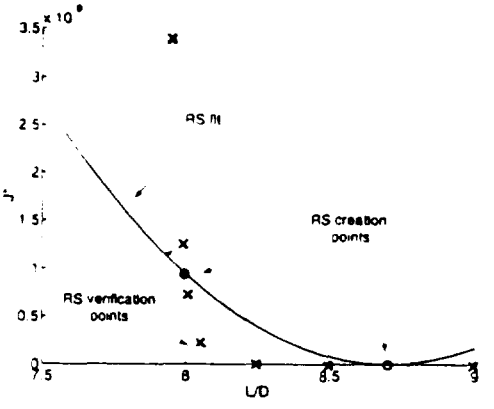

Figure 6.23: Mission subproblem response surface: J^* vs $\frac{L}{D}$

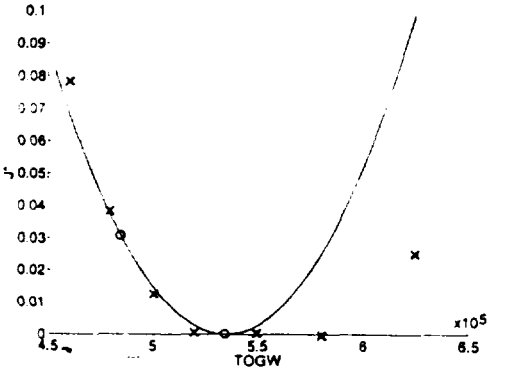

Figure 6.24: Mission subproblem response surface: J^* vs $TOGW$

information required is equivalent to $\frac{(n+1)(n+2)}{2}$:

$$\frac{(n+1)(n+2)}{2} = m(n+1) - \frac{m(m-1)}{2} \tag{6.16}$$

simplifying to $m = n+1$. [13, 14]

The required number of data points to create a quadratic fit using this gradient information is therefore only $n+1$, an order of magnitude fewer than required for a basic quadratic fit. The potential accuracy of a fit using the full set of points or using gradient information to reduce the number of required function evaluations is explored in References 73 and 71.

This result is dependent upon fitting the results of optimal solutions, for which the post-optimality gradient information is valid. One option for selecting the designs to evaluate for response surface creation is to optimize the required data points corresponding to the base point and perturbations in each variable independent of the others. A possible concern here is that as each variable is perturbed only once, the response surface is *one-sided* and is a condition which must be monitored by the designer to avoid confusing the optimizer and reducing the efficiency of the solution process. Further analysis of the response surface creation and potential difficulties appear in Section 8.2.

Figures 6.23 and 6.24 contain plots of mission J^* fits with respect to $\frac{L}{D}$ and $TOGW$ respectively. The mission design variables for these fits of the natural laminar flow aircraft are:

$TOGW$ (lb)	535 000
ZFW (lb)	247 000
Altitude (ft)	50 000
$\frac{L}{D}$	8.0
$SLSTH$ (lb)	38 000

In addition to the line representing the fit, creation points and verification points are indicated. Note there are only two creation points in each case, the baseline point and one perturbation. This perturbation size represents the trust region size, so it is clear the fits in this example have been extrapolated well outside of the trust region. Extrapolation should not occur during the optimization process.

In Figure 6.24 the baseline point is $TOGW$ =535 000 lb, corresponding to the circular data point corresponding to the lowest J^* on the plot. The other point used to create the fit is at $TOGW$ =485 000lb. In the region of the these two points, and for extrapolation to lower $TOGW$, the response surface fit is an excellent representation of the design space. Extrapolating to higher $TOGW$ values, however, yields poor results. The quadratic fit, having no information on this side of the base point, does not account for the fact that higher weight means more fuel, thus the objective function stays quite low until the $TOFL$ constraint becomes active due to the thrust requirement to accelerate the heave aircraft. Thus it is clear why extrapolation far outside the trust region is ill-advised. The problem is, the system-level optimizer sets the bounds both above and below the center point, therefore this extrapolation for increased $TOGW$ may occur. It is fortunate that the fit overpredicts J^*, thus in this case an increase in $TOGW$ helps mission compatibility.

The fit in Figure 6.23 does not fare so well. As for lift-to-drag ratio values greater than 8.0, the aircraft has plenty of lift to meet the range constraint, J^* quickly becomes quite small for $\frac{L}{D}$ values above the baseline value. This is not well represented by the fit which predicts a quadratically decreasing J^* between the creation points. Again, in this region the fit is over-predicting the value of the objective function. The fit may yield an incorrect solution in the regions far from the creation points, but ultimately, upon new point verification, as discussed in Section 2.3.3, an $\frac{L}{D}$ between 8.0 and 9.0 will be yield and improved J^*. For $\frac{L}{D}$ values less than 8.0, on the side of the baseline point no evaluated, the mission subproblem range constraint becomes active and drives J^* up. An $\frac{L}{D}$ value in this region will cause an underprediction of J^*, and could yield to an over all worse point for

the system level cycle.

The accuracy of response surfaces that fit these non-quadratic design spaces can be improved by keeping trust regions small. This means the range of $\frac{L}{D}$ and $TOGW$ which the optimizer will search is reduced, and the creation points will be much closer together in each dimension. Fortunately, collaborative optimization recognizes if a trust region is too big. If the response surface are underpredicting the objective functions, response surface verification will not yield improvements, in which case the trust region must shrink. Development of a new fitting method is one area of work that can help this optimization process.

Chapter 7

Results

7.1 Introduction

Previous chapters discuss in depth the disciplinary analyses, the optimization method, and modeling, all of which are important components of large-scale design. This chapter, after a discussion of the system-level objective functions and gradient calculations, demonstrates the design process for both conventional and natural laminar flow supersonic commercial aircraft. In these problems solved by collaborative optimization, parallel subproblem optimization in the aerodynamics, structures, and mission disciplines attempts to match target designs provided by a system-level coordinator. The system goal is to minimize the aircraft take-off gross weight while ensuring compatibility between the three disciplines. The arrangement of computed values and design variables for the aerodynamics, structures and mission discipline optimizations is shown in Figure 2.5. Results of the discipline-based optimizations are fit using response surface methods as described in Chapter 6, and updated in each 'cycle' of the system-level design problem. Progress of the design with system-level cycles, describing the collaborative implementation, will be shown in the following examples along with of the impact of design changes in performance and subsystems.

This chapter presents the first application of collaborative optimization with industry codes, and is, in the opinion of the author, the most complex problem that should be managed by an individual.

7.2 Objective Function and Gradients

As the system-level optimizer operates on response surface fits of the subproblems, it is possible that no design, represented by a design variable vector $\{z\}$, exists for which all $J_i^*(z) = 0$. Also, each optimization cycle is performed within a region of the design space, the trust region. Determination of the global optimum may require many system-level cycles and the creation of many response surfaces. As a result, response surfaces do not support system-level constrained optimization algorithms. One method of posing an unconstrained system-level problem is to combine the design objective with a penalty function:

$$J^* = f + K\left(J_a^* + J_m^* + J_s^*\right) \tag{7.1}$$

where K weights the disciplinary discrepancy values and the subscripts a, m, and s represent *aerodynamics*, *mission*, and *structures*, respectively.

At the optimum design, compatibility is achieved as all $J_i^* \approx 0$ and $J^* \approx f$.

In the following optimization problems f is the $TOGW$ normalized to order 1, and $K = 1000$, meaning that a $\sum J_i^* = 1 \times 10^{-6}$ adds the equivalent of 100 lb in $TOGW$ to the system-level objective:

$$J^* = \frac{TOGW}{1 \times 10^5} + 1000\left(J_a^* + J_m^* + J_s^*\right) \tag{7.2}$$

The derivative of the objective function with respect to each system level design variable is required for optimization with a gradient-based optimizer. It is possible to compute the gradients via finite differencing, but any chance to express gradients analytically should be exploited, as doing so reduces the required number of function evaluations and eliminates the effect of convergence tolerances and finite difference intervals on the result. This analytic gradient of the system-level objective function with respect to each design variable z_k is:

$$\frac{\partial J^*}{\partial z_k} = 1000\left[\frac{\partial J_a^*}{\partial z_k} + \frac{\partial J_m^*}{\partial z_k} + \frac{\partial J_s^*}{\partial z_k}\right] + \frac{\partial z(1)}{\partial z_k} \tag{7.3}$$

where $z(1) = \frac{TOGW}{1 \times 10^5}$ and expressions are required for $\frac{\partial J_m^*}{\partial z_k}$, $\frac{\partial J_s^*}{\partial z_k}$, and $\frac{\partial J_a^*}{\partial z_k}$.

As the subspace discrepancy values J_i^* within a given trust region are defined by quadratic response surfaces, computing analytic gradients is straightforward. Mission and

structures discipline objective functions are as expressed in Equation 2.3. If, for simplification, the subproblem local variables, $\{x\}$, and computed state variables $\{y\}$, are combined into an array W,

$$W = \{x_1 \ldots x_a\}, \{y_1 \ldots y_b\} \tag{7.4}$$

then gradients are expressed as follows with respect to $\{z\}$, and W:

$$\frac{\partial J_j^*}{\partial z_k} = \frac{\partial}{\partial z_k} \sum_{i=1}^{n} (W_i - z_i)^2 \tag{7.5}$$

The post-optimality condition [13], [14] dictates that the derivative of the discipline objective with respect to each system-level design variable is:

$$\frac{\partial J^*}{\partial z_k} = -2 (x_k - z_k) \tag{7.6}$$

The contribution of the aerodynamics subproblem to the system-level objective gradient, $\frac{\partial J_a^*}{\partial z_k}$, is expressed in a similar fashion. System-level gradient information then, as expressed in Equation 7.3, may be obtained analytically, without finite difference approximation, increasing accuracy and reducing computation time.

7.3 Conventional HSCT Optimization

The inter-disciplinary design variables specified by the system optimizer for the conventional HSCT problem are listed in the following table along with the selected values for the initial design.

Conventional HSCT baseline design variables			
Variable	*Value*	*Variable*	*Value*
TOGW (lb)	745 000	F_1 (lb)	12 300
ZFW (lb)	350 000	F_2 (lb)	14 090
Initial cruise altitude (ft)	52 000	F_3 (lb)	18 956
SLSTH (lb)	60 000	F_4 (lb)	11 041
L/D	8.30	T_1 (ft-lb)	2.73×10^7
δ_1 (deg)	-0.9	T_2 (ft-lb)	2.19×10^6
δ_2 (deg)	-1.5	T_3 (ft-lb)	1.58×10^6
δ_3 (deg)	-3.0	T_4 (ft-lb)	9.82×10^5

In this table, δ_1 through δ_3, F_1 through F_4, and T_1 through T_4 are the spline fit coefficients representing the spanwise distributions of wing structural twist, bending moment, and torque, in a 2.5g high-speed pull-up maneuver condition. The origin of these 11 variables is discussed in Chapter 6. The wing planform, as fixed for this design problem, is shown with selected additional parameters in Figure 1.15.

The system goal is to minimize the take-off gross weight ($TOGW$) of a 250 passenger, Mach 2.4, aircraft accounting for a number of discipline constraints:

Disciplinary optimization constraints			
Discipline	*Constraint*	*minimum*	*maximum*
Mission	Range	5000 n.mi.	∞
	Take-off field length	0	12 000 ft
	Landing field length	0	7000 ft
	Drag/Thrust	0	0.95
Structures	$\frac{\sigma}{\sigma_{max}}$ (*each finite element*)	-1.0	1.0
Aerodynamics	Maneuver Lift	2.5**TOGW*	2.5**TOGW*

As indicated in the flowchart in Figure 2.8, the first step in this collaborative optimization process is to select a trust region of variable bounds inside which to create a response surface. For example, the starting trust region for the aircraft $TOGW$ is $\pm$30 000 lb , and that of *altitude* is $\pm$5000 ft. The system-level optimizer will operate in this range about the starting design. The trust region in this design problem is sixteen-dimensional, thus difficult to visualize. For fair comprehension, a sample trust region in the variables of *altitude* and

TOGW is shown in Figure 7.1. The large rectangle indicates absolute variable bounds, and the smaller rectangle within denotes the current trust region. At the center of the trust region lies the baseline aircraft, and the remaining dots represent additional target designs evaluated by the subproblems to create a response surface for this subspace. The design

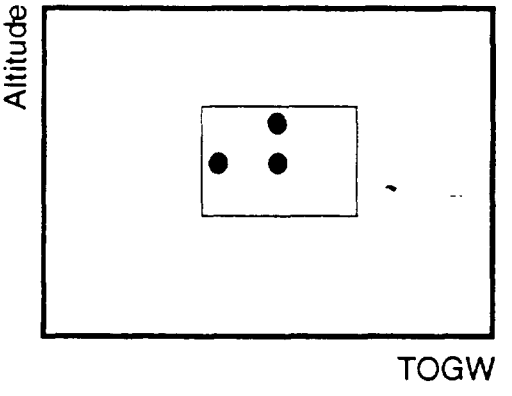

Figure 7.1: Sample initial trust region

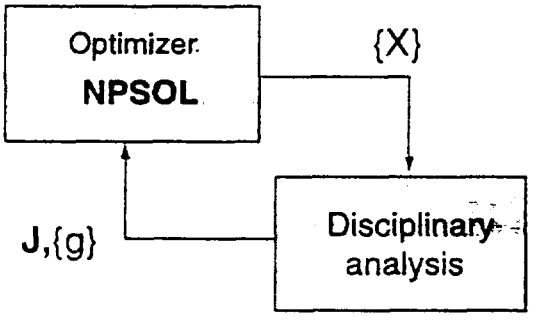

min: $J = (TOGW\text{-}TOGW_o)^2 + (Altitude\text{-}Altitude_o)^2$

st: {X} = (TOGW, Altitude)

wrt: {g} = local constraints

Figure 7.2: Sample discipline optimization problem

progression and cycle fitness checks to follow are based upon each cycle's center, or baseline point. In the process of creating their respective response surfaces, the subproblems optimize as in Figure 7.2, matching as close as possible the target design defined by the system-level optimizer.

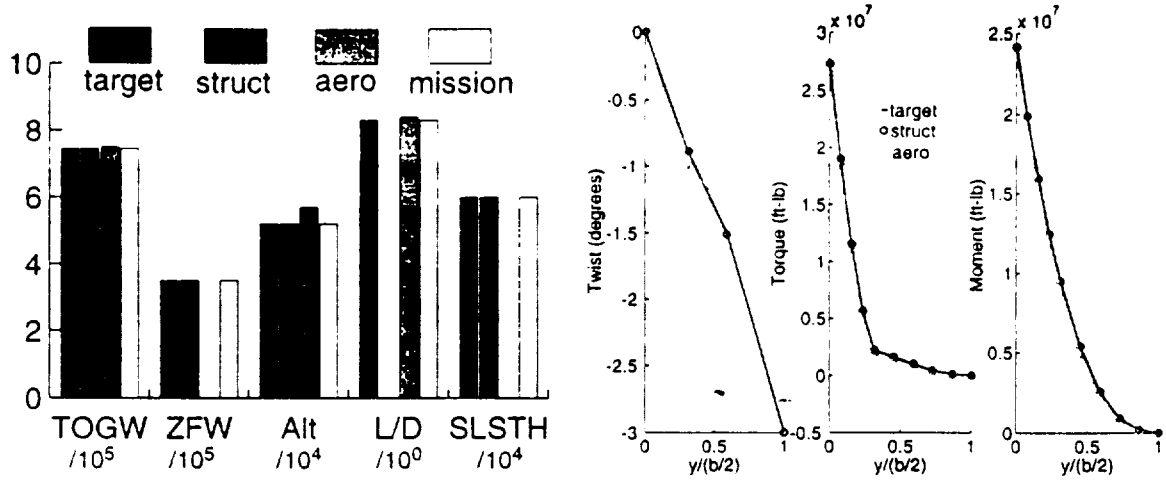

Figure 7.3: Disciplinary results: Cycle 1

Disciplinary results for cycle 1 appear graphically in Figure 7.3 along with the cycle target design variables.[1] A better match yields an improved subproblem discrepancy value J_i^*, thus a lower overall objective, J^*. The discipline and system-level objective function values for cycle 1 are:

J^*	J_a^*	J_m^*	J_s^*
1089	1.09	2.33×10^{-9}	3.9×10^{-4}

The plots in Figure 7.3 indicate discernible discrepancies between the target variables and the aerodynamics subproblem result in *altitude*, L/D, $TOGW$, and $\{\delta\}$. Given a higher target *altitude* and lower δ_3 in this initial design, the aerodynamics subproblem would have returned a lower discrepancy value, J_a^*. The other two disciplines were able to match the system-level targets more closely, while still satisfying their respective local constraints. The structures and aerodynamics subproblems return no result for L/D and ZFW respectively (see Figure 7.3), as in these graphs, a subproblem will return no result for variables by which it is not affected. Disciplines compute their respective J_i^* values for each selected design within the trust region, and response surface fits are created. The system-level optimizer operates on the response surfaces to minimize the objective function within the trust region. In Figure 7.4, the new point is marked with an X. A comparison of the original design to

[1] Numerical values of all target variables and disciplinary results for each optimization cycle are compiled in Appendix B.3.

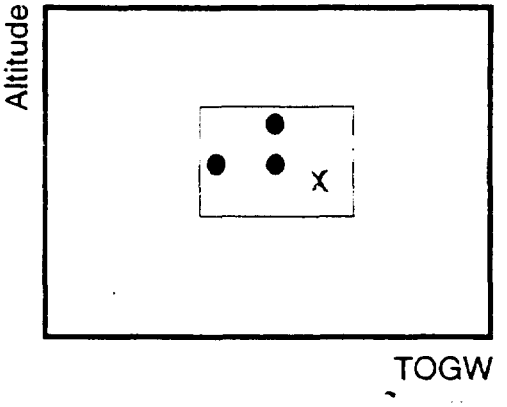

Figure 7.4: Improved point (X) within initial trust region

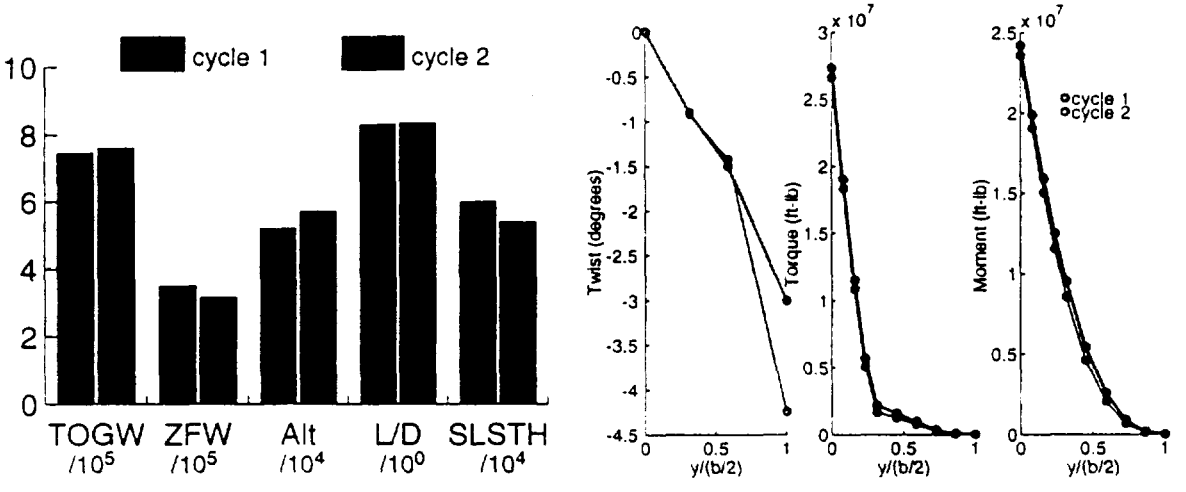

Figure 7.5: Cycles 1 and 2 aircraft target values

the new one selected by the system level optimizer is shown in Figure 7.5.[2] The associated discipline and system-level objective functions are:

J^*	J_a^*	J_m^*	J_s^*
8.34	8.70×10^{-6}	4.84×10^{-5}	6.86×10^{-4}

Subproblem discrepancy reduction was emphasized in this initial cycle, as the $TOGW$ actually rises slightly, while the penalty function $K(J_a^* + J_m^* + J_s^*)$ decreases.

This result is based upon the information provided to the system-level optimizer by response surfaces fits of the disciplines. As explained in Section 2.3.3, it is necessary to

[2] Numerical values of all target variables for each optimization cycle are compiled in Appendix B.2.

verify this new point and to determine the *actual* subproblem and system-level objective values. The corresponding subproblem predicted and verified objective functions for this new design appear as follows, along with the cycle 1 value for comparison:

	Cycle 1	Cycle 2 (Predicted)	Cycle 2 (Verified)
$TOGW$ (lb)	745 000	759 387	759 387
J_a^*	1.09	8.70×10^{-6}	8.70×10^{-6}
J_m^*	2.3×10^{-9}	4.84×10^{-5}	8.92×10^{-2}
J_s^*	3.9×10^{-4}	6.86×10^{-4}	9.2×10^{-2}
J^*	1089	8.34	189.55

The updated $TOGW$ is used to compute the actual system objective. The verified new J^*, at 189.55, is higher than the predicted value of 8.34 due to the non-quadratic nature of the structures and mission design spaces being imperfectly represented by the quadratic response surfaces used in the system level optimization. The predicted point for cycle 2 is acceptable however, as the verified new J^* is an improvement over the cycle 1 system-level objective function value of 1089. The subproblem results leading to the improved system-level objective are shown in Figure 7.6. A new trust region is defined, centered on the

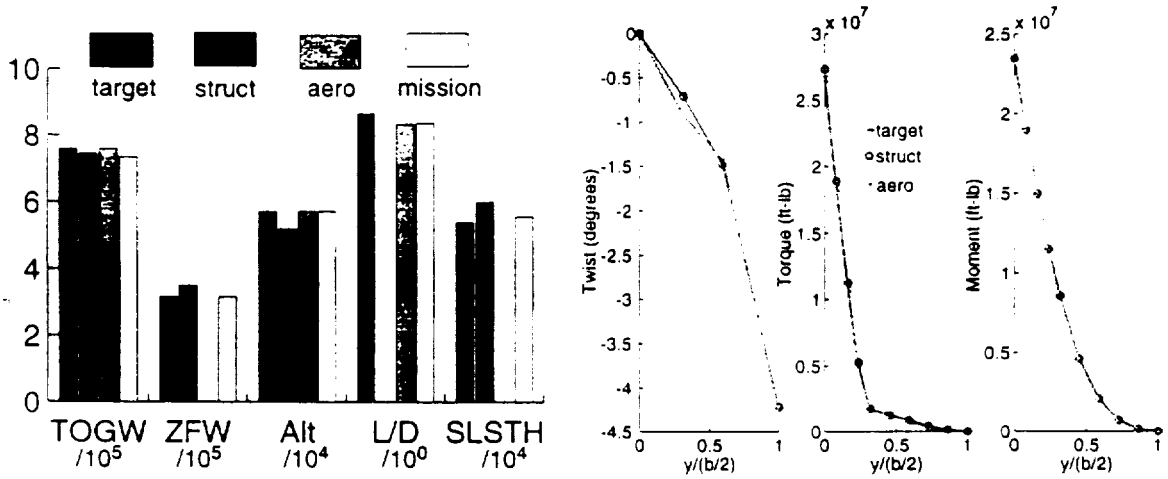

Figure 7.6: Disciplinary results: Cycle 2

cycle 2 design. Figure 7.7 depicts aircraft target designs within the new trust region. The previous trust region and associated target designs are shaded lightly. According to the algorithm in Section 2.3.3, as no new system-level design variables are at the previous trust

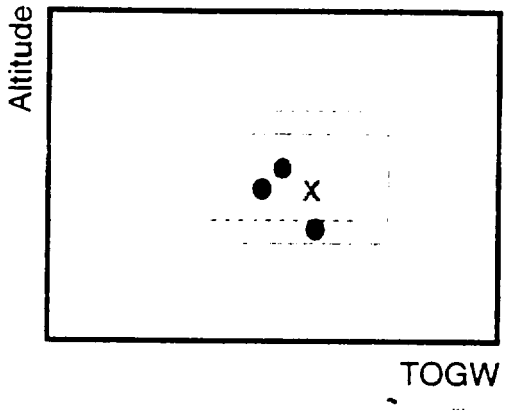

Figure 7.7: Cycle 2 trust region, centered on the new design (X). Also indicated are additional design points selected for response surface creation.

region bounds, the trust region merely translates, unchanged in size.

As in cycle 1, the system-level optimizer, given the response surfaces developed from subproblem results of the new target aircraft in Figure 7.7, is able to minimize its objective function within the current trust region. The new design, along with the previous two (for comparison) is shown in Figure 7.8. There are reductions in $TOGW$, $\{F\}$, $\{T\}$ and ZFW, and increases in L/D, altitude and $\{\delta\}$.

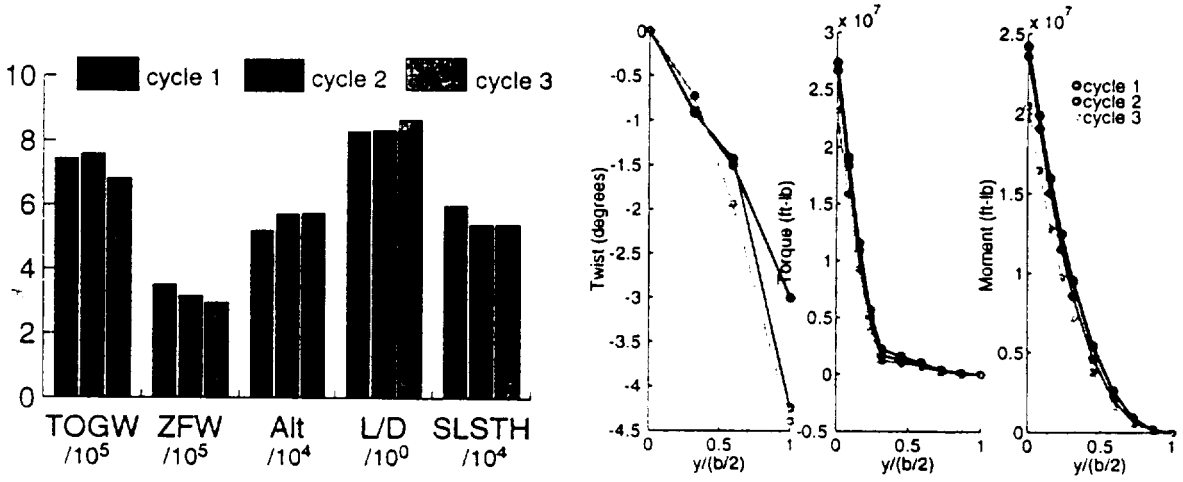

Figure 7.8: Cycle 1, 2, and 3 aircraft values

The cycle 3 predicted and verified subproblem and system objective function values are:

	Cycle 2	Cycle 3 (Predicted)	Cycle 3 (verified)
TOGW (lb)	759 387	681 630	681 630
J_a^*	8.68×10^{-6}	1.04×10^{-4}	1.04×10^{-4}
J_m^*	8.92×10^{-2}	1.22×10^{-4}	7.94×10^{-11}
J_s^*	9.28×10^{-2}	2.70×10^{-3}	7.23×10^{-3}
J^*	189.55	9.74	14.19

Subproblem discrepancy values were allowed to rise over those of the previous cycle. Though the penalty function of 1000 in Equation 7.2 is unchanged, the system-level optimizer emphasized a reduction in *TOGW*, resulting in a lower overall objective. The verified system objective of 14.19 is an improvement over the cycle 2 design. The subproblem results for the new cycle 3 baseline are shown in Figure 7.9 along with the target variables.

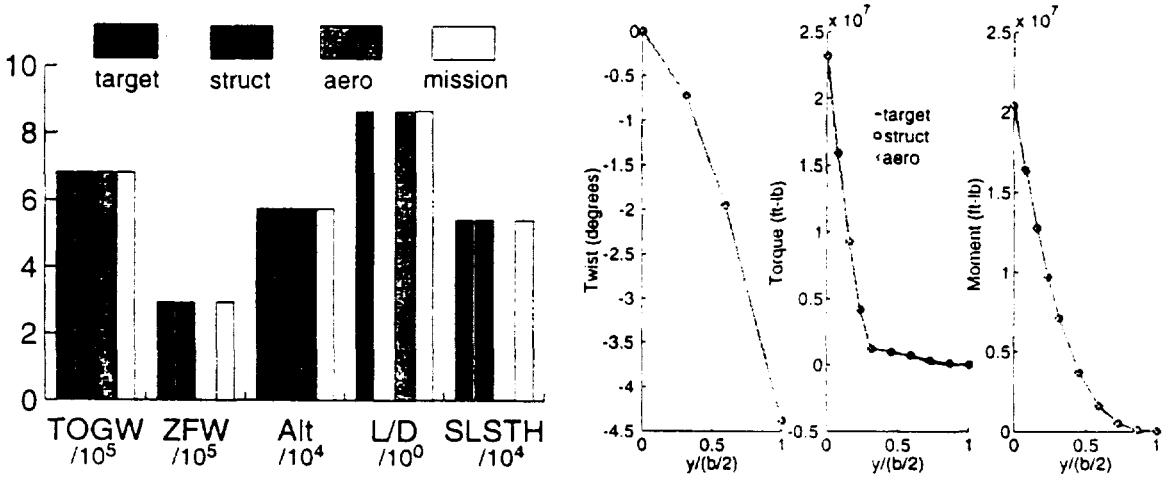

Figure 7.9: Disciplinary results: Cycle 3

Of course a new trust region must be defined, points selected, and response surfaces created. The cycle 3 center point *TOGW* of 681 630 *lb* lies on the lower bound of the cycle 2 trust region. The trust region algorithm states that the trust region should then *grow* in the TOGW dimension. This growth is depicted in Figure 7.10, along with previous trust regions and associated designs (retained in the background for comparison).

Using the new response surfaces centered around the cycle 3 design, a new aircraft is found by the system-level optimizer which is a further improvement:

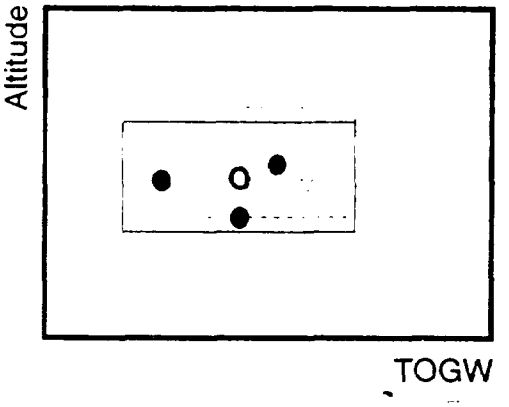

Figure 7.10: Cycle 3 trust region

J^*	J_a^*	J_m^*	J_s^*
10.03	5.59×10^{-4}	5.81×10^{-5}	2.79×10^{-3}

This time, the reduction is both in *TOGW* and in the penalty function portions of J^*. Design verification is successful, and the new design is accepted.

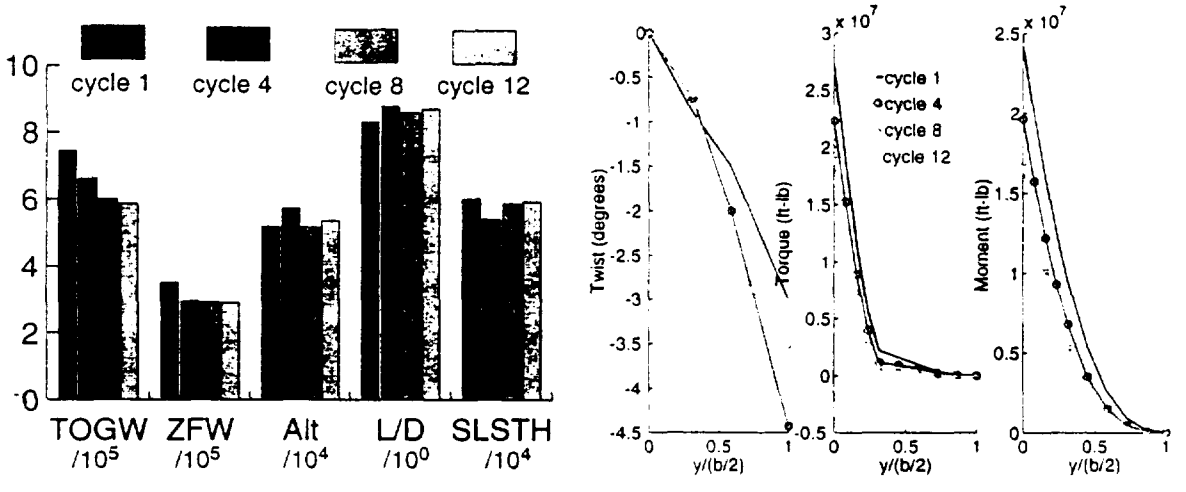

Figure 7.11: Cumulative cycle aircraft target values: spanwise distributions

This process repeats until a global optimum is found. If, in any cycle, a new design point does not lead to an improvement in J^*, the trust region is reduced in size and the previous cycle is repeated. At the global optimum design, the trust region will continue to shrink until it is within the acceptable tolerance for each variable. For this design the *TOGW* tolerance is 100 lb. This aircraft optimization converged in 12 cycles with a 159 100 lb

reduction in $TOGW$. No further improvement in J^* could be found within the trust region surrounding this design. The design variable progression from the initial to the final cycle is shown graphically in Figure 7.11. For clarity, only cycles 1, 4, 8 and 12 are shown.

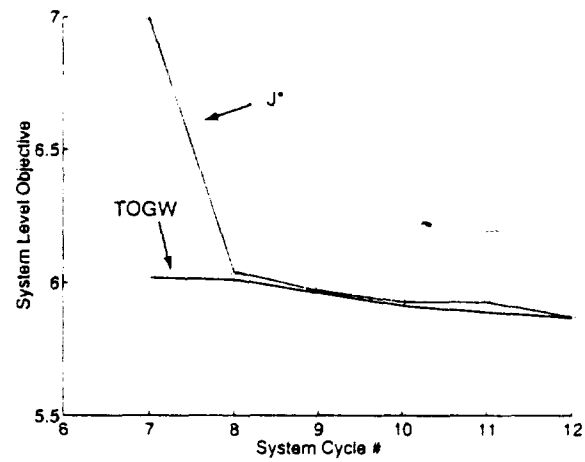

Figure 7.12: System-level objective progression

The progression of J^* with system-level cycle appears in Figure 7.12.[3] It is interesting to note that after the rise in $TOGW$ between cycles 1 and 2, in which the optimizer emphasized inter-disciplinary compatibility, the aircraft weight dropped steadily and quickly through cycle 6, a decrease of 158 000 pounds in 4 cycles. The ZFW drops as well, but only by 24 000 pounds. After cycle 6, the $TOGW$ continues to drop, but in much smaller increments while the ZFW oscillates before dropping again in the final cycles. Cycle 6 is the point at which the *Range* constraint becomes active, in that for some design within the trust region, the design is range-limited. Plots of *Range* and $TOGW$ with each cycle is shown in Figure 7.13. In the later cycles, there is no major design change, rather $TOGW$ decreases slowly and only small changes in other variables are seen. This continued $TOGW$ reduction is accompanied by a rising L/D and decreasing loads.

The aerodynamics and structures optimizers each use local design variables to perform their subproblem optimizations; that is, variables not directly affecting other disciplines. Figure 7.14 displays the optimal cruise and maneuver angles of attack (α_{cr}, α_{man}) selected

[3] Numerical values of system and subproblem objective functions for each optimization cycle are compiled in Appendix B.1.

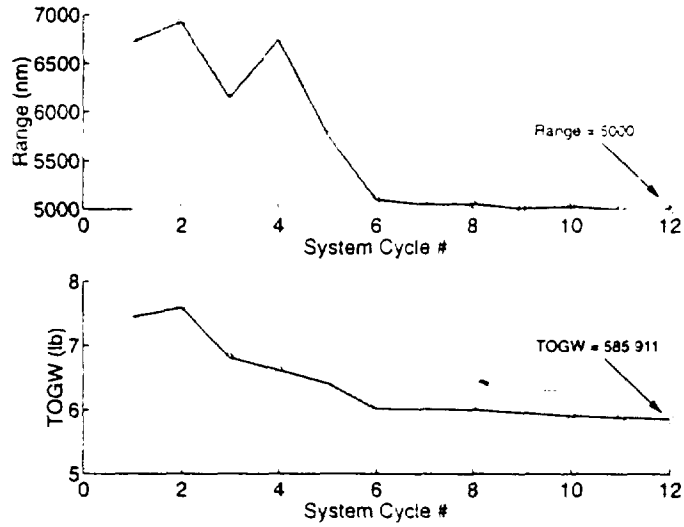

Figure 7.13: HSCT: Range and TOGW progression

by the aerodynamics subproblem optimizer in each cycle.[4] Corresponding to the *TOGW* progression, which is manifested as take-off lift generated in the aerodynamics analysis, the α_{cr} and α_{man} values decrease quickly and considerably over the first six cycles, after which the progress levels off. α_{cr} increases slightly over the later cycles to corresponding to the rising target L/D. The initial and final upper surface pressures computed by the aerodynamics analysis can be compared in Figure 7.15. There is not a major change, as the only variables directly affecting this result are the structural deflections and the angles of attack. The optimizer did soften the pressure peak at the leading edge of the spanwise wing break.

Properties of the structural model are shown for the initial and final designs in Figures 7.16 and 7.17. Figure 7.16 shows that the final z deflections are slightly greater than the initial as is the resulting twist. The top skin stress ratio $\left(\frac{\sigma}{\sigma_{max}}\right)$ appears in Figure 7.17. The high stress area is between the midchord and trailing edge on the inboard portion of the wing. However, the wing is not maximally stressed, as there is an aerodynamic advantage to a wing designed with a twist distribution that requires the addition of extra material to the model for deflection target matching.

[4]Recall the structural deflections corresponding to the maneuver flight condition are 2.5 g deflections, while those corresponding to the cruise condition are 1.0 g deflections.

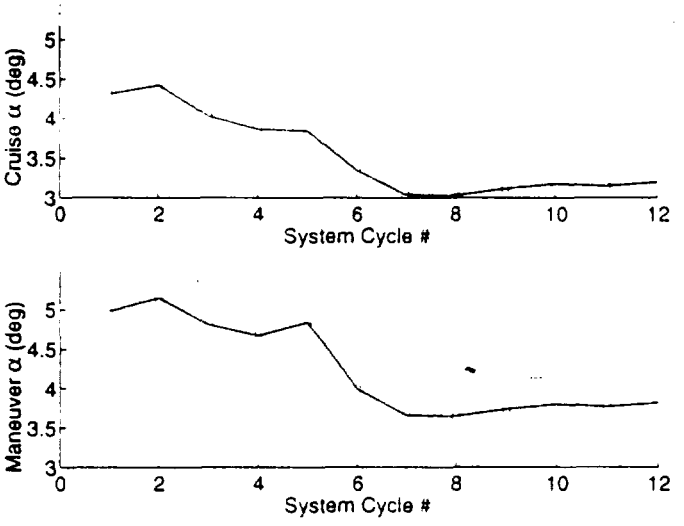

Figure 7.14: HSCT: Angle of attack progression

The cycle 12 aircraft in Figure 7.11 is the design corresponding to the lowest system-level objective function, J^*. At this converged solution, shown in more detail in Appendix B.2, neither the D/T nor the $TOFL$ constraint is active. The D/T is less than the maximum allowable value of 95%, and the $TOFL$ is well under the required 12 000 ft. This means that the engine is larger in thrust, size, and weight, than the minimum required by the mission subproblem. As $SLSTH$ is proportional to propulsion weight (and contributes to ZFW) in the structures discipline, it was expected that the structural analysis would drive the $SLSTH$ down to the minimum required value. The reason for the over-sized engine seems to be that the engine loads applied to the structural model were used to alter the structural twist distribution. For this design problem, as explained in Section 4.6, there is no chordwise variation in the finite-element thicknesses, and jig twist is not included in the design, so the only design variables that directly affect the twist are aerodynamic loads, and $SLSTH$. The oversized engines may reflect insufficient degrees of freedom in the structures or aerodynamics disciplines.

In the optimization described in the following sections, two local structural design variables are added. As described in Section 4.6, these variables permit changes in chordwise thickness distribution of the spars in addition to the existing spanwise thickness distributions of the spars and skin. These additions should permit further tailoring of structural twist.

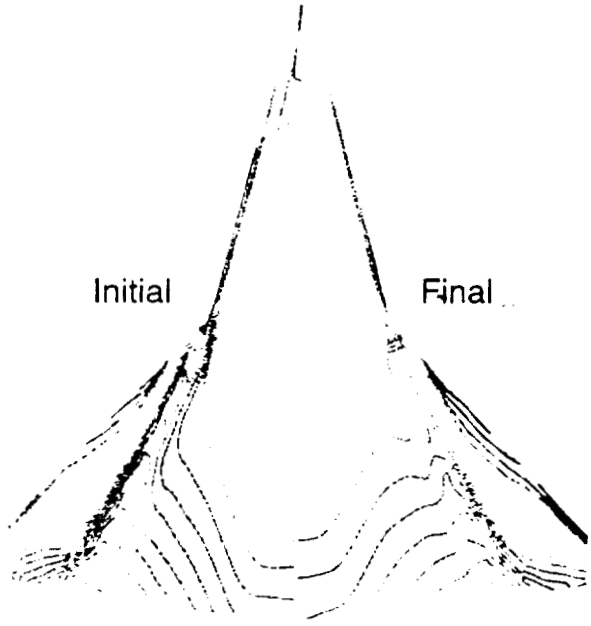

Figure 7.15: HSCT: Initial and final surface pressures

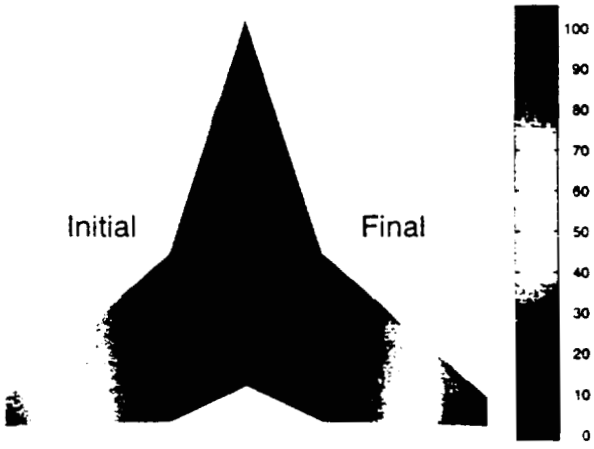

Figure 7.16: HSCT: Initial and final z deflections

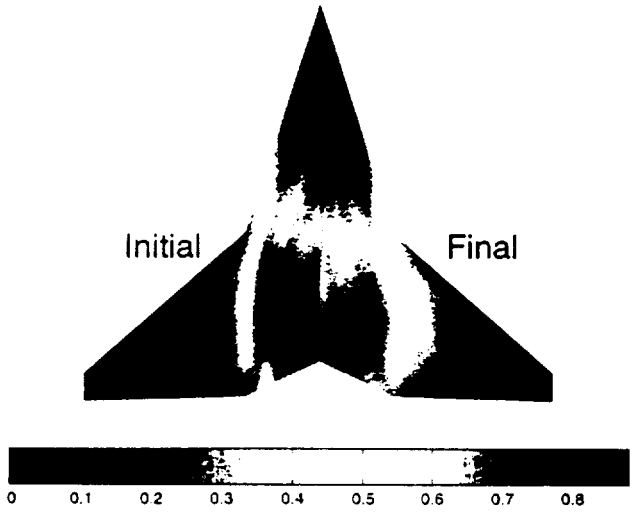

Figure 7.17: HSCT: Initial and final stress ratios: Upper surface skin.

7.4 Supersonic Natural Laminar Flow Aircraft Optimization

Supersonic NLF baseline design variables			
Variable	*Value*	*Variable*	*Value*
TOGW (lb)	535 000	Initial cruise altitude (ft)	50 000
ZFW (lb)	247 000	SLSTH (lb)	50 000
L/D	8.00		
F_1 (lb)	20 000	T_1 (ft-lb)	-8.0×10^6
F_2 (lb)	10 000	T_2 (ft-lb)	-3.3×10^6
F_3 (lb)	20 000	T_3 (ft-lb)	-2.0×10^6
F_4 (lb)	10 000	T_4 (ft-lb)	-3.0×10^5

The baseline natural laminar flow aircraft, for which the system-level design variables are listed above, is also a fixed-planform design (See Figure 1.16 for planform dimensions). In order to reduce the $TOGW$, the optimizer should select the most efficient aircraft, thus a design with the highest L/D subject to the various constraints. In the aerodynamics discipline, L/D increases result in part from a reduction in drag. Wave drag and skin friction drag each depend largely on the aircraft surface geometry. It was shown in Chapter 1 that skin friction drag is a large percentage of the total supersonic cruise drag for a turbulent aircraft. For this reason, it is expected that the optimizer will discover the sensitivity of boundary layer transition, in the form of reduced drag, to some design variables. The lack of planform and fuselage design capability limits the degrees of freedom available to the system-level optimizer for drag reduction, however other aspects of this approach make it a promising example of supersonic natural laminar flow design. Unlike the HSCT aircraft, a fuselage is explicitly modeled in the aerodynamics analysis and simulated in structures via boundary conditions as discussed in Section 4.3. Additionally, the viscous drag computation is handled by the boundary layer analysis introduced in Section 3.5, including transition prediction. The design in this case will not be fully aeroelastic. The aerodynamic loads remain as system-level variables to allow for structural sizing of the wing, but structural deflections induced by said loads are not passed to the system and on to the aerodynamics subproblem optimization. Thus the aerodynamics analysis will consider the wing rigid, and will build in jig twist to tailor the wing loads ($\{F\} and \{T\}$) and L/D.

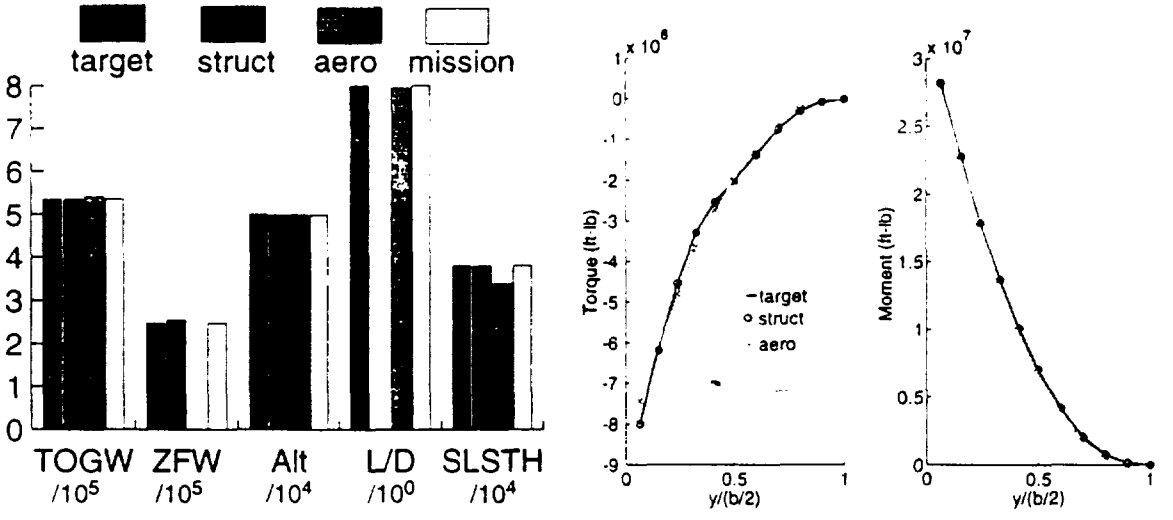

Figure 7.18: Supersonic NLF disciplinary results: Cycle 1

In presenting the results of the conventional HSCT, the emphasis was on the collaborative process. This section stresses additional CO implementation and result details. Design aspects which are important are the accuracy of the aerodynamics response surface, and analysis of trust region sizing. The system goal is again to design a 250 passenger, 5000 nautical mile range aircraft of minimum weight. The optimization process via the collaborative method is identical to that described for the previous aircraft. Disciplinary results, in their attempt to match the initial targets are displayed with the targets in Figure 7.18[5] The discipline and system-level objective functions for cycle 1 are:

J^*	J_a^*	J_m^*	J_s^*
193	0.18	9.41×10^{-10}	5.00×10^{-3}

Aerodynamics contributed more than the other disciplines to the system-level objective of 193, due greatly to the fact that there is a poor match of the target L/D while trying to lower the wing incidence to match the target $TOGW$. For this reason, the $TOGW$ computed by the aerodynamics discipline is higher than the target $TOGW$ and lower than the target L/D. Aerodynamics would have computed more favorable objective if a lower target $SLSTH$ had been selected, as $SLSTH$ sizes the engine and contributes friction drag. The structures subproblem failed to match the target ZFW, the reason the structures

[5] Numerical values of all target variables and disciplinary results for each optimization cycle are compiled in Appendix C.3.

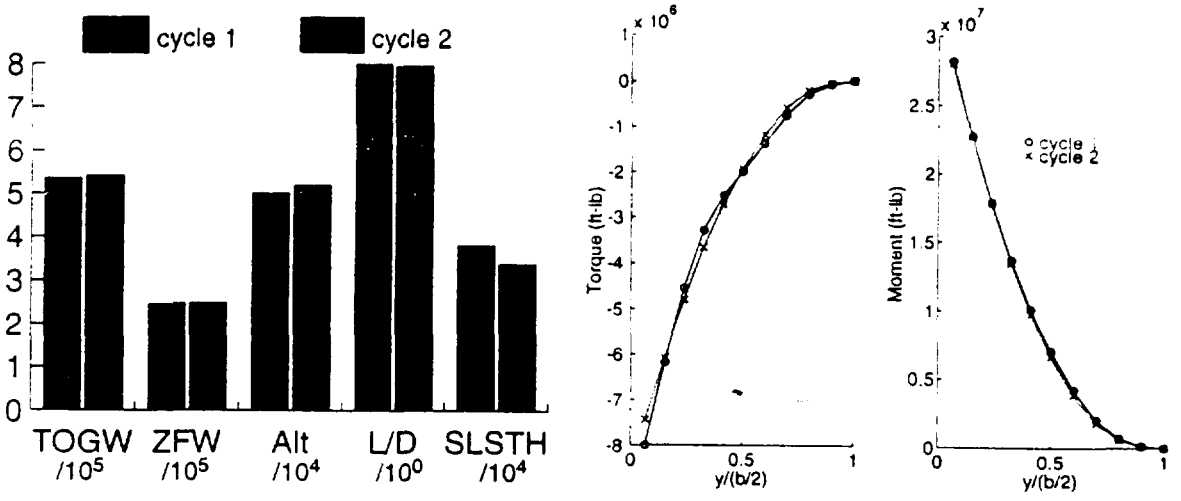

Figure 7.19: Cycles 1 and 2 aircraft target values

discipline $SLSTH$ result is low, as propulsion system weight is proportional to $SLSTH$ and contributes to ZFW.

The system-level optimizer, operating on the cycle 1 response surfaces and within the initial trust region, predicts a new point as shown in Figure 7.19. As in the HSCT optimization problem, the aircraft gross weight increases in this first cycle, as the system level optimizer emphasizes improved compatibility between the disciplines. The system and subproblem predicted and verified objective function values for the baseline and cycle 2 aircraft are:

	Cycle 1	Cycle 2 (Predicted)	Cycle 2 (Verified)
$TOGW$ (lb)	535 000	541 168	541 168
J_a^*	0.18	2.65×10^{-4}	2.65×10^{-4}
J_m^*	2.3×10^{-9}	4.17×10^{-4}	2.09×10^{-12}
J_s^*	3.9×10^{-4}	2.58×10^{-3}	2.83×10^{-4}
J^*	193	6.351	6.047

$SLSTH$ decreased from cycle 1 to cycle 2 as it is proportional to drag and weight in the aerodynamics and structures disciplines respectively. The lower bound in $SLSTH$ is dictated for the system by the mission subproblem, as there must be sufficient thrust to meet the $TOFL$ requirement and the climb constraint (D/T). These two constraints are much closer to becoming active in the second cycle. In this case, range remained essentially

the same, as neither L/D nor the available fuel changed appreciably:

Supersonic NLF Performance Constraint Values		
Variable	Cycle 1	Cycle 2
Range (n.mi.)	5118	5117
D/T	0.794	0.937
$TOFL$ (ft)	9198	10 664
LFL (ft)	5483	5515

In each cycle, the aerodynamics analysis response surface is by definition perfectly quadratic, therefore the predicted and verified values of J_2^* for the updated design match exactly. Thus it is necessary to ensure that the aerodynamics response surface, given the design variables selected by the subproblem optimizer to match the system-level targets, is an accurate prediction of the analysis. In Section 6.5.3, we saw that the aerodynamics response surface is a fine predictor in 2-D slices of the design space *if* there is no extrapolation beyond the fitted aerodynamics design space. Is this accuracy upheld when all aerodynamics design variables, in this case α_{cr}, α_{man}, $SLSTH$ and jig twist, are perturbed? The center, or base design variables of the current aerodynamics response surface appear below, along with the design variable values corresponding to the aerodynamics optimization of Cycle 2.

Aerodynamics Response Surface Fitness		
Variable (degrees)	RS center point	RS Cycle Solution
α_{cr}	2.5	1.18
α_{man}	2.5	1.09
θ_1	0.0	1.49
θ_2	0.0	2.96
θ_3	0.0	-0.03
$SLSTH$	38 000	33 792
Altitude	52 000	51 057

Most design variables have moved quite far from the base point. In this case, about a ± 1 degree (and $\pm 10\,000$ lb) perturbation was used to create the response surface. The response surface and *actual* analysis results given these inputs appear in Figure 7.20, indicating that the aerodynamics response surface is a fine predictor of the analysis. The next step is to run

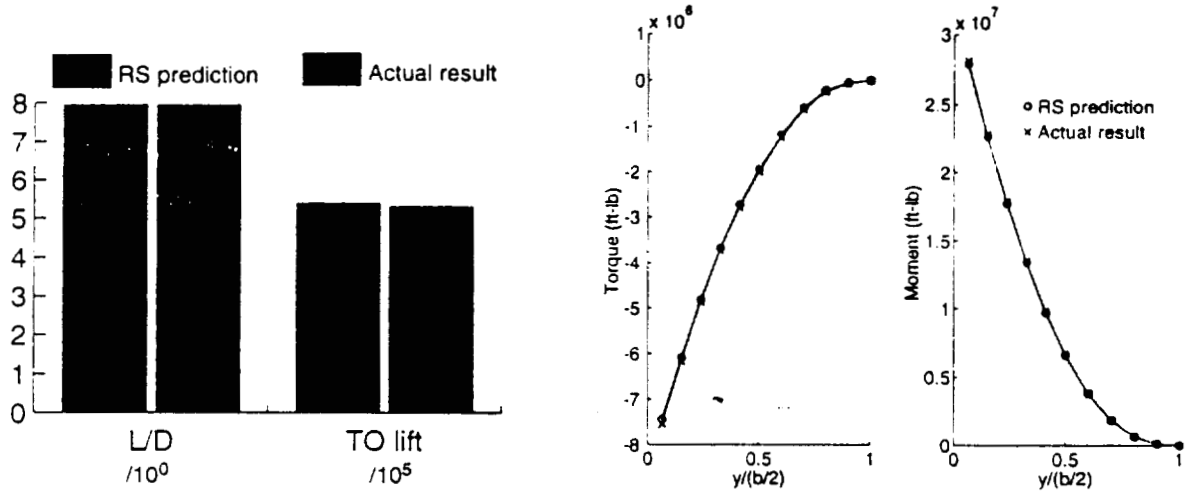

Figure 7.20: Aerodynamics response surface fitness: Cycle 2

a *new* aerodynamics response surface centered on the current cycle solution design variable values. This fit update process is repeated each cycle, and it turns out that this level of accuracy is the norm, and the response surface substitution of the analysis introduces minimal loss of accuracy, while greatly decreasing expense and frustration. The collaborative

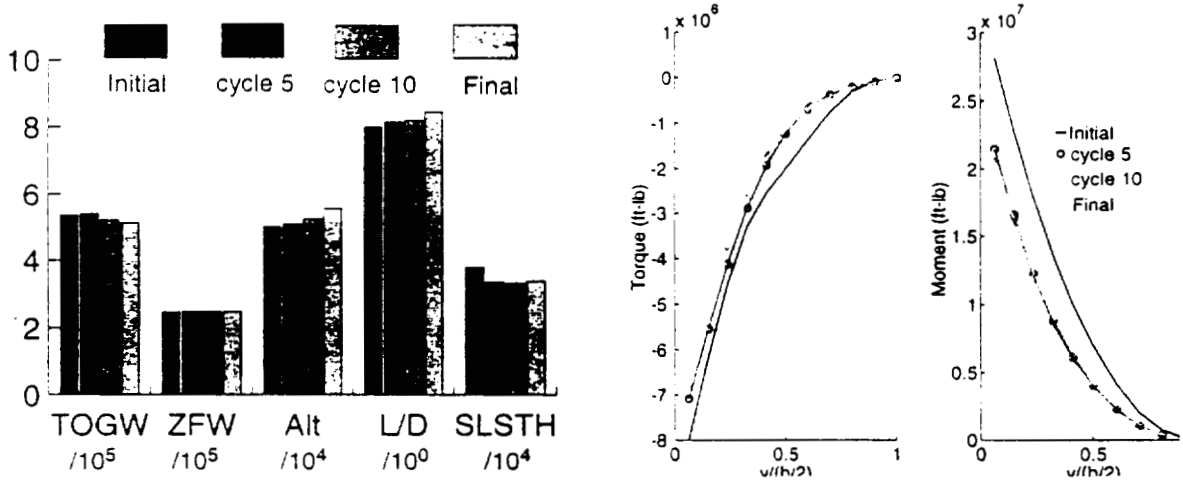

Figure 7.21: Aircraft target value progression

optimization process is followed as described in Sections 2.3.3 and 7.3 until no further cycle improvement can be found. This optimization converged in 17 cycles. The design variables for cycles 1, 5, 10 and 17 are displayed graphically in Figure 7.21. Overall, the system

managed a 4.4% weight decrease.

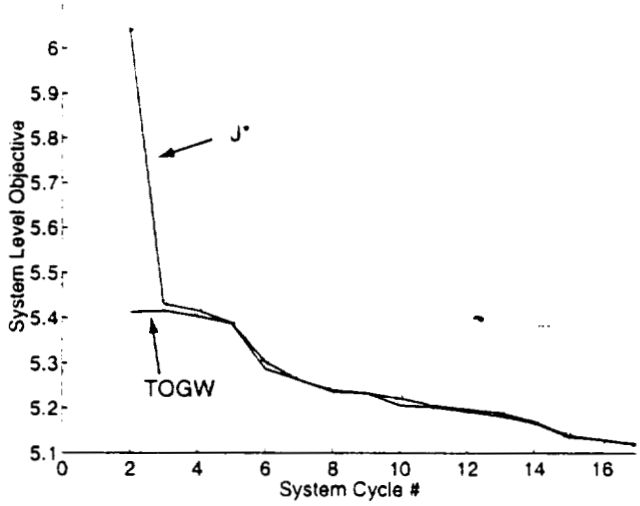

Figure 7.22: System-level objective progression

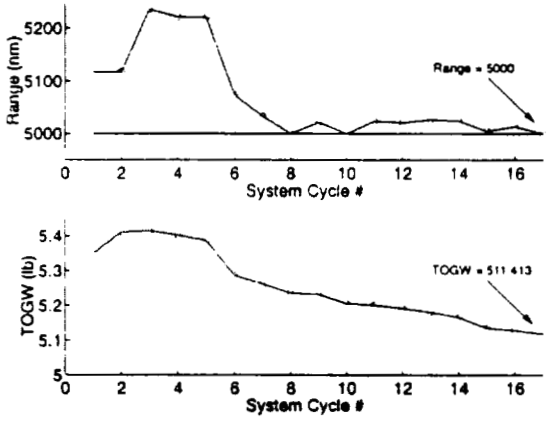

Figure 7.23: NLF: Range and TOGW progression

Figures 7.22 and 7.24 show progression of the system objective and the aircraft variables and constraints. [6]

As stated, the optimizer raised both $TOGW$ and ZFW in cycle 2, lowering J^* by improving inter-disciplinary compatibility. There is another, smaller, $TOGW$ increase in cycle 3. In subsequent cycles, both weights steadily decrease. The range constraint becomes

[6] Numerical values of system and subproblem objective functions for each optimization cycle are compiled in Appendix C.1.

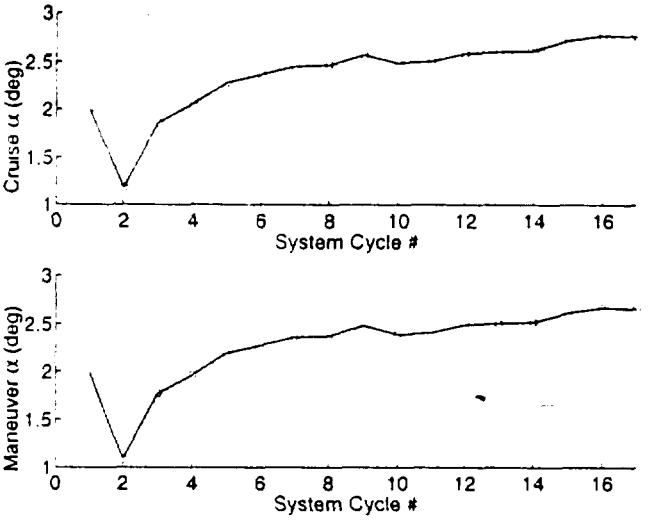

Figure 7.24: NLF: Angle of attack progression

active at cycle 7. When this occurs, the optimizer performs subtle design changes by testing design variable interaction. In this case the weight loss is achieved by increasing L/D (for mission to require less fuel to fly 5000 n.mi.), keeping $SLSTH$ low (to allow aerodynamics to improve L/D), and decreasing moment and torque (to reduce structural load thus ZFW). This is accomplished without violating structural integrity or mission constraints.

The local aerodynamics variables, α_{cr} and α_{man}, shown in Figure 7.24, in cycle 2 considerably drop from their initial values. The aerodynamics analysis, in its initial configuration, was generating much more lift than that requested by the system-level optimizer. To reduce

Figure 7.25: NLF: Initial and final surface pressures

the supplied lift, the angles of attack were lowered, which diminished L/D. Thus, as can be seen in Appendix C, in cycle 1 aerodynamics produced a $TOGW$ higher than the target, and an L/D considerably lower. $SLSTH$ was lower than its target in an attempt to help L/D, and the aerodynamic loads are generally lower than their targets, though the match in loads was quite good. This contribution to the aerodynamics J_1^* led to the cycle 2 $TOGW$ increase and lower L/D and $SLSTH$.

The initial and final wing surface pressures are displayed in Figure 7.25. Though modeled in aerodynamics with a fuselage, only the wing pressures are shown here. As in the conventional HSCT case, there are only small changes in the pressure contours. The optimizer smoothed the leading edge pressures. The effect of the fuselage and the wing tip can been seen in this figure as the Mach cones create disturbances in the isobars.

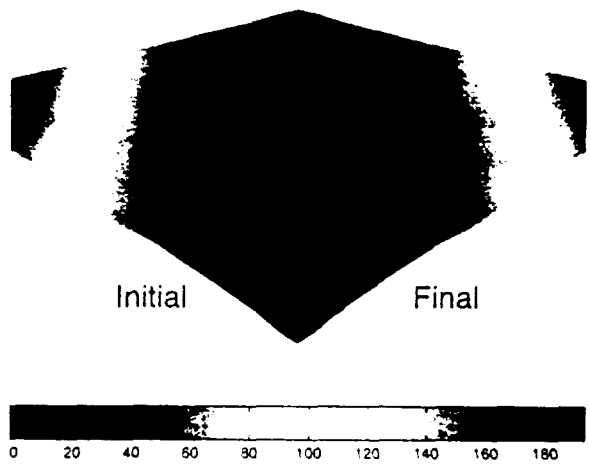

Figure 7.26: NLF: Initial and final z deflections

Figures 7.26 and 7.27 display optimization structural results graphically. The initial and final surface deflections can be seen in Figure 7.26. The tip deflection and twist are less than their initial values in the final design, but decreased largely in the early cycles and changed little after cycle 5. Figure 7.27 shows the ratio of top-skin stress to maximum allowable stress for the initial and final designs. In this NLF aircraft design, once the aerodynamic loads are matched by the structures subproblem, the deflections are limited only by the stress. In this design, the maximum skin stress was about 95 % of the maximum allowable in each cycle, and inboard root spar elements are fully stressed. The ribs, as expected, remain at minimum gauge thickness.

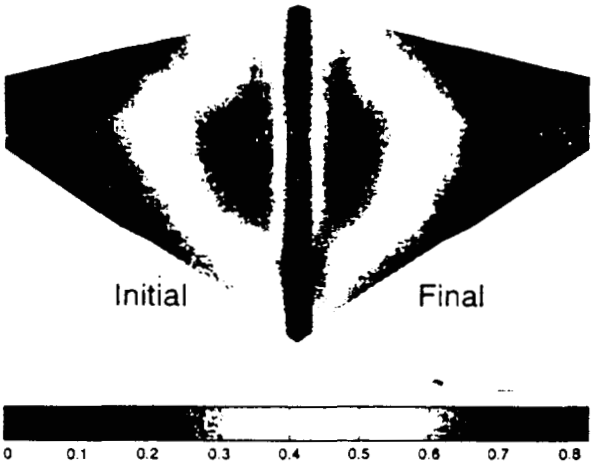

Figure 7.27: NLF: Initial and final stress ratios: Upper surface skin.

The change in design, even without free planform or fuselage variables, enabled an increase in maximum laminar flow fraction on the NLF wing, from 50% to 55% chord.

Chapter 8

Conclusions and Future Direction

8.1 Large-Scale Design with Collaborative Optimization

Large-scale implementation of collaborative optimization with response surface estimation is complex. Successfully integrating industry codes for analysis of structures [54], inviscid aerodynamics [18], and viscous aerodynamics [12] into their respective subproblems was not uneventful. Selection of auxiliary analysis calculations such as propulsion, performance (Chapter 5), component drag (Chapter 3), aircraft weights (Chapter 4), and development of reduced basis modeling techniques (Chapter 6) for system level variable reduction were also involved processes.

The importance of accurate modeling techniques became clear when the first attempts at large-scale implementation of the method stalled after few cycles. [71,74] Insufficient fits of aerodynamic loading led the structures discipline to extract incorrect force distributions from the system level design variables. This problem, which hinders aeroelastic convergence, prompted the analysis in Section 6.4 and a complete overhaul of the fitting approaches.

Inconsistent aerodynamics subproblem convergence and other difficulties encountered by the gradient-based optimizer NPSOL revealed poor gradient information from the higher-order surface panel method A502 using finite differencing. In fact, although developed for industry use, A502 does not compute results to the precision required for gradient-based optimization. After some attempts to increase the code precision, the gradient problem was improved, but not eliminated. For this reason the entire aerodynamics analysis is fit with a series of response surface fits over the optimization cycle trust region. As the aerodynamics analysis is a combination of a surface panel method, a finite-difference boundary layer code,

and auxiliary calculations, each computed value passed to the subproblem optimizer was fit separately, for a total of 11 fits. This solution lead to smooth gradients and reduced computation time in the aerodynamics discipline.

Upon resolution of these implementation problems, the application of collaborative optimization to a conventional HSCT design, as described in Section 7.3 was successfully performed. The second successful optimization minimized the *TOGW* of a natural laminar flow supersonic transport. The lack of planform and fuselage design capability limits the degrees of freedom available to the system level optimizer for drag reduction, however other aspects of this approach make it a promising example of supersonic natural laminar flow design. The fixed-planform NLF application converged in 17 system level cycles, and incorporated analysis enhancements. The aerodynamics analysis paneled a fuselage into the surface geometry (for the conventional HSCT the drag, weight, and volume of the fuselage was computed from a set of parameters) and the boundary layer transition prediction introduced in Section 3.5 was applied to compute the transition due to streamwise and crossflow boundary layer effects.

8.2 Trust Region Update Algorithm and Response Surface Fits

The trust region algorithm is described in Sections 2.3.2 and 2.3.3.

This algorithm is the least well-developed aspect of the optimization architecture. Implementation for a large-scale design problem is more complex than for the smaller problems used to develop and verify the method initially. Previous problems solved using collaborative optimization, showing the accuracy of the method, often had the luxury of an analytic or exact solution with which to compare [13, 15, 71, 72]. Subsequent, more evolved designs were embedded with analyses inexpensive enough to minimize the inconvenience of slow convergence [71]. This is not the case for the large-scale designs of this research. Due to the now more expensive response surface creation process, a consequence of using more design variables with longer-running codes, a significant time penalty is incurred when a new point is not an improvement.

It is clear to the author that in order to efficiently solve large-scale problems with collaborative optimization, a more efficient trust region update algorithm is necessary. The update sequence is affected by absolute variable bounds, amount of change from the previous

system level point, movement of design variables to trust region bounds, and proximity to the global optimum. A good algorithm governs when, by how much, and in what directions to alter the trust region size.

The optimization subproblems developed in the current research include expensive analyses, and consist of more design variables and constraints than in previous problems solved with collaborative optimization. All of this means considerable expense in creating a response surface at each cycle. If a new design point is in fact not an improvement, a step backward is required to create a replacement response surface on a smaller trust region in an attempt to improve the fit. On these occasions, the author found herself relying on intimate familiarity of the entire optimization process *and* the details of each analysis to select the amount by which to increase or decrease trust region size when necessary. In the industry implementation of collaborative optimization, however, the system level controller may not know the details of each discipline. The fact that there need be no discussion of analysis details between disciplines or with the system level is one of the benefits of collaborative implementation of large-scale design problems. This localized knowledge can be a detriment, however, when determining ideal trust region sizes. A proper, well developed trust region update algorithm can maximize the chances of improvement in each cycle, as well as finding the most direct path to the optimum design. These features will reduce the number of cycles, thus the required number of response surface fits.

Using post-optimality gradient information, only O(n) points are required to generate a reasonable response surface (see Section 6.6) [13, 14]. This fact can introduce problems to an insufficient trust region update algorithm, two of which were experienced in the current work.

First, if a trust region is too large for accurate estimation by the quadratic response surfaces, the gradient $\frac{\partial J^*}{\partial z_i}$ in the dimension of a design variable may be quite big, discouraging the optimizer from moving in that direction. This could result in lack of system level improvement, necessitating trust region shrinking, or in only nominal improvement between cycles. Second, as only O(n) points are required, only one perturbation in each design variable from the center point is necessary to obtain enough linearly independent target sets to develop the response surface. Thus the fit within the trust region may contain information in only one direction from the base point for each variable, and no explicit cross-perturbation information. The perturbation direction, positive or negative, could degrade the accuracy of the result if the design space is not truly quadratic. This will also

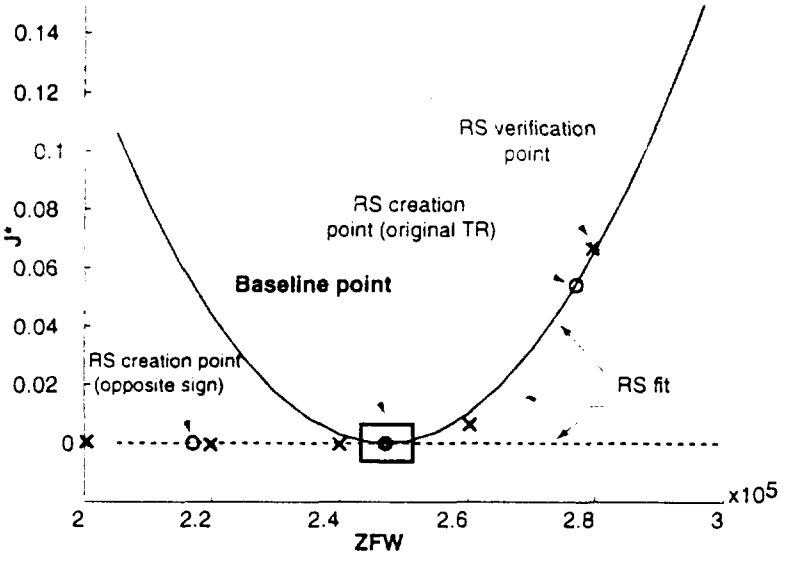

Figure 8.1: Effect of perturbation direction on mission subproblem response surface: J^* vs ZFW

lead to unnecessary extra cycles. In either case, an oversized trust region or an incorrectly spanned trust region, though the correct global solution can still be obtained, excess cycles will be required. In the case of true industry implementation, where a system level cycle may take days to complete, this is a problem which should be controlled.

For illustration, Figures 8.1 and 8.2 contain fits of the mission discrepancy value, J^*, with respect to L/D and ZFW. The baseline point design variables for these fits of the natural laminar flow aircraft are:

$TOGW$ (lb)	535 000
ZFW (lb)	247 000
Altitude (ft)	50 000
$\frac{L}{D}$	8.0
$SLSTH$ (lb)	38 000

In addition to the line representing the fits, symbols indicate points used to create the fit, and verification points.

The baseline target $TOGW$ and ZFW for the NLF aircraft are 535 000 lb and 247 000 lb respectively. The size of the trust region in the ZFW direction is 30 000 lb, and the perturbation direction has a huge impact on the mission $\frac{\partial J^*_m}{\partial ZFW}$. In Figure 8.1, response

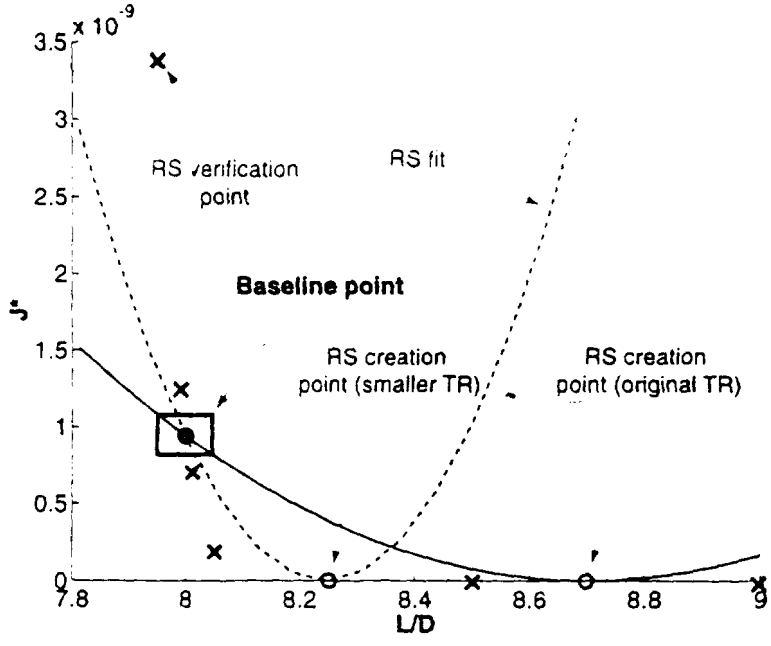

Figure 8.2: Effect of trust region size on mission subproblem RS: J^* vs $\frac{L}{D}$

surface fits are plotted using points from each perturbation direction. The baseline aircraft has about 280 000 lb of fuel. For a positive perturbation in ZFW, to 277 000 lb, mission evaluates an aircraft with about 250 000 lb of fuel, while for a negative perturbation, about 310 000 lb of fuel is available. The solid line represents the response surface created from the baseline point and the increased ZFW. This fit reflects the fact that the range constraint becomes active and drives up the objective function, however, does not have information to indicate improvement in J^* for lower ZFW values. If the negative perturbation were used, the dashed line is the result. The baseline J^* is low, the value for the perturbed ZFW is even closer to zero, and the response surface never captures the rise in J^* for larger ZFW. For this case, even within the trust region the response surface would be a poor indicator of performance. As the one-sided response surface is the only information the optimizer has to determine $\frac{\partial J^*_m}{\partial ZFW}$, it is clear that this gradient affects the system level solution. It is preferable to select the perturbation direction that most accurately represents the discipline design space, and will lead to active constraints. In this case that is the positive perturbation in ZFW.

In Figure 8.2 the baseline point is $L/D = 8$. The cycle 1 trust region for this aircraft was 0.7 $\frac{lb}{lb}$ in the L/D dimension, and the corresponding fit is indicated by the solid blue

line. The fit is not very accurate within the trust region, overpredicting the true mission J^*. This means that the the *actual* mission subproblem, when instructed to verify a new cycle's design, will return a better result (lower J_t^*) than predicted by the response surface. Shrinking the trust region to 0.25 $\frac{\Delta^2}{16}$ yields the fit depicted by the dashed line, and predicts more accurately the values within the trust region. However, this fit would be useless in extrapolation to higher L/D values. For reasons displayed in this plot, trust region extrapolation is never performed in this research, as any cycle-to-cycle improvement would likely be pure coincidence.

The above examples show that care must be taken to select representative trust region sizes and evaluation points within the defined space. The analysis and optimization development in this research was performed by an individual, someone familiar with all levels of interaction. This will not be that case in the industry implementation of collaborative optimization using response surface estimation. There may be leaders within each discipline knowledgable only of the subproblem analysis and optimization. The system level coordinator may not be at all exposed to discipline analysis details. The efficiency of the solution process may be helped if discipline level information affecting effective trust region sizing and selection of evaluation points for response surface creation is forwarded to the system level coordinator.

This discussion leads to a general issue with quadratic fits that affects response surface utility. Currently, at each cycle when a new response surface is created, the old information (from points evaluated for the previous fits), is discarded. It is preferable to retain old data in order to enhance current fits. This is especially true near the optimum, when the trust region moves less and it is more likely that the new region will overlap the old. A fitting procedure that uses all points lying within the current trust region to create the response surface would be beneficial.

8.3 Natural Laminar Flow Supersonic Commercial Aircraft Design

This work represents the first attempt at large-scale multidisciplinary optimization of a supersonic natural laminar flow aircraft. In recent years, however, two other supersonic NLF wing concepts have been proposed. A partial laminar flow wing design was analyzed in Reference [28]. This design was similar to the conventional HSCT planform, with the

outboard, supersonic leading edge portion of the wing swept only 20 degrees. Studies were performed to assess the affect of increasing the area of this outboard portion as well. Using a range of supersonic transition Reynolds numbers, the aircraft was optimized for minimum $TOGW$ subject to mission constraints. The aerodynamics analysis consisted of linear methods supplemented with experimental and empirical data, while the mission and weight calculations were performed by FLOPS [48]. No aeroelastic optimization was performed. Up to 91 percent laminar flow on the outboard portion of the wing vs predicted for a transition Reynolds number of 30 million [28].

Research at Northrop Corporation yielded a reverse-delta wing concept for natural laminar flow supersonic transports. The benefits of the reverse-delta are similar to those of the wing analyzed in this dissertation, such as favorable pressure gradient, and low-swept isobars for low crossflow [31], [32]. In fact, early in the analysis development for the work in this dissertation, the reverse delta concept was explored along with the trapezoidal wing ultimately selected for further research. In References 31 and 32, Euler calculations and wind tunnel tests suggested that flow over the reverse-delta wing is nominally 2-D. No optimization was performed.

8.3.1 Supersonic NLF Aircraft: Additional Design Variables

The conventional HSCT optimization demonstrated the ability of collaborative optimization to perform large-scale fully aeroelastic design using complex analyses. Convergence of the supersonic natural laminar flow aircraft design in Section 7.4 showed that the subproblem enhancements required for NLF optimization, such as boundary layer transition and a wing-body model could be successfully implemented. This optimization, however, was performed without several important geometry-related design variables. The design variable set limits the degrees of freedom available to the system-level optimizer for aggressive delay of boundary layer transition. The obvious next step is to introduce design variables that allow the optimizer to design the wing planform, thickness distribution, and wing-fuselage intersection. For the fixed-geometry NLF design problem, the optimizer sought to raise L/D consistently over the last 7 cycles, and did so by reducing $SLSTH$ as much as possible given the D/T constraint and by raising the initial cruise altitude. Addition of variables permitting the optimizer to increase the wing laminar flow fraction would lead to even higher L/D values thus lower necessary $TOGW$ and ZFW to meet the performance constraints. These geometry variables and their values for the fixed-planform NLF design

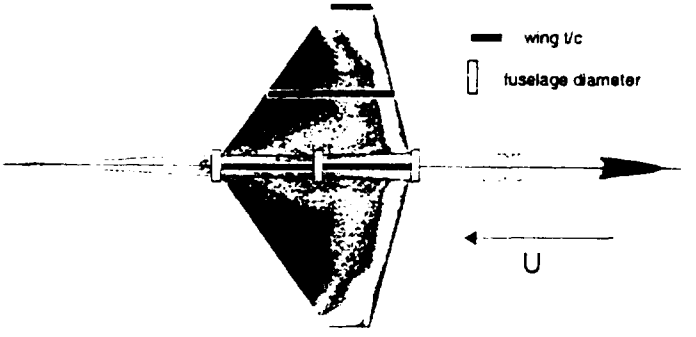

Figure 8.3: Location of NLF fuselage diameter and wing thickness design variables.

are [1]:

NLF additional design variables			
Variable	*Value*	*Variable*	*Value*
$S_w\ (ft^2)$	7675	$\frac{t}{c}_{root}$	0.0175
$b\ (ft)$	144	$\frac{t}{c}_{mid-span}$	0.0175
$\Lambda_{le}\ (deg)$	15	$\frac{t}{c}_{tip}$	0.0175
λ	0.2127	$fused_1\ (ft)$	12
		$fused_2\ (ft)$	10
		$fused_3\ (ft)$	9

Locations of the fuselage diameter and wing thickness variables are shown in Figure 8.3. The wing thickness varies linearly between these selected locations, while the fuselage diameter is a spline fit through the three stations shown in the figure.

The optimization starting point for the other design variables is the final design of the fixed-planform NLF case. In the first cycle with additional variables (cycle 18 overall), the objective function, J^*, improves to 5.107 from 5.129. The new geometry variables become:

[1] The fuselage diameters are defined at the x stations of the 1) wing leading edge root, 2) wing mid-chord 3) wing trailing edge root

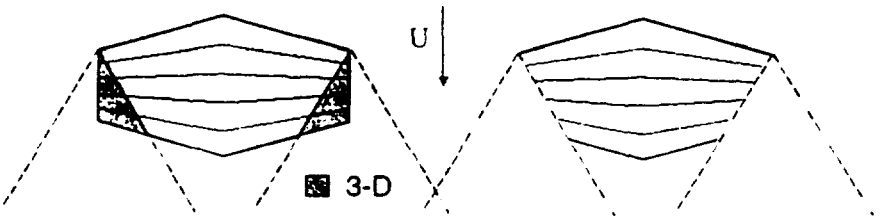

Figure 8.4: NLF wing planform concepts.

NLF additional design variables-cycle 18			
Variable	*Value*	*Variable*	*Value*
$S_w\ (ft^2)$	7744.29	$\frac{t}{c}_{root}$	0.0176
$b\ (ft)$	143.59	$\frac{t}{c}_{mid-span}$	0.0154
$\Lambda_{le}\ (deg)$	14.78	$\frac{t}{c}_{tip}$	0.0165
λ	0.2206	$fused_1\ (ft)$	11.73
		$fused_2\ (ft)$	11.00
		$fused_3\ (ft)$	9.12

with a reduction in $TOGW$ to 510 421 lb. It is apparent that the optimizer is attempting to reduce wave drag by decreasing mean fuselage diameter and t/c.

To date, three cycles are complete for this free-planform NLF aircraft. Changes in the wing pressure contours indicate that the optimizer is attempting to smooth the isobars and approach the near conical-flow distribution of the wing-only case (see Figure 1.11). It is recommended that this optimization problem run to convergence to test the ability of the system level optimizer to improve the efficiency of the aircraft.

When considering additional optimization design variables to provide the necessary degrees of freedom for aggressive natural laminar flow design, wing tip design should be investigated further. Analysis of several derivative trapezoidal planforms was performed early in this research. A trapezoidal NLF wing planform is shown on the left side of Figure 8.4. A derivative planform, seen on the right side of the figure, has wing tip edges raked along the Mach angle to avoid the influence of disturbances emanating from the leading edge tip. Computational results of local velocity and crossflow Reynolds number for the trapezoidal wing concept are shown in Figure 8.5. The 2-D linear theory result of local velocity at the same flight condition is shown for comparison. The trapezoidal wing exhibits all properties

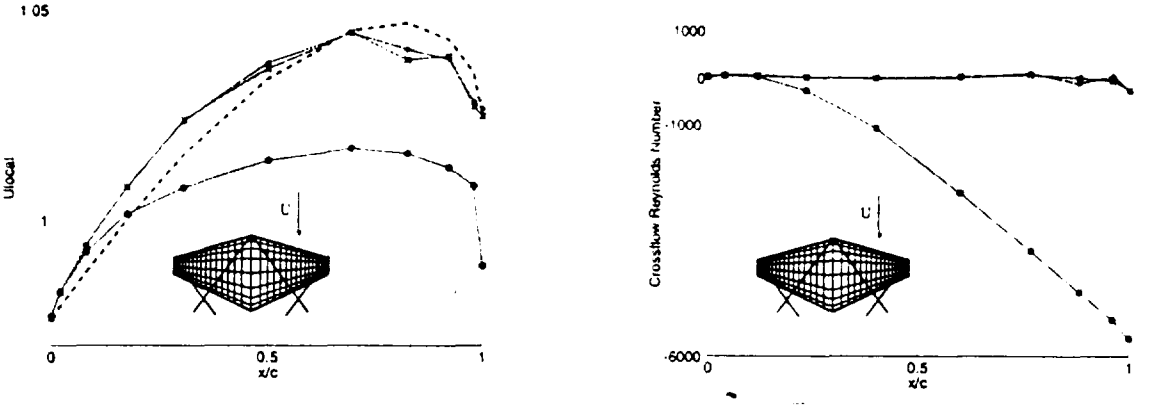

Figure 8.5: Local U velocity and crossflow Reynolds number on a trapezoidal wing.

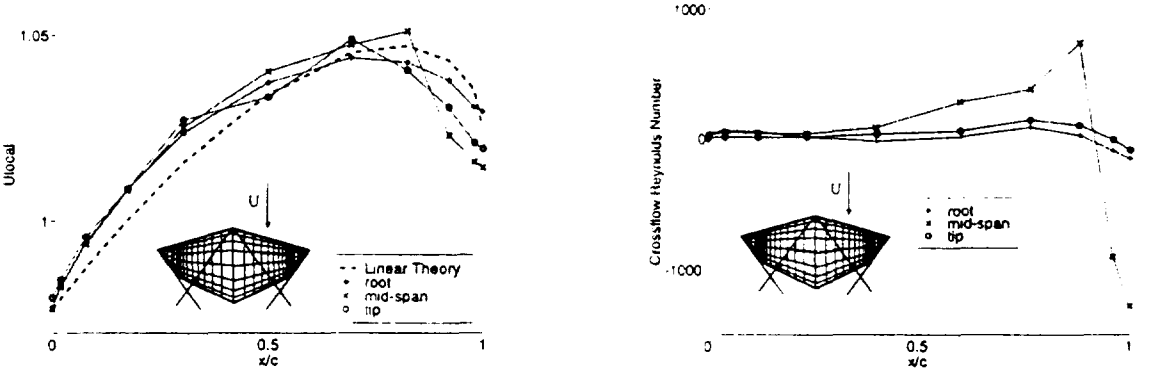

Figure 8.6: Local U velocity and crossflow Reynolds number on a trapezoidal wing with wing tips raked to the Mach angle.

of 2-D flow except near the wing tip, inside the zone of influence of the disturbances emanating from the wing leading edge. To reduce crossflow it is advantageous to design a wing that does not penetrate the tip mach cone zone of influence. Figure 8.6 shows the same results for the trapezoidal wing with the tips *raked* to the Mach angle. The local velocity is now close to the 2-D result all along the span, and the crossflow at the tip has been essentially eliminated. There is induced crossflow near the trailing edge of the tip, which is now raked inward, thus affecting the flow near the mid-span of the wing.

The aeroelastics, even static, are more challenging to analyze than for the conventional supersonic transport. Admittedly, one of the major benefits of large-scale design with collaborative optimization, the use of response surfaces, has difficulty with the aeroelastic coupling of the low-sweep configuration. That is, it is difficult to sufficiently represent

the design space with the quadratic fit methods employed here. Thus the proposal in Section 8.2 for development of new modeling methods that retain old information and that do not assume a quadratic subspace. Recommended new fitting functions include combining weighted mode shapes of the potential twist and load distributions, and the ability to retain existing information in future fits.

As stated in Chapter 1 there are many inhibitors to maintaining supersonic natural laminar flow over the majority of a wing surface, problems that need to be addressed before successful commercial flight. This work, though not discovering solutions to all forseen difficulties of NLF configuration development, sets in place the framework for performing the aircraft optimization. Collaborative optimization methodology allows for enhancement of any discipline analysis or incorporation of additional subproblems without necessitating an overhaul of the entire system framework. Thus design challenges such as aircraft trim during transonic acceleration, subsonic performance, dynamic aeroelastic response, and high-lift system development, among others, may be inexpensively incorporated into the existing system.

As this thesis is submitted, preparation for a natural laminar flow wing flight test is underway. A supersonic NLF wing model with a 3-foot root chord will be mounted to the underbody of a NASA F-15. Tests for natural laminar flow will be conducted using infrared photography to detect transition. The analyses and collaborative framework in this work is planned for use in helping to determine a wing-body combination for a future flight test.

8.4 Closing

Rohl [64] and Hoenlinger [56] indicate that industry feels as though sophisticated processes such as collaborative optimization are not yet fully proven or sufficiently matured. In some cases they are not suited to a given application, and in others complicated approaches are not easy to understand or follow. [64] Flexibility of a chosen multidisciplinary optimization method is necessary, as the optimization process must be tailored to each new problem. It is the author's hope that this work serves to show that collaborative optimization is, in fact, a valuable method for design that is ready for real-world implementation.

Bibliography

[1] High Speed Commercial Flight: The Coming Era. In J.P. Loomis, editor, *Proceedings of the First High Speed Commercial Flight Symposium*. Battelle Press, Oct 1987.

[2] *Aviation Week and Space Technology*, page 17, 2 Dec 1991.

[3] *Aviation Week and Space Technology*, page 62, 15 Jun 1998.

[4] "Growth Prospects Strong For Business Flying". *Aviation Week and Space Technology*, page 46, 19 Oct 1998.

[5] S. Agrawal and T. A. Kinard. "Supersonic Boundary-Layer Stability Analysis on an Aircraft Wing". *Journal of Aircraft*, 32:721–727, Nov 1991.

[6] N. Alexandrov and J.E. Dennis. "A Trust Region Framework for Managing the Use of Approximation Models in Optimization". NASA TM 112870, 1997.

[7] N.M. Alexandrov and S. Koldiyalam. "Initial Results of an MDO Method Evaluation Study". AIAA Paper 98-4884, 1998.

[8] S.A. Altus. *Multidisciplinary Optimization Using Optimizer Based Decomposition*. PhD thesis, Stanford University, Jun 1997.

[9] Anon. "Hybrid Laminar Flow Tests Cut Drag, Fuel Burn on 757". *Aviation Week and Space Technology*, page 36, 1991.

[10] J-F. Barthelemy, G.A. Wrenn, A.R. Dovi, P.G. Coen, and L.E. Hall. Supersonic Transport Wing Minimum Weight Design Integrating Aerodynamics and Structures. *Journal of Aircraft*, 31, Mar-Apr 1994.

[11] P. Bradshaw and T. Cebeci. *Momentum Transfer in Boundary Layers.* Hemisphere Publishing Corporation, 1977.

[12] P. Bradshaw and T. Cebeci. *Physical and Computational Aspects of Convective Heat Transfer.* Springer-Verlag, 1984.

[13] R.D. Braun. *Collaborative Optimization: An Architecture for Large-Scale Distributed Design.* PhD thesis, Stanford University, Jun 1998.

[14] R.D. Braun, I.M. Kroo, and P. Gage. "Post-Optimality Analysis in Aerospace Vehicle Design". AIAA 93-3932, Aug 1993.

[15] R.D. Braun, I.M. Kroo, P. Gage, and I. Sobieski. "Implementation and Performance Issues in Collaborative Optimization". AIAA Paper 96-4017-CP, 1996.

[16] G.W. Brune and J.H. McMasters. Computational Aerodynamics Applied to High-Lift Systems. In *Applied Computational Aerodynamics.* Battelle Press, 1990. Vol 125 of Progress in Astronautics and Aeronautics, AIAA, Washington D.C.

[17] M.D. Brunner and A. Velicki. "Study of Materials and Structures for High-Speed Civil Transport". NASA CR-191434, 1993.

[18] R.L. Carmichael and L.L. Erickson. "PAN AIR - A Higher Order Panel Method for Predicting Subsonic or Supersonic Linear Potential Flows about Arbitrary Configurations". AIAA Paper 81-1255, 1991.

[19] D. Cauchon. "Successor to Concorde Can't Get Off the Ground". *USA Today*, page 8D, 6 Apr 1999.

[20] National Research Council. *U.S. Supersonic Commercial Aircraft: Assessing NASA's High Speed Research Program.* National Academy Press, Washington, D.C., 1997.

[21] Boeing Commercial Aircraft New Airplane Development. "High-Speed Civil Transport Study". NASA CR-4233, 1989.

[22] M. Drela. *Two-Dimensional Transonic Aerodynamic Design and Analysis Using the Euler Equations.* PhD thesis, M.I.T., Feb 1986. MIT GTL Rep No. 187.

[23] G.S. Dulikravich. *Aerodynamic Shape Optimization Methods*, pages 175–187. Springer Wien, New York, 1997.

[24] G.S. Dulikravich. *Multidisciplinary Inverse Design and Optimization*, pages 223–236. Springer Wien, New York, 1997.

[25] G.S. Dulikravich. *Structural Inverse Design and Optimization*, pages 213–221. Springer Wien, New York, 1997.

[26] D. Dwiggins. *The SST: Here It Comes Ready or Not.* Doubleday and Company, 1968.

[27] L. Erikson. "Panel Methods-An Introduction". NASA TP 2995, Apr 1991.

[28] H.D. Fuhrmann. "Application of Natural Laminar Flow to a Supersonic Transport Concept". AIAA Paper 93-3467, 1993.

[29] P.J. Gage. "New Approaches to Optimization in Aerospace Conceptual Design". NASA CR 196695, Mar 1995.

[30] J.P. Geising and J.F. Barthelemy. "A Summary of Industry MDO Applications and Needs". AIAA Paper 98-4737, 1998.

[31] B.T. Gibson and H.A. Gerhardt. "Development of an Innovative Natural Laminar Flow Wing Concept for High-Speed Civil Transports". AIAA Paper 93-3466, 1993.

[32] B.T. Gibson and H.A. Gerhardt. "Natural Laminar Flow Wing Concept for Supersonic Transport". *Journal of Aircraft*, 32(1), Jan-Feb 1995.

[33] G.L. Giles. *ELAPS User's Manual*, 1996.

[34] R. Hallion. *Supersonic Flight.* The Macmillan Company, 1972.

[35] D.N. Halsey and J.L. Hess. "A Geometry Package for Generation of Input Data for a Three-Dimensional Potential Flow Program". NASA CR-2962, Jun 1978.

[36] J.B. Heywood. *Internal Combustion Engine Fundamentals.* McGraw-Hill, 1998.

[37] R. Joslin. "Overview of Laminar Flow Control". NASA TP-1998-208705, 1998.

[38] D.L. Knill. Response Models Combining Linear and Euler Aerodynamics for Supersonic Transports. *Journal of Aircraft*, 36, Jan-Feb 1999.

[39] D.L. Knill, A.A. Guinta, C.A. Baker, B. Grossman, W.H. Mason, R.T. Hafka, and L.T. Watson. "HSCT Configuration Design Using Response Surface Approximations of Supersonic Euler Aerodynamics". AIAA 98-0905, 1998.

[40] V.A. Komarov. "Aircraft Structural Design - Improving Conceptual Design Level Fidelity". AIAA Paper 98-4885, 1998.

[41] I.M. Kroo. "An Interactive System for Aircraft Design and Optimization". AIAA Aerospace Design Conference, AIAA Paper 92-1190. AIAA Paper 92-1190, Feb 1992.

[42] I.M. Kroo. Aircraft Design, Synthesis and Analysis. Stanford Univerity, Jan 1999.

[43] A. Lippisch. *The Delta Wing: History and Development.* Iowa State University Press, 1971.

[44] H. G. Loos. "A Simple Laminar Boundary Layer with Secondary Flow". *Journal of the Aeronautical Sciences*, pages 35–40, Jan 1955.

[45] M. R. Malik. "COSAL - A Black Box Compressible Stability Analysis Code for Transition Prediction in Three-Dimensional Boundary Layers". NASA CR 165925, May 1982.

[46] M. R Malik, P. Balakumar, and C.-L. Chang. "Linear Stability of Hypersonic Boundary Layers". Paper No. 189, Apr 1991. 10th National Aero-Space Plane Symposium.

[47] V.M. Manning and I.M. Kroo. "Multidisciplinary Optimization of a Natural Laminar Flow Supersonic Aircraft". AIAA Paper 99-3102, Jun 1999. Presented at the 17th Applied Aerodynamics Conference.

[48] L.A. McCullers. Aircraft Configuration Optimization Including Optimized Flight Profile. In Jaroslow Sobieski, editor, *Recent Experiences in Multidisciplinary Analysis and Optimization*, number NASA CP-2327, 1984.

[49] F. E. McLean. "Supersonic Cruise Technology". NASA SP-472, 1985.

[50] J. Mertens. *Aerodynamic Shape Optimization Methods*, pages 275–290. Springer Wien, New York, 1997.

[51] J. Mertens. *Certifications of Supersonic Civil Transports*, pages 97–103. Springer Wien, New York, 1997.

[52] J. Mertens. *Required Aerodynamic Technologies*, pages 70–96. Springer Wien, New York, 1997.

[53] NBAA. National Business Aviation Association. http://www.nbaa.org/, 1999. World Wide Web site.

[54] D.T. Nguyen. "Final Report: Finite Element Software for Multidisciplinary Optimization". Old Dominion University, 1995. for NASA Langley Contract NASI-19858.

[55] L.M. Nicolai. *Fundamentals of Aircraft Design.* E.P. Domicone Printing Services, Fairborne, OH, 1975.

[56] H. Noenlinger, J. Krammer, and M. Stettner. "MDO Technology Needs in Aeroservoelastic Structural Design". AIAA Paper 98-4731, 1998.

[57] Office of Technology Assessment. "Impact of Advanced Air Transport Technology, Part 1: Advanced High-Speed Aircraft". OTA-T-112, Apr 1980.

[58] J.R. Olds and K.B. Steadman. "Cross-Platform Computational techniques for Analysis Code Integration and Optimization". AIAA Paper 98-4743, 1998.

[59] J. Rech and C.S. Leyman. "A Case Study by Aerospatiale and British Aerospace on the Concorde". AIAA Professional Study Series, 1980.

[60] LT S.A. Reed, Y.I. Moon, A.A. Bhungalia, and V.B. Venkayya. "Aerodynamics-Structures Interaction in MDO". AIAA Paper 98-4780, 1998.

[61] L. Reithmaier. *Mach 1 and Beyond.* McGraw-Hill, 1995.

[62] T.L. Rishko. Performance and Robustness of Multidisciplinary Optimization Architechtures. Engineer Thesis, Stanford University, Jun 1999.

[63] W.P. Rodden and E.H. Johnson. *MSC/NASTRAN User's Guide.* The Machneal-Schwendler Corporation, 1994.

[64] P. Rohl, B. He, and P. Finnigan. "A Collaborative Optimization Environment for Turbine Engine Development". AIAA Paper 98-4737, 1998.

[65] P.J. Röhl, D.M. Mavris, and D.P. Schrage. "A Multilevel Wing Design Procedure Centered on the Astros Structural Optimization System". AIAA Paper 94-4411, 1994.

[66] P.J. Röhl, D.M. Mavris, and D.P. Schrage. "Combined Aerodynamic and Structural Optimization of a High-Speed Civil Transport Wing". AIAA Paper 95-1222, 1995.

[67] H. Schlicting. *Boundary Layer Theory.* McGraw-Hill, 1979.

[68] R. Shevell. *Fundamentals of Flight.* Prentice Hall, N.J., 1989.

[69] W.A. Shurcliff. *S/S/T and Sonic Boom Handbook.* Ballantine Books, 1970.

[70] H. Sobieczky. *New Design Concepts for High Speed Air Transport.* Springer Wien, 1997.

[71] I.P. Sobieski. *Collaborative Optimization Using Response Surface Estimation.* PhD thesis, Stanford University, Sep 1998.

[72] I.P. Sobieski and I.M. Kroo. "Aircraft Design Using Collaborative Optimization". AIAA Paper 96-0715, 1996.

[73] I.P. Sobieski and I.M. Kroo. "Collaborative Optimization Using Response Surface Estimation". AIAA Paper 98-0915, 1998.

[74] I.P. Sobieski, V.M. Manning, and I.M. Kroo. "Response Surface Estimation and Refinement in Collaborative Optimization". AIAA Paper 98-4753, 1998.

[75] L. Sowerby. "Secondary Flow in a Boundary Layer". Rept. 16832, Aeronautical Research Council, 1954.

[76] Pierre Sparaco. "Dassault Explores Supersonic Business Jet Perspectives". *Aviation Week and Space Technology*, page 62, 19 Oct 1998.

[77] P. Sturdza, V.M. Manning, and I.M. Kroo. "Boundary Layer Calculations for Preliminary Design of Wings in Supersonic Flow". AIAA Paper 99-3104, Jun 1999. Presented at the 17th Applied Aerodynamics Conference.

[78] B. Suiru and J.D. Busick. *Future Flight.* TAB Aero, Blue Ridge Summit, 1994.

[79] Richard R. Tracy. U.S. Patent No. 5322242, Jun 1994.

[80] R.R. Tracy, I.M. Kroo, J. Chase, and J. Viken. "Exploiting Natural Laminar Flow for Economical Supersonic Transport". SAE Paper 952040, Sep 1995.

[81] E.R. Unger and P.G. Coen. "Aerodynamic-Performance Planform and Camber Optimization of a Supersonic Transport Wing". NASA CR 932632, 199-.

[82] A. Van der Velden. *Multidisciplinary Supersonic Transport Design*, pages 275–290. Springer Wien, New York, 1997.

[83] A.J.M. Van der Velden. "The Conceptual Design of a Mach 2 Oblique Flying Wing Supersonic Transport". NASA CR 177529, May 1989.

[84] A.J.M. Van der Velden and I.M. Kroo. "The Aerodynamic Design of the Oblique Flying Wing Supersonic Transport". NASA CR 177552, Jun 1990.

[85] Theodore von Karman. *Aerodynamics*. McGraw Hill, 1963.

[86] F.M. White. *Viscous Fluid Flow*. Hemisphere Publishing Corporation, New York, 1991. 2nd ed.

[87] F.A. Woodward. "An Improved Method for the Aerodynamic Analysis of Wing-Body-Tail Configurations in Subsonic and Supersonic Flow, Part I, Theory and Applications". NASA CR-2228, 1973.

Appendix A

Compressible Boundary Layer Analysis

A.1 Derivation of the Orr-Sommerfield Equation

From the unsteady Navier Stokes equations, thin shear layer (TSL) approximations allow retention of only linear terms in u', v', and w', as the Reynolds stress produced by the disturbance is neglected: $-\rho\overline{u'v'} = -\rho\overline{u'w'} = 0$ [1] Thin shear layer (TSL) approximations retain only linear terms in u', v', and w', as the Reynolds stress produced by the disturbance is neglected: $-\rho\overline{u'v'} = -\rho\overline{u'w'} = 0$

The TSL equations have the following form, where $s = u$, v, or w.

$$\begin{aligned}
&\frac{\partial s'}{\partial t} + u'\frac{\partial s}{\partial x} + u \\
&\frac{\partial s'}{\partial x} + v'\frac{\partial s}{\partial y} + v \\
&\frac{\partial s'}{\partial y} + w'\frac{\partial s'}{\partial z} + w \\
&\frac{\partial s'}{\partial z} = \frac{-1}{\rho}\frac{\partial P'}{\partial n} + \nu\nabla^2 s'
\end{aligned} \tag{A.1}$$

where $n = x$ for the x equation, $n = y$ for the y equation, and $n = z$ for the z equation. Also, the instantaneous continuity equation applies:

[1] $' \rightarrow$ fluctuating parts.

$$\frac{\partial u'}{\partial x} + \frac{\partial v'}{\partial y} + \frac{\partial w'}{\partial z} = 0 \tag{A.2}$$

Assuming the streamwise wavelength of the disturbance is only a few boundary layer thicknesses, therefore the X-wise gradient of u' and v' are of the same order. This is essentially saying $v = 0$: the parallel flow approximation. So along with the assumption of two dimensional flow the equations become:

$$\frac{\partial u'}{\partial x} + \frac{\partial v'}{\partial y} = 0 \tag{A.3}$$

$$\frac{\partial u'}{\partial t} + u\frac{\partial u'}{\partial x} + v'\frac{\partial u}{\partial y} = \frac{-1}{\rho}\frac{\partial P'}{\partial x} + \nu\left[\frac{\partial^2 u'}{\partial x^2} + \frac{\partial^2 u'}{\partial y^2}\right] \tag{A.4}$$

$$\frac{\partial v'}{\partial t} + u\frac{\partial v'}{\partial x} = \frac{-1}{\rho}\frac{\partial P'}{\partial y} + \nu\left[\frac{\partial^2 v'}{\partial x^2} + \frac{\partial^2 v'}{\partial y^2}\right] \tag{A.5}$$

Now taking the small disturbance to be a sinusoidal traveling plane wave (a Tollmein-Schlichting wave) with the form:

$$g'(x, y, z, t) = g(y)\exp[i(\alpha x - \beta z - \omega t)] \tag{A.6}$$

where: g(y) = complex amplitude function, α is the complex wave number in the x direction $\left(\frac{2\phi}{\lambda_x}\right)$, β is the complex wave number in the z direction $\left(\frac{2\phi}{\lambda_z}\right)$, and ω is the circular frequency in radians.

Also:

$RE(\exp) \rightarrow$ growth of disturbance amplitude in x or t

$IM(\exp) \rightarrow$ sinusoidal oscillation of disturbance in x or t: $\cos\theta + i\sin\theta$ and:

$\alpha = \alpha_r + i\alpha_i$ and $\omega = \omega_r + i\omega_i$ then if $\beta = 0$:

$RE(\exp) = (-\alpha_i x + \omega_i t)$ and $IM(\exp) = (i[\alpha_r x - \omega_r t])$

if $\beta = 0$, the direction of propagation of the wave is in the x direction, but if $\beta \neq 0$, the

wave propagation direction is inclined at an angle γ with respect to the freestream, where $\gamma = \tan^{-1}\frac{\beta}{\alpha}$.

To get to the equation for the rate of change of fluctuating vorticity following fluid along a mean streamline, eliminate pressure from the equations by taking the derivative of the x equation with respect to y and of the y equation with respect to x:

$$\frac{\partial}{\partial y}\left(\frac{\partial u'}{\partial t} + u\frac{\partial u'}{\partial x} + v'\frac{\partial u}{\partial y} = \frac{-1}{\rho}\frac{\partial P'}{\partial x} + \nu\left[\frac{\partial^2 u'}{\partial x^2} + \frac{\partial^2 u'}{\partial y^2}\right]\right.$$

$$\frac{\partial}{\partial x}\left(\frac{\partial v'}{\partial t} + u\frac{\partial v'}{\partial x} = \frac{-1}{\rho}\frac{\partial P'}{\partial y} + \nu\left[\frac{\partial^2 v'}{\partial x^2} + \frac{\partial^2 v'}{\partial y^2}\right]\right.$$

yielding,

$$\frac{\partial^2 u'}{\partial t \partial y} + \frac{\partial u}{\partial y}\frac{\partial u'}{\partial x} + u\frac{\partial^2 u'}{\partial x \partial y} + \frac{\partial v'}{\partial y}\frac{\partial u}{\partial y} + v'\frac{del^2 u}{\partial y^2} = \frac{-1}{\rho}\frac{\partial P'}{\partial x \partial y} + \nu\left[\frac{\partial^3 u'}{\partial x^2 \partial y} + \frac{\partial^3 u'}{\partial y^3}\right] \tag{A.7}$$

and

$$\frac{\partial^2 v'}{\partial t \partial x} + \frac{\partial u}{\partial x}\frac{\partial v'}{\partial x} + u\frac{\partial^2 v'}{\partial^2 x} = \frac{-1}{\rho}\frac{\partial P'}{\partial y \partial x} + \nu\left[\frac{\partial^3 v'}{\partial x^3} + \frac{\partial^3 v'}{\partial y^2 \partial x}\right] \tag{A.8}$$

subtracting one from the other:

$$\frac{\partial}{\partial t}\left(\frac{\partial u'}{\partial y} - \frac{\partial v'}{\partial x}\right) + u\frac{\partial}{\partial x}\left(\frac{\partial u'}{\partial y} - \frac{\partial v'}{\partial x}\right) + v'\frac{\partial^2 u}{\partial y^2} = \nu\left[\frac{\partial^3 u'}{\partial x^2 \partial y} - \frac{\partial^3 v'}{\partial y^2 \partial x} + \frac{\partial^3 u'}{\partial y^3} - \frac{\partial^3 v'}{\partial x^3}\right] \tag{A.9}$$

now define the stream function $u' = \frac{\partial \psi}{\partial y}$ $v' = -\frac{\partial \psi}{\partial x}$

to produce:

$$\frac{\partial}{\partial t}(\nabla^2 \psi) + u\frac{\partial}{\partial x}(\nabla^2 \psi) - \frac{\partial \psi}{\partial x}\frac{\partial^2 u}{\partial y^2} = \nu(\nabla^4 \psi) \tag{A.10}$$

where $\nabla^4 = \nabla^2 \nabla^2$ and $-\nabla^2 \psi$ is the fluctuating z-component of vorticity $\left(\frac{\partial v'}{\partial x} - \frac{\partial u'}{\partial y}\right)$

Define the disturbance Stream Function in complex notation with $\beta = 0$ as:

$$\psi(x, y, t) = \phi(y)\exp[i(\alpha x - \omega t)] \tag{A.11}$$

where $\phi(y)$ is the complex amplitude of the disturbance and α is the wave number of the disturbance ($\lambda = \frac{2\pi}{\alpha}$).

If α is complex, then the amplitude varies with x as $\exp(-\alpha_i x)$ [spatial]. If ω is complex, then the amplitude varies with time as $\exp(-\omega_i t)$ [temporal]. If both are real, then the disturbance propagates through parallel mean flow with constant amplitude $\phi(y)$ and if both are complex, the disturbance amplitude varies in both time and space.

Plugging the disturbance stream function into the governing equation we get the most general form of the Orr Sommerfield equation:

$$(u - \frac{\omega}{\alpha})(\phi'' - \alpha^2\phi) - u''\phi = \frac{\nu}{i\alpha} + (\phi'''' - 2\alpha^2\phi'' + \alpha^4\phi'') \tag{A.12}$$

This is the fundamental equation for incompressible stability theory, in which the primes $(')$ represent $\frac{\partial}{\partial y}$. To introduce dimensionless variables, divide velocities by U_∞, lengths by l, and introduce a dimensionless time variable $\rightarrow \frac{tu_\infty}{l}$

This leads to the dimensionless form of the Orr Sommerfield equation:

$$[\phi'''' - 2\alpha_l^2\phi'' + \alpha_l^4\phi''] = iR[(\alpha_l\tilde{u} - \tilde{\omega})(\phi'' - \alpha_l^2\phi) - \tilde{u}''\alpha_l\phi] \tag{A.13}$$

Where $R = \frac{u_\infty l}{\nu}$ $\tilde{u} = \frac{u}{u_\infty}$ $\tilde{\omega} = \frac{\omega}{u_\infty}$

- $\lambda_x = \frac{2\pi}{\alpha_r}$ is the wavelength of the disturbance in the x-direction
- ϕ is the complex amplitude function f(y) of the perturbation velocity in the y-direction.
- α is the complex wave number. α_i is the spatial amplification rate
- ω is the complex frequency of the disturbance. ω_r is the circular frequency
- c is the propagation speed, $\frac{\omega}{\alpha}$
- for 2-D stability, the velocity profile U is a function of y for a given x by local similarity. $\beta = 0$
- for 3-D stability, the velocity profile U, W are functions of y for given x and z by local similarity. $\beta \neq 0$. α and β are related by the condition that $\frac{\partial\alpha}{\partial\beta}$ is real.

- for 3-D spatial amplification theory , amplitude varies with x and z as (exp $(-\alpha i X - \beta i Z)$). In temporal theory, it varies with time as (exp (w, T)).

A.2 Proof of Inflection Point Theorem

It is necessary for instability that the velocity profile have a point of inflection. [86]

For linear, parallel flow, $\frac{1}{Re} \to 0$

$$\frac{\partial}{\partial t} \nabla^2 v + U(y) \frac{\partial}{\partial x} \nabla^2 v - \frac{\partial}{\partial x} v \frac{\partial^2 U}{\partial y^2} = 0 \tag{A.14}$$

This has a solution of the form $v = \phi(y) e^{\sigma t} e^{i\alpha x}$, which is periodic in x and growing in time if $\sigma > 0$. If the flow is unstable, $\sigma > 0$

$$\begin{array}{ll} \frac{\partial v}{\partial t} = \sigma v & \frac{\partial v}{\partial x} = i\alpha v \\ \frac{\partial}{\partial t} \to \sigma & \frac{\partial}{\partial x} \to i\alpha \end{array} \tag{A.15}$$

Therefore A.14 becomes $\sigma \left(\frac{\partial^2 v}{\partial y^2} - \alpha^2 v \right) + U(y) i\alpha \left(\frac{\partial^2 v}{\partial y^2} - \alpha^2 v \right) - i\alpha v \frac{\partial^2 U}{\partial y^2} = 0$

$$\text{so } [\sigma + i\alpha U(y)] \left[\frac{\partial^2 v}{\partial y^2} - \alpha^2 v \right] - i\alpha v \frac{\partial^2 U}{\partial y^2} = 0 \tag{A.16}$$

The boundary conditions for equation A.16 are: at $y = a$ and $y = b$, $v(a) = v(b) = 0$

Let $vv^* = |v|^2$, where $v^* = \phi(y)e^{\sigma t}e^{-i\alpha x}$ so from A.16:

$$\int_a^b \left(\frac{\partial^2 v}{\partial y^2} - \alpha^2 v\right) v^* dy = \int_a^b \frac{i\alpha v v^* \frac{d^2U}{dy^2}}{(\sigma + i\alpha U(y))} dy$$

$$\int_a^b \left(\frac{\partial^2 v}{\partial y^2} v^* - \alpha^2 v v^*\right) dy = i\int_a^b \frac{i\alpha |v|^2 \frac{d^2U}{dy^2}}{(\sigma + i\alpha U(y))} dy$$

$$v^* \frac{\partial v}{\partial y}|_a - \int_a^b \frac{\partial v}{\partial y}\frac{\partial v^*}{\partial y} - \int_a^b \alpha^2 |v|^2 dy = i\int_a^b \frac{i\alpha |v|^2 \frac{d^2U}{dy^2}}{(\sigma + i\alpha U(y))} dy$$

$$-\int_a^b \left|\frac{\partial |v|}{\partial y}\right|^2 - \int_a^b \alpha^2 |v|^2 dy = i\int_a^b \frac{i\alpha |v|^2 \frac{d^2U}{dy^2}}{(\sigma + i\alpha U(y))} dy$$

$$\int_a^b \left(\left|\frac{\partial v}{\partial y}\right|^2 + \alpha^2 |v|^2\right) dy = -i\int_a^b \frac{\alpha |v|^2 \frac{d^2U}{dy^2}}{(\sigma + i\alpha U(y))} dy$$

$$\int_a^b \left(\left|\frac{\partial v}{\partial y}\right|^2 + \alpha^2 |v|^2\right) dy = -i\int_a^b \frac{\alpha |v|^2 \frac{d^2U}{dy^2}}{(\sigma + i\alpha U(y))}\frac{(\sigma^* - i\alpha U(y))}{(\sigma^* - i\alpha U(y))} dy$$

$$\int_a^b \left(\left|\frac{\partial v}{\partial y}\right|^2 + \alpha^2 |v|^2\right) dy = -i\int_a^b \frac{(\sigma^* - i\alpha U(y))\alpha |v|^2 \frac{d^2U}{dy^2}}{|\sigma + i\alpha U(y)|^2} dy \qquad \text{(A.17)}$$

where $\sigma^* = \sigma_r - i\sigma_i$

The LHS of equation A.17 has no factors of i, so the coefficient of i on the RHS must equal zero. Therefore:

$$0 = \int_a^b \frac{-\sigma_r \alpha |v|^2 \frac{d^2U}{dy^2}}{|\sigma + i\alpha U(y)|^2} dy$$

but $c \equiv \frac{i\sigma}{\alpha}$ ⟵ wave speed

$$0 = -\frac{\sigma_r \alpha}{|i\alpha|^2}\int_a^b \frac{|v|^2 \frac{d^2U}{dy^2}}{\left|\frac{\sigma}{i\alpha} + U(y)\right|^2} dy$$

$$0 = \frac{\sigma_r}{\alpha}\int_a^b \frac{|v|^2 \frac{d^2U}{dy^2}}{|c + U(y)|^2} dy \qquad \text{(A.18)}$$

For equation A.18 to be true, either $\sigma_r = 0$ (the disturbance does not grow) OR $\int_a^b \frac{|v|^2 \frac{d^2U}{dy^2}}{|c+U(y)|^2} dy = 0$.

It is given that $\frac{|v|^2}{|c+U|^2} > 0$, so in order for the integral to go to zero , $\frac{d^2U}{dy^2}$ must $= 0$ at some

point in order to at some time be both greater than and less than zero. It holds then, that a necessary condition for $\sigma_r > 0$ is that $\frac{d^2U}{dy^2} = 0$ for some y.

A.3 Heat Transfer Effects in Compressible Boundary Layers

In a compressible boundary layer, at least four additional quantities (density, viscosity, temperature and rate of heat transfer) must be considered in addition to those in incompressible flows. Thus, a parameter must be considered which is connected with the rate of heat transfer between the fluid and the wall. [67] When the fluid is incompressible, heat can exchange only if the wall temperature is originally higher or lower than the fluid temperature. When the fluid is compressible however, heat evolved in the boundary layer produces an additional important influence. A thermal boundary layer develops in addition to the velocity boundary layer. This additional parameter plays a part in stability, as transfer of heat from the boundary layer to the wall can now occur regardless of the initial relative temperatures. This stabilizing or destabilizing effect due to the transfer of heat is a consequence of the dependence of μ on T. (The viscosity of gases increases with T.) When $T_w > T_\infty$ the boundary layer is less stable, and when the relation is reversed, the layer is more stable. The latter situation is stabilizing because the critical Reynolds number increases. The former is destabilizing due to a presence of a point of inflection in the velocity profile as well as a lower critical Reynolds number. The way the relationship between wall and freestream temperature corresponds to velocity profile curvature is shown below:

$$\frac{d}{dy}\left(\mu\frac{dU}{dy}\right)_w = \frac{dp}{dx} \text{ from the momentum equation.}$$

$$\text{if } \frac{dp}{dx} = 0, \frac{d}{dy}\left(\mu\frac{\partial U}{\partial y}\right)_w = 0$$

$$\text{then } \mu_w\left(\frac{\partial^2 U}{\partial y^2}\right)_w + \left(\frac{d\mu}{dy}\right)_w\left(\frac{dU}{dy}\right)_w = 0$$

$$\text{therefore } \left(\frac{\partial^2 U}{\partial y^2}\right)_w = -\frac{1}{\mu_w}\frac{d\mu}{dy}_w \frac{dU}{dy}_w = \text{curvature of velocity profile at wall}$$

$$\text{if } T_w > T_\infty \text{ , } \left(\frac{\partial T}{\partial y}\right)_w < 0 \text{ (temperature gradient at the wall is negative)}$$

$$\text{since } \mu \uparrow \text{ as } T \uparrow \text{ (} \mu \text{ is an increasing function of temperature therefore) } \left(\frac{\partial \mu}{\partial y}\right)_w < 0$$

$$\text{so if } T_w > T_\infty \text{ , } \left(\frac{\partial^2 U}{\partial y^2}\right)_w > 0 \text{ because } \left(\frac{\partial U}{\partial y}\right)_w > 0$$

$$\text{and if } T_w < T_\infty \text{ , } \left(\frac{\partial^2 U}{\partial y^2}\right)_w < 0$$

If the curvature of the velocity profile, $\frac{d^2U}{dy^2}$, is positive at the wall (as for a heated wall), then the velocity profile *must* have a point of inflection. This is because at the edge of the velocity boundary layer, the curvature of the velocity profile, $\frac{d^2U}{dy^2}$, is very small but negative and in order to go from positive to negative it must pass through zero. [67] For a cooled wall, where the wall temperature is less than that of the freestream, the curvature is negative, so an inflection point may not exist. As the presence of a point of inflection in the boundary layer indicates instability, the transfer of heat to the fluid has a similar effect on the flow as an adverse pressure gradient, whereas heat flow in the opposite direction corresponds to a favorable pressure gradient (in its effect on stability). The work of compression and energy dissipation produces a rise in temperature of a compressible boundary layer as it flows, thus can heat the wall, creating the transfer of heat in the favorable direction. It is for this reason that some laminar flow control practices involve wall cooling in order to stabilize the boundary layer.

Why is a point of inflection in the boundary layer an indication of instability? This question is answered by the point of inflection theorem.

Appendix A.2 shows that heat transfer from the gas to the wall raises the stability limit, while transfer from the wall to the gas lowers it. What if there is *no* heat transfer? This is the case of the adiabatic wall, when the boundary layer is not assumed to heat the wall,

but is still slightly more stable than a boundary layer in incompressible flow.

There is a case in which a compressible boundary layer is *not* assumed to heat the wall, the case of the adiabatic wall. This occurs when there exists a perfect balance between viscous dissipation and heat conduction so as to keep the stagnation enthalpy constant in an adiabatic boundary layer. The Prandtl number, $\frac{\mu c_p}{\kappa}$, effectively a ratio of the diffusion of momentum to the diffusion of heat, is equal to unity in this situation, and $P = \rho RT$ and $dh = c_p dT$.

From the 2D compressible boundary layer equations (see Equation 3.2):

$$\rho \frac{DH}{Dt} = \frac{\partial p_e}{\partial t} + \frac{\partial}{\partial y}\left(\kappa \frac{\partial T}{\partial y} + \mu u \frac{\partial u}{\partial y}\right)$$

$$\rho u \frac{\partial H}{\partial x} + \rho v \frac{\partial H}{\partial y} = \frac{\partial}{\partial y}\left(\frac{\mu}{Pr}\frac{\partial H}{\partial y}\right) + \frac{\partial}{\partial y}\left[\left(1 - \frac{1}{Pr}\right)\mu u \frac{\partial u}{\partial y}\right]$$

If Pr = 1, then the total enthalpy is a solution, where from the energy relation it can be shown: [86]

$$H = constant = h + \frac{u^2}{2} = h_w + (H_e - h_w)\frac{u}{U_e}$$

Therefore,

$$\left(\frac{\partial H}{\partial y}\right)_0 = 0 \quad \text{so} \quad \left(\frac{\partial h}{\partial y}\right)_0 = 0 \quad \text{because} \quad \left(\frac{\partial\left(\frac{u^2}{2}\right)}{\partial y}\right)_0 = 0$$

which indicates zero heat transfer at the wall.

Additionally, if $c_p = constant$, $h = (c_p T + constant)$, $Pr = 1$, and $\frac{dP}{dx} = 0$ then from the definition of the total enthalpy:

$$T = T_w + \left(T_e + \frac{U_e^2}{2c_p} - T_w\right)\frac{u}{U_e} - \frac{u^2}{2c_p} \tag{A.19}$$

$$T = T_w + (T_{aw} - T_w)\frac{u}{U_e} - \frac{u^2}{2c_p} \tag{A.20}$$

where $T_e + \dfrac{U_e^2}{2c_p} = T_{aw}$ (adiabatic wall temperature)

and $T_{ad} - T_e =$ temperature increase of an adiabatic wall which is due to frictional heat.

$$\text{The heat flux is denoted by } q_w = \frac{(T_{aw} - T_w)\,\kappa_w \tau_w}{U_e \mu_w} \tag{A.21}$$

For an adiabatic wall boundary layer, the stabilizing effect of compressibility lies not in the favorable results of fluid-to-wall heat transfer, but only in the compressible fluid properties. A boundary layer in this situation is more stable than an incompressible fluid, but less than a layer experiencing the favorable effects of compressible fluid properties *and* heat transfer. At very low compressible Mach numbers, this effect is fairly insignificant, but as Mach number increases, the critical Reynolds number based upon ∂^* decreases slightly, intensifying the favorable effect.

As stated, compressibility causes density variations as well as fluid temperature variations too large to permit the assumption of constant μ and κ. High speed flows have large amounts of kinetic energy which can be dissipated into heat by the boundary layer. This is modeled in the term $\mu\left(\frac{\partial u}{\partial y}\right)^2$ in the energy equation (from Equation 3.2), and represents the difference between the stagnation and static temperatures. If the wall is adiabatic, the temperature of that wall attains at equilibrium depends upon the amount of this energy that is recovered on the wall. So for this type of wall, there is no heat transfer, but the fluid temperature increases thus viscosity rises and the fluid-wall interaction changes.

The boundary layer code used in this analysis permits the user to specify wall temperature or heat flux. For an adiabatic wall, the wall temperature can be computed and supplied as a boundary condition. For specified heat flux conditions, a value of zero heat flux can be supplied. These two results are similar, as can be seen in Figure A.1. In this figure, a 2.5 percent thick supersonic airfoil is run for each set of boundary conditions. Reference [86] states that the adiabatic wall temperature can be computed from the Prandtl number, Mach number, and local velocity.

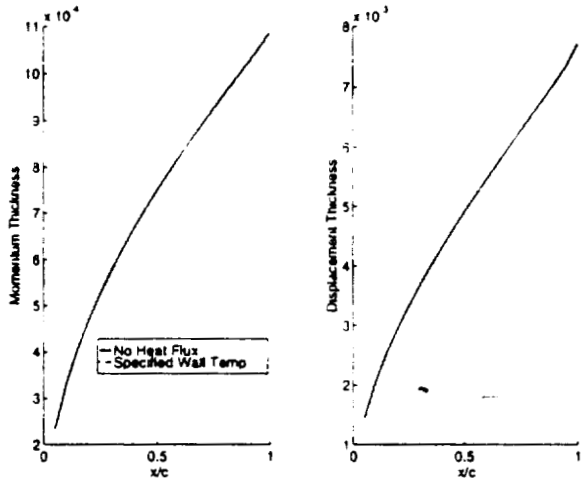

Figure A.1: 2-D Boundary layer properties, wall temperature supplied, and zero heat flux supplied. Mach = 2.4, Re = 235 million

$$
\begin{aligned}
T_1 &= 1 + \sqrt{PR}\frac{(\gamma-1)}{2}M^2\left(\frac{U_e}{U_\infty}\right)^2 \\
T_2 &= 1 - \frac{(\gamma-1)}{2}M^2\left[\left(\frac{U_e}{U_\infty}\right)^2 - 1\right] \\
\frac{T_{aw}}{T_\infty} &= \frac{(T_1 - T_2)}{(T_1 - 1)}
\end{aligned}
\tag{A.22}
$$

Appendix B

Conventional HSCT Compiled Results

B.1 Subproblem and System Level Objective Progression

Values Predicted at System Level				
CYCLE	J_{system}	$J_{aerodynamics}$	$J_{mission}$	$J_{structures}$
Baseline	-	-	-	-
Cycle 2	8.34	8.7×10^{-6}	4.84×10^{-5}	6.86×10^{-4}
Cycle 3	9.74	1.04×10^{-4}	1.22×10^{-4}	2.70×10^{-3}
Cycle 4	10.03	5.59×10^{-4}	5.81×10^{-5}	2.79×10^{-3}
Cycle 5				
Cycle 6	6.0421	7.0734×10^{-9}	2.933×10^{-7}	2.55×10^{-5}
Cycle 7	6.0145	2.67978×10^{-8}	2.0763×10^{-6}	1.17746×10^{-6}
Cycle 8	6.0050	1.8641×10^{-9}	2.3425×10^{-6}	2.4079×10^{-7}
Cycle 9	5.9533	1.0928×10^{-9}	5.654×10^{-7}	2.75×10^{-7}
Cycle 10	5.9048	9.965×10^{-10}	2.162×10^{-6}	5.241×10^{-7}
Cycle 11	5.8889	3.855×10^{-6}	1.693×10^{-7}	4.064×10^{-6}
Cycle 12	5.863	1.363×10^{-6}	6.174×10^{-7}	2.747×10^{-6}

Values Computed by Disciplines				
CYCLE	J_{system}	$J_{aerodynamics}$	$J_{mission}$	$J_{structures}$
Cycle 1	1098.04	1.09	2.33×10^{-9}	3.90×10^{-4}
Cycle 2	189.55	8.68×10^{-6}	8.92×10^{-2}	9.28×10^{-2}
Cycle 3	14.19	1.04×10^{-4}	7.94×10^{-11}	7.27×10^{-3}
Cycle 4	11.98	5.59×10^{-4}	4.94×10^{-10}	4.80×10^{-3}
Cycle 5	104.01	8.1137×10^{-3}	5.4257×10^{-10}	2.999×10^{-3}
Cycle 6	18.03	1.0697×10^{-2}	2.364×10^{-7}	1.32×10^{-3}
Cycle 7	7.17	1.1472×10^{-3}	1.4314×10^{-6}	9.8111×10^{-6}
Cycle 8	6.04	1.8641×10^{-9}	6.4059×10^{-7}	3.3335×10^{-5}
Cycle 9	5.97	1.0928×10^{-9}	6.455×10^{-7}	1.8468×10^{-5}
Cycle 10	5.928	9.965×10^{-10}	6.721×10^{-7}	2.273×10^{-5}
Cycle 11	5.926	3.855×10^{-6}	3.791×10^{-5}	3.819×10^{-6}
Cycle 12	5.871	1.363×10^{-6}	6.916×10^{-8}	1.041×10^{-5}

B.2 Design Progression

HSCT Design Progression				
Variable Name	*Cycle 1*	*Cycle 2*	*Cycle 3*	*Cycle 4*
$TOGW(lb)$	745000	759387.40	681630.12	661630.12
$ZFW(lb)$	350000	315843.35	294788.21	293909.91
$Altitude(ft)$	52000	57200.00	57380.93	57230.13
L/D	8.3	8.3369	8.6548	8.7560
$SLSTH$ (lb)	60000	54000.00	54104.30	54116.46
F_1	12300	8910.64	6709.66	6109.05
F_2	14090	16921.67	15531.01	15158.0215
F_3	18956	19980.85	18502.52	18004.27
F_4	11041	20878.66	19794.55	19743.68
T_1	27343518	26630622.97	23217354.81	22297714.50
T_2	2191452	1662790.03	1211217.56	1121709.21
T_3	1580612	1261892.89	1001705.55	916566.34
T_4	981795	792351.61	652001.48	626849.51
δ_1(deg)	-0.9	-0.9194	-0.7291	-0.7429
δ_2 (deg)	-1.5	-1.4266	-1.9431	-2.0027
δ_3 (deg)	-3.0	-4.2384	-4.3885	-4.4305
HSCT Performance				
$Range(n.mi.)$	6721	6923	6141	6747
$TOFL(ft)$	11477	12000	10552	9911
$LFL(ft)$	7444	6357	5985	5968
D/T	0.714	0.887	0.820	0.783

HSCT Design Progression				
Variable Name	*Cycle 5*	*Cycle 6*	*Cycle 7*	*Cycle 8*
$TOGW(lb)$	641630.12	601630.12	601127.44	600244.73
$ZFW(lb)$	292786.46	291942.23	292062.94	290614.27
$Altitude(ft)$	55930.13	54531.62	51931.62	51741.30
L/D	8.912	8.65	8.575	8.5713
$SLSTH(lb)$	55616.46	58616.466	61616.46	58616.46
F_1	4959.35	4265.59	3905.19	3830.98
F_2	14654.29	13841.82	13685.53	13685.58
F_3	18159.93	17258.23	17541.70	17521.09
F_4	19741.75	19089.49	19259.43	19373.06
T_1	20927924.73	19354682.81	18958780.28	18886077.87
T_2	873175.26	737111.66	663801.28	651716.99
T_3	567060.80	518354.16	692667.81	685805.58
T_4	567060.80	518354.16	511509.24	507975.67
δ_1(deg)	-0.7343	-0.7351	-0.7374	-0.7412
δ_2 (deg)	-2.5027	-2.5082	-2.5112	-2.5116
δ_3 (deg)	-4.2894	-3.9828	-3.5468	-3.5525
HSCT Performance				
$Range(n.mi.)$	5576	5106	5056	5084
$TOFL(ft)$	9088	7550	7167	7514
$LFL(ft)$	6368	6314	6315	6290
D/T	0.697	0.611	0.542	0.566

HSCT Design Progression				
Variable Name	*Cycle 9*	*Cycle 10*	*Cycle 11*	*Cycle 12*
$TOGW(lb)$	595244.73	590472.14	588076.98	585911.18
$ZFW(lb)$	291921.31	289402.91	289833.73	288583.73
$Altitude(ft)$	52602.94	53230.29	53159.39	53659.39
L/D	8.6373	8.6687	8.6558	8.6859
$SLSTH(lb)$	57744.26	57908.09	58508.09	59158.09
F_1	3969.44	4070.90	4096.27	4128.75
F_2	13538.63	13411.68	13345.77	13307.54
F_3	17338.76	17161.21	17064.90	17007.36
F_4	18967.12	18647.91	18543.83	18346.18
T_1	18850368.69	18796948.86	18743143.25	18749075.37
T_2	675904.71	695867.48	703515.33	705417.57
T_3	695452.67	703047.37	703682.26	704582.93
T_4	510607.43	512551.84	513751.848	513610.65
δ_1(deg)	-0.7387	-0.7378	-0.7387	-0.7087
δ_2 (deg)	-2.5168	-2.5067	-2.4707	-2.4847
δ_3 (deg)	-3.5750	-3.5926	-3.5566	-3.5746
HSCT Performance				
$Range(n.mi.)$	5012	5033	5000	5000
$TOFL(ft)$	7497	7353	7222	7082
$LFL(ft)$	6308	6260	6256	6242
D/T	0.580	0.583	0.573	0.572

B.3 Subproblem Result Progression

Cycle 1				
Variable Name	*Target*	*Aerodynamics*	*Structures*	*Mission*
TOGW (lb)	745000	749888.19	744984.54	744999.70
ZFW (lb)	350000	-	349846.39	350000.52
Altitude (ft)	52000	56953.31	52000.59	51999.85
L/D	8.3	8.40	-	8.30
SLSTH (lb)	60000	-	60000.87	59999.59
F_1	12300	10060.13	12266.71	-
F_2	14090	15521.71	14093.88	-
F_3	18956	19970.43	18958.83	-
F_4	11041	17966.21	11041.19	-
T_1	27343518	26466881.64	27336178.99	-
T_2	2191452	1862927.05	2193184.38	-
T_3	1580612	1389584.36	1573704.12	-
T_4	981795	867223.41	997567.54	-
δ_1(deg)	-.9	-1.02	-0.89	-
δ_2 (deg)	-1.5	-1.30	-1.51	-
δ_3 (deg)	-3.0	-2.77	-3.00	-

Cycle 2				
Variable Name	*Target*	*Aerodynamics*	*Structures*	*Mission*
TOGW (lb)	759387.40	759386.72	757640.18	734507 01
ZFW (lb)	315843.35	-	301174.91	315855.95
Altitude (ft)	57200.00	57207.60	57303.38	57199.69
L/D	8.3368	8.33680	-	8.3368
SLSTH (lb)	54000.00	-	54080.83	55651.00
F_1	8910.64	8903.83	9011.68	-
F_2	16921.67	16922.54	16651.45	-
F_3	19980.85	19981.57	19825.32	-
F_4	20878.66	20878.70	20879.20	-
T_1	26630622.97	26627858.97	27322989.03	-
T_2	1662790.03	1662850.66	1748446.25	-
T_3	1261892.89	1662850.66	1201014.88	-
T_4	792351.61	791599.96	869684.02	-
δ_1(deg)	-0.9193	-0.9198	-0.7065	-
δ_2 (deg)	-1.4266	-1.4261	-1.4745	-
δ_3 (deg)	-4.2384	-4.2380	-4.2204	-

Cycle 3				
Variable Name	*Target*	*Aerodynamics*	*Structures*	*Mission*
TOGW (lb)	681630.12	681631.37	681490.43	681630.20
ZFW (lb)	294788.21	-	293830.97	294788.30
altitude (ft)	57380.93	57404.77	57381.39	57380.90
L/D	8.6547	8.6547	-	8.6547
SLSTH (lb)	54104.30	-	54113.36	54104.24
F_1	6709.66	6661.47	6575.51	-
F_2	15531.00	15515.82	15553.85	-
F_3	18502.52	18488.06	18516.17	-
F_4	19794.55	19776.56	19794.33	-
T_1	23217354.81	23196735.57	23188823.65	-
T_2	1211217.56	1210654.38	1220220.32	-
T_3	1001705.55	994328.73	968245.34	-
T_4	652001.48	653956.06	727680.58	-
δ_1 (deg)	-0.7290	-.7307	-0.7273	-
δ_2 (deg)	-1.94314	-1.9416	-1.9471	-
δ_3 (deg)	-4.3885	-4.3878	-4.3828	-

Cycle 4				
Variable Name	*Target*	*Aerodynamics*	*Structures*	*Mission*
TOGW (lb)	661630.1232	661624	661527	661630
ZFW (lb)	293909.9172	-	293910	293910
altitude (ft)	57230.13	57154.01	57232.02	57230.03
L/D	8.7560	8.7560	-	8.7562
SLSTH (lb)	54116.46	-	54126	54116
F_1	6109.0519	6156	6020	-
F_2	15158.0215	15147	15184	-
F_3	18004.2725	17997	18015	-
F_4	19743.6820	19656	19742	-
T_1	22297714.5019	22319384	22269350	-
T_2	1121709.2146	1119391	1128715	-
T_3	916566.3457	934324	889526	-
T_4	626849.5188	619003	688570	-
δ_1 (deg)	-0.74298	-.742	-.744	-
δ_2 (deg)	-2.0027	-2.01	-2.01	-
δ_3 (deg)	-4.4305	-4.433	-4.426	-

Cycle 5				
Variable Name	*Target*	*Aerodynamics*	*Structures*	*Mission*
TOGW (lb)	641630.12	642219.35	641556.49	641629.80
ZFW (lb)	292786.46	-	292416.65	292786.32
altitude (ft)	55930.13	55939.17	55930.46	55930.05
L/D	8.9125	8.82	-	8.91
SLSTH (lb)	55616.46	-	55620.55	55616.26
F_1	4959.35	5080.85	4934.28	-
F_2	14654.29	14734.82	14675.94	-
F_3	18159.93	18199.19	18165.18	-
F_4	19741.75	19695.34	19741.78	-
T_1	20927924.73	21049049.02	20902992.64	-
T_2	873175.26	886836.15	878621.55	-
T_3	812822.84	818762.90	789564.04	-
T_4	567060.80	573039.89	615795.50	-
δ_1 (deg)	-0.7343	-0.7415	-0.7356	-
δ_2 (deg)	-2.5027	-2.5147	-2.5049	-
δ_3 (deg)	-4.2894	-4.2945	-4.2856	-

Cycle 6				
Variable Name	*Target*	*Aerodynamics*	*Structures*	*Mission*
TOGW (lb)	601630.123	599503.64	601579.63	601613.05
ZFW (lb)	291942.23	-	291754.22	291981.91
altitude (ft)	54531.62	54131.22	54531.92	54532.22
L/D	8.6594	8.7482	-	8.6592
SLSTH (lb)	58616.46	-	58618.47	58616.75
F_1	4265.59	4181.43	4256.59	-
F_2	13841.82	13865.87	13855.28	-
F_3	17258.23	17250.97	17262.34	-
F_4	19089.49	19240.07	19089.39	-
T_1	19354682.81	19295411.15	19337168.16	-
T_2	737111.66	723746.10	740705.94	-
T_3	721543.29	713719.7734	705876.40	-
T_4	518354.16	514422.34	550629.64	-
δ_1 (deg)	-0.7351	-0.7362	-0.7362	-
δ_2 (deg)	-2.5082	-2.4981	-2.5098	-
δ_3 (deg)	-3.9828	-3.9756	-3.9801	-

Cycle 7				
Variable Name	*Target*	*Aerodynamics*	*Structures*	*Mission*
TOGW (lb)	601127.44	600500.84	601108.56	601055.80
ZFW (lb)	292062.94	-	292101.73	292146.03
altitude (ft)	51931.62	51809.52	51932.45	51933.02
L/D	8.5753	8.6050	-	8.5752
SLSTH (lb)	61616.46	-	61616.41	61612.18
F_1	3905.19	3879.05	3904.88	-
F_2	13685.53	13689.62	13689.95	-
F_3	17541.70	17546.06	17543.26	-
F_4	19259.43	19300.05	19259.28	-
T_1	18958780.28	18934552.91	18957767.95	-
T_2	663801.28	659702.36	663753.86	-
T_3	692667.81	690494.51	693292.78	-
T_4	511509.24	510282.07	513197.73	-
δ_1 (deg)	-0.7374	-0.7422	-0.7392	-
δ_2 (deg)	-2.5112	-2.5100	-2.5095	-
δ_3 (deg)	-3.5468	-3.5452	-3.5471	-

C.2 Design Progression

NLF Design Progression				
Variable Name	*Cycle 1*	*Cycle 2*	*Cycle 3*	*Cycle 4*
TOGW (lb)	535000	541168.49	541526.86	540285.77
ZFW (lb)	247000	248556.36	248896.77	248740.16
Altitude (ft)	50000	51074.18	50933.2	50937.06
L/D	8	7.9451	8.1362	8.1321
SLSTH (lb)	38000	33785.78	33658.35	33652.10
F_1	20000	17435.86	11489.05	11008.39
F_2	10000	14672.81	13462.70	11348.11
F_3	20000	16085.99	20636.13	23978.22
F_4	10000	7763.23	12763.2	6263.23
T_1	-8000000	-7440618.71	-7424166.48	-7085898.41
T_2	-3300000	-3669801.31	-3349838.01	-2888377.58
T_3	-2000000	-1940956.64	-1591958.50	-1227665.11
T_4	-300000	-215787.02	-315787.02	-201836.80
NLF Performance				
Range(n.mi.)	5118	5118	5236	5221
$TOFL(ft)$	9198	10664	10722	10671
$LFL(ft)$	5483	5515	5522	5518
D/T	0.794	0.937	0.910	0.914

C.2 Design Progression

NLF Design Progression				
Variable Name	*Cycle 1*	*Cycle 2*	*Cycle 3*	*Cycle 4*
TOGW (lb)	535000	541168.49	541526.86	540285.77
ZFW (lb)	247000	248556.36	248896.77	248740.16
Altitude (ft)	50000	51074.18	50933.2	50937.06
L/D	8	7.9451	8.1362	8.1321
SLSTH (lb)	38000	33785.78	33658.35	33652.10
F_1	20000	17435.86	11489.05	11008.39
F_2	10000	14672.81	13462.70	11348.11
F_3	20000	16085.99	20636.13	23978.22
F_4	10000	7763.23	12763.2	6263.23
T_1	-8000000	-7440618.71	-7424166.48	-7085898.41
T_2	-3300000	-3669801.31	-3349838.01	-2888377.58
T_3	-2000000	-1940956.64	-1591958.50	-1227665.11
T_4	-300000	-215787.02	-315787.02	-201836.80
NLF Performance				
$Range(n.mi.)$	5118	5118	5236	5221
$TOFL(ft)$	9198	10664	10722	10671
$LFL(ft)$	5483	5515	5522	5518
D/T	0.794	0.937	0.910	0.914

NLF Design Progression				
Variable Name	*Cycle 5*	*Cycle 6*	*Cycle 7*	*Cycle 8*
TOGW (lb)	538701.59	528701.59	526201.59	523601.59
ZFW (lb)	248479.95	248477.52	248477.55	248402.64
Altitude (ft)	50939.55	50985.50	51625.60	51703.92
L/D	8.1544	8.1544	8.1544	8.1484
SLSTH (lb)	33640.33	33689.11	32689.11	32748.06
F_1	10206.82	10636.25	10796.36	10763.49
F_2	10106.78	9382.48	9210.99	9027.23
F_3	25825.41	25221.51	25031.95	25069.43
F_4	4837.10	5329.78	5371.99	5080.96
T_1	-7034174.44	-6953698.84	-6944997.52	-6912922.35
T_2	-2718970.18	-2638675.18	-2628420.63	-2608822.21
T_3	-1100351.50	-1113127.81	-1123222.46	-1112960.01
T_4	-212905.72	-220702.96	-224754.39	-226250.48
NLF Performance				
$Range(n.mi.)$	5220	5073	5033	5000
$TOFL(ft)$	10607	10170	10392	10265
$LFL(ft)$	5512	5502	5499	5493
D/T	0.909	0.892	0.930	0.929

NLF Design Progression				
Variable Name	*Cycle 9*	*Cycle 10*	*Cycle 11*	*Cycle 12*
TOGW (lb)	523296.56	520596.56	520187.94	519187.94
ZFW (lb)	248267.96	247992.27	247863.99	247860.32
Altitude (ft)	52135.53	52472.1	52991.9	53491.94
L/D	8.1993	8.1942	8.2642	8.2873
SLSTH (lb)	33079.99	33238.00	33700.36	34200.36
F_1	10581.37	10030.94	10730.94	10603.56
F_2	8998.59	9533.29	9468.40	9279.57
F_3	250.1.62	24825.76	24356.94	24609.00
F_4	5780.96	5670.13	5455.23	5105.23
T_1	-6905135.82	-6827624.92	-6871355.22	-6855721.23
T_2	-2570961.41	-2589077.09	-2643766.54	-2621986.55
T_3	-1094713.55	-1070609.14	-1133771.93	-1113873.46
T_4	-221715.09	-208434.39	-219498.95	-221542.58
NLF Performance				
$Range(n.mi.)$	5022	5000	5024	5021
$TOFL(ft)$	10140	9985	9818	9628
$LFL(ft)$	5493	5480	5483	5482
D/T	0.920	0.925	0.918	0.914

NLF Design Progression					
Variable Name	*Cycle 13*	*Cycle 14*	*Cycle 15*	*Cycle 16*	*Cycle 17*
TOGW (lb)	518087.94	516587.94	513587.94	512892.76	511413.33
ZFW (lb)	247855.48	247853.00	247573.14	247420.17	247283.14
Altitude (ft)	53818.60	54125.75	54738.32	55388.32	55468.38
L/D	8.3273	8.3630	8.3980	8.4274	8.4533
SLSTH (lb)	34627.86	34468.25	34104.61	34214.03	33914.65
F_1	10712.85	11037.43	11009.85	10717.84	10780.09
F_2	9353.01	9327.62	8977.62	9185.12	90.1.46
F_3	24340.88	23990.88	24190.40	24147.59	240.1.82
F_4	5280.69	5298.99	4713.99	4874.05	5251.12
T_1	-6850383.39	-6855102.60	-6824705.94	-6796846.32	-6787166.60
T_2	-2632334.85	-2652554.24	-2625974.73	-2619658.76	-2595634.54
T_3	-1127889.48	-1158016.13	-1142954.56	-1124031.07	-1124444.00
T_4	-221155.65	-225583.31	-230798.64	-223104.23	-223162.86
NLF Performance					
$Range(n.mi.)$	5027	5024	5005	5014	5000
$TOFL(ft)$	9461	9448	9435	9376	9338
$LFL(ft)$	5481	5479	5472	5468	5467
D/T	0.906	0.912	0.930	0.940	0.950

C.3 Subproblem Result Progression

NLF - Cycle 1				
Variable Name	*Target*	*Aerodynamics*	*Structures*	*Mission*
TOGW (lb)	535000	539579.28	534730.13	535000.45
ZFW (lb)	247000	-	254030.90	246997.08
altitude (ft)	50000	50485.16	49999.55	49999.99
L/D	8	7.7427	-	8.0000
SLSTH (lb)	38000	37492.22	37933.47	38000.01
F_1	20000	19184.88	19984.15	-
F_2	10000	10290.88	9987.44	-
F_3	20000	18848.63	19995.68	-
F_4	10000	10107.11	9999.51	-
T_1	-8000000	-7836766	-8000006.36	-
T_2	-3300000	-3294614.69	-3299955.49	-
T_3	-2000000	-1906491.23	-1999848.90	-
T_4	-300000	-307550.58	-300000.12	-

NLF - Cycle 2				
Variable Name	*Target*	*Aerodynamics*	*Structures*	*Mission*
TOGW (lb)	541168.49	541107.34	541110.05	541168.45
ZFW (lb)	248556.36	-	250.17.12	248556.49
altitude (ft)	51074.18	51057.42	51073.42	51074.18
L/D	7.9451	7.9465	-	7.9451
SLSTH (lb)	33785.78	33791.94	33769.57	33785.79
F_1	17435.86	17424.08	17432.91	-
F_2	14672.81	14551.37	14668.65	-
F_3	16085.99	16058.72	16083.48	-
F_4	7763.23	7722.82	7762.37	-
T_1	-7440618.71	-7446541.82	-7440583.54	-
T_2	-3669801.31	-3670936.20	-3669842.99	-
T_3	-1940956.64	-1937790.63	-1940598.17	-
T_4	-215787.02	-215156.03	-215778.30	-

NLF - Cycle 3				
Variable Name	*Target*	*Aerodynamics*	*Structures*	*Mission*
TOGW (lb)	541526.86	541526.71	541563.77	541526.91
ZFW (lb)	248896.77	-	248883.07	248896.67
altitude (ft)	50933.21	50933.14	50.19.02	50933.21
L/D	8.1362	8.1362	-	8.1362
SLSTH (lb)	33658.35	33658.28	33661.20	33658.35
F_1	11489.05	11489.48	11499.96	-
F_2	13462.70	13463.35	13464.17	-
F_3	20636.13	20636.36	20630.99	-
F_4	12763.23	12763.32	12759.10	-
T_1	-7424166.48	-7424164.33	-7424091.00	-
T_2	-3349838.01	-3349830.88	-3350814.66	-
T_3	-1591958.50	-1591965.25	-1588371.79	-
T_4	-315787.02	-315787.76	-315790.75	-

NLF - Cycle 4				
Variable Name	*Target*	*Aerodynamics*	*Structures*	*Mission*
TOGW (lb)	540285.77	540286.17	540280.83	540285.83
ZFW (lb)	248740.16	-	248697.83	248739.99
altitude (ft)	50937.06	50937.18	50936.43	50937.06
L/D	8.1321	8.1321	-	8.1321
SLSTH (lb)	33652.10	33652.09	33652.80	33652.10
F_1	11008.39	11008.60	11003.10	-
F_2	11348.11	11348.10	11354.89	-
F_3	23978.22	23978.19	23989.59	-
F_4	6263.23	6263.21	6263.89	-
T_1	-7085898.41	-7085901.64	-7085819.80	-
T_2	-2888377.58	-2888373.85	-2887788.51	-
T_3	-1227665.11	-1227659.91	-1224521.15	-
T_4	-201836.80	-201836.02	-201800.12	-

NLF - Cycle 5				
Variable Name	*Target*	*Aerodynamics*	*Structures*	*Mission*
TOGW (lb)	538701.59	538702.05	538708.47	538701.65
ZFW (lb)	248479.95	-	248438.96	248479.81
altitude (ft)	50939.55	50939.67	50937.50	50939.55
L/D	8.1544	8.1544	-	8.1544
SLSTH (lb)	33640.33	33640.33	33645.49	33640.33
F_1	10206.82	10206.66	10213.98	-
F_2	10106.78	10106.80	10112.42	-
F_3	25825.41	25825.42	25827.60	-
F_4	4837.10	4837.15	4833.14	-
T_1	-7034174.44	-7034171.45	-7033925.87	-
T_2	-2718970.18	-2718970.43	-2718976.60	-
T_3	-1100351.50	-1100356.69	-110.117.31	-
T_4	-212905.72	-212906.72	-212895.97	-

NLF - Cycle 6				
Variable Name	*Target*	*Aerodynamics*	*Structures*	*Mission*
TOGW (lb)	528701.59	528701.42	528674.08	528701.56
ZFW (lb)	248477.52	-	248465.96	248477.61
altitude (ft)	50985.50	50985.46	50983.71	50985.50
L/D	8.1544	8.1544	-	8.1544
SLSTH (lb)	33689.11	33689.11	33694.76	33689.11
F_1	10636.25	10636.27	10636.96	-
F_2	9382.48	9382.52	9395.23	-
F_3	25221.51	25221.53	25233.82	-
F_4	5329.78	5329.79	5327.26	-
T_1	-6953698.84	-6953697.42	-6953480.65	-
T_2	-2638675.18	-2638676.82	-2638441.17	-
T_3	-1113127.81	-1113124.60	-1112203.78	-
T_4	-220702.96	-220703.10	-220692.12	-

NLF - Cycle 7				
Variable Name	*Target*	*Aerodynamics*	*Structures*	*Mission*
TOGW (lb)	526201.59	526201.18	526201.12	526201.53
ZFW (lb)	248477.55	-	248473.32	248477.74
altitude (ft)	51625.60	51625.49	51625.53	51625.60
L/D	8.1544	8.1544	-	8.1544
SLSTH (lb)	32689.11	32689.12	32689.18	32689.11
F_1	10796.36	10796.33	10796.47	-
F_2	9210.99	9211.054	9211.12	-
F_3	25031.95	25031.85	250.1.04	-
F_4	5371.99	5371.94	5371.93	-
T_1	-6944997.52	-6945004.24	-6944996.28	-
T_2	-2628420.63	-2628415.03	-2628420.59	-
T_3	-1123222.46	-1123211.30	-1123225.29	-
T_4	-224754.39	-224754.57	-224754.54	-

NLF - Cycle 8				
Variable Name	*Target*	*Aerodynamics*	*Structures*	*Mission*
TOGW (lb)	523601.59	523601.26	523601.08	523681.76
ZFW (lb)	248402.64	-	248398.62	248234.02
altitude (ft)	51703.92	51703.84	51703.87	51703.71
L/D	8.1484	8.1484	-	8.1488
SLSTH (lb)	32748.06	32748.06	32748.11	32748.08
F_1	10763.49	10763.50	10763.56	-
F_2	9027.23	9027.39	9027.34	-
F_3	25069.43	25069.47	25069.53	-
F_4	5080.96	5080.99	5080.93	-
T_1	-6912922.35	-6912917.22	-6912922.27	-
T_2	-2608822.21	-2608820.45	-2608821.08	-
T_3	-1112960.01	-1112954.62	-1112963.89	-
T_4	-226250.48	-226251.23	-226250.68	-

NLF - Cycle 9				
Variable Name	*Target*	*Aerodynamics*	*Structures*	*Mission*
TOGW (lb)	523296.56	523297.64	523292.86	523296.50
ZFW (lb)	248267.96	-	248215.40	248268.14
altitude (ft)	52135.53	52135.77	52135.41	52135.53
L/D	8.1993	8.1993	-	8.1993
SLSTH (lb)	33079.99	33079.95	33081.52	33079.99
F_1	10581.37	10581.27	10584.52	-
F_2	8998.59	8998.73	9001.60	-
F_3	250.1.62	250.1.69	25064.21	-
F_4	5780.96	5781.08	5780.83	-
T_1	-6905135.82	-6905124.18	-6905121.92	-
T_2	-2570961.41	-2570959.54	-2570945.97	-
T_3	-1094713.55	-1094730.88	-1094597.43	-
T_4	-221715.09	-221716.50	-221713.87	-

NLF - Cycle 10				
Variable Name	*Target*	*Aerodynamics*	*Structures*	*Mission*
TOGW (lb)	520596.56	520597.04	520598.41	520762.89
ZFW (lb)	247992.27	-	247930.11	247642.95
altitude (ft)	52472.18	52472.29	52471.54	52471.74
L/D	8.1942	8.1942	-	8.1949
SLSTH (lb)	33238.006	33237.99	33240.61	33238.02
F_1	10030.94	10031.01	100.1.95	-
F_2	9533.29	9533.36	9535.77	-
F_3	24825.76	24825.72	24827.32	-
F_4	5670.13	5670.16	5668.82	-
T_1	-6827624.92	-6827623.83	-6827497.51	-
T_2	-2589077.09	-2589078.19	-2589029.25	-
T_3	-1070609.14	-1070593.55	-1070398.30	-
T_4	-208434.39	-208435.04	-208428.51	-

NLF - Cycle 11				
Variable Name	*Target*	*Aerodynamics*	*Structures*	*Mission*
TOGW (lb)	520187.94	520188.66	520137.01	520187.90
ZFW (lb)	247863.99	-	247850.06	247864.11
altitude (ft)	52991.94	52992.10	52990.38	52991.94
L/D	8.2642	8.2642	-	8.2642
SLSTH (lb)	33700.36	33700.34	33704.23	33700.36
F_1	10730.94	10731.05	10.16.81	-
F_2	9468.40	9468.55	9481.73	-
F_3	24356.94	24356.89	24370.69	-
F_4	5455.23	5455.20	5452.88	-
T_1	-6871355.22	-6871357.80	-6871148.70	-
T_2	-2643766.54	-2643755.17	-2643669.62	-
T_3	-1133771.93	-1133769.61	-1133429.93	-
T_4	-219498.95	-219499.07	-219496.33	-

NLF - Cycle 12				
Variable Name	*Target*	*Aerodynamics*	*Structures*	*Mission*
TOGW (lb)	519187.94	519187.31	519151.38	519187.90
ZFW (lb)	247860.32	-	247826.07	247860.43
altitude (ft)	53491.94	53491.81	53491.54	53491.94
L/D	8.2873	8.2873	-	8.2873
SLSTH (lb)	34200.36	34200.39	34204.35	34200.36
F_1	10603.56	10603.70	10604.58	-
F_2	9279.57	9279.46	9293.08	-
F_3	24609.00	24609.05	24622.32	-
F_4	5105.23	5105.19	5104.27	-
T_1	-6855721.23	-6855724.30	-6855578.19	-
T_2	-2621986.55	-2621984.98	-2621628.04	-
T_3	-1113873.46	-1113871.64	-1112577.45	-
T_4	-221542.58	-221541.41	-221532.82	-

NLF - Cycle 13				
Variable Name	*Target*	*Aerodynamics*	*Structures*	*Mission*
TOGW (lb)	518087.94	518087.00	5180.1.46	518087.91
ZFW (lb)	247855.48	-	247823.87	247855.56
altitude (ft)	53818.60	53818.39	53818.07	53818.60
L/D	8.3273	8.3273	-	8.3273
SLSTH (lb)	34627.86	34627.90	34630.41	34627.86
F_1	10712.85	10712.76	10.11.61	-
F_2	9353.01	9353.09	9354.88	-
F_3	24340.88	24340.95	24335.50	-
F_4	5280.69	5280.68	5277.89	-
T_1	-6850383.39	-6850380.04	-6850171.49	-
T_2	-2632334.85	-2632335.35	-2632465.44	-
T_3	-1127889.48	-1127890.61	-1130571.97	-
T_4	-221155.65	-221156.09	-221185.35	-

NLF - Cycle 14				
Variable Name	*Target*	*Aerodynamics*	*Structures*	*Mission*
TOGW (lb)	516587.94	516587.76	516623.33	516587.92
ZFW (lb)	247853.00	-	247697.00	247853.07
altitude (ft)	54125.75	54125.71	54125.30	54125.75
L/D	8.3630	8.3630	-	8.3630
SLSTH (lb)	34468.25	34468.26	34470.89	34468.26
F_1	11037.43	11037.40	11029.50	-
F_2	9327.62	9327.69	9321.85	-
F_3	23990.88	23990.96	23989.19	-
F_4	5298.99	5299.04	5297.33	-
T_1	-6855102.60	-6855095.40	-6854924.87	-
T_2	-2652554.24	-2652558.27	-2652371.52	-
T_3	-1158016.13	-1158015.68	-1157383.27	-
T_4	-225583.31	-225583.99	-225569.18	-

NLF - Cycle 15				
Variable Name	*Target*	*Aerodynamics*	*Structures*	*Mission*
TOGW (lb)	513587.94	513588.55	513632.17	513587.94
ZFW (lb)	247573.14	-	247450.52	247573.15
altitude (ft)	54738.32	54738.45	54738.01	54738.32
L/D	8.3980	8.3980	-	8.3980
SLSTH (lb)	34104.61	34104.57	34106.06	34104.61
F_1	11009.85	11009.78	11008.69	-
F_2	8977.62	8977.63	8970.08	-
F_3	24190.40	24190.46	24185.03	-
F_4	4713.99	4714.07	4712.901	-
T_1	-6824705.94	-6824698.52	-6824607.33	-
T_2	-2625974.73	-2625978.89	-2625907.93	-
T_3	-1142954.56	-1142962.49	-1142073.97	-
T_4	-230798.64	-230799.36	-230781.03	-

NLF - Cycle 16				
Variable Name	*Target*	*Aerodynamics*	*Structures*	*Mission*
TOGW (lb)	512892.76	512892.09	512892.17	512892.74
ZFW (lb)	247420.17	-	247370.19	247420.34
altitude (ft)	55388.32	55388.19	55388.29	55388.32
L/D	8.4274	8.4275	-	8.4274
SLSTH (lb)	34214.03	34214.07	34214.81	34214.03
F_1	10717.84	10717.71	10715.67	-
F_2	9185.12	9185.15	9184.77	-
F_3	24147.59	24147.59	24147.75	-
F_4	4874.05	4873.99	4873.31	-
T_1	-6796846.32	-6796848.46	-6796797.25	-
T_2	-2619658.76	-2619663.18	-2619648.95	-
T_3	-1124031.07	-1124025.19	-1124453.74	-
T_4	-223104.23	-223104.31	-223111.78	-

NLF - Cycle 17				
Variable Name	*Target*	*Aerodynamics*	*Structures*	*Mission*
TOGW (lb)	511413.33	511414.26	511486.65	511413.30
ZFW (lb)	247283.14	-	247201.58	247283.22
altitude (ft)	55468.38	55468.58	55467.71	55468.38
L/D	8.4533	8.4533	-	8.4533
SLSTH (lb)	33914.65	33914.60	33915.67	33914.65
F_1	10780.09	10780.19	10777.87	-
F_2	90.1.46	90.1.33	9035.08	-
F_3	240.1.82	240.1.72	24007.31	-
F_4	5251.12	5251.17	5247.55	-
T_1	-6787166.60	-6787172.85	-6786923.90	-
T_2	-2595634.54	-2595627.21	-2595829.87	-
T_3	-1124444.00	-1124441.45	-1124820.57	-
T_4	-223162.86	-223162.77	-223153.32	-